Optical Interface Based on a Nanofiber Atom-Trap

Dissertation

zur
Erlangung des Grades
„Doktor
der Naturwissenschaften"
am Fachbereich Physik
der
Johannes Gutenberg-Universität
in Mainz

Eugen Vetsch
aus Mainz

Mainz, 2010

D77

Abstract

In this thesis, I present the realization of a fiber-optical interface using optically trapped cesium atoms, which is an efficient tool for coupling light and atoms. The basic principle of the presented scheme relies on the trapping of neutral cesium atoms in a two-color evanescent field surrounding a nanofiber. The strong confinement of the fiber guided light, which also protrudes outside the nanofiber, provides strong confinement of the atoms as well as efficient coupling to near-resonant light propagating through the fiber.

In chapter 1, the necessary physical and mathematical background describing the propagation of light in an optical fiber is presented. The exact solution of Maxwell's equations allows us to model fiber-guided light fields which give rise to the trapping potentials and the atom-light coupling in the close vicinity of a nanofiber. In addition, the fabrication of tapered optical fibers (TOFs) with a nanofiber waist from standard glass fibers is presented. Chapter 2 gives the theoretical background of light-atom interaction. A quantum mechanical model of the light-induced shifts of the relevant atomic levels is reviewed, which allows us to quantify the perturbation of the atomic states due to the presence of the trapping light-fields.

The experimental realization of the fiber-based atom trap is the focus of chapter 3. Here, I analyze the properties of the trap in terms of the confinement of the atoms and the impact of several heating mechanisms. In particular, the detrimental effect of fundamental and technical noise on the storage time due to heating and subsequent loss of atoms is examined. Furthermore, I demonstrate the transportation of the trapped atoms, as a first step towards a deterministic delivery of individual atoms.

In chapter 4, I present the successful interfacing of the trapped atomic ensemble and fiber-guided light. Three different approaches are discussed, i.e., those involving the measurement of either near-resonant scattering in absorption or the emission into the guided mode of the nanofiber. In the analysis of the spectroscopic properties of the trapped ensemble we find good agreement with the prediction of theoretical model discussed in chapter 2. In addition, I introduce a non-destructive scheme for the interrogation of the atoms states, which is sensitive to phase shifts of far-detuned fiber-guided light interacting with the trapped atoms. The inherent birefringence in our system, induced by the atoms, changes the state of polarization of the probe light and can be thus detected via a Stokes vector measurement.

Contents

Introduction

Since the first exploration of individual quantum systems, a large variety of experimental work has been carried out in order to investigate quantum effects with the aim of testing several models and predictions of quantum theory [1]. The feasibility to efficiently access and manipulate the quantum degrees of freedom of such systems has even initiated research on quantum information processing [2]. For this purpose many different approaches (employing, e.g., ions, neutral atoms, quantum dots, and other solid state devices [7, 9] as quantum systems) have been proposed, and have been, to varying degrees, successfully demonstrated.

In view of the requirements for practical applications of, e.g., quantum information technologies [3], neutral atoms are one of the most promising candidates as storage units for quantum information (qubits) [5, 6]. Due to the weak coupling of neutral atoms to their environment, qubits encoded as coherent superposition of internal atomic states, can be robust against external influences, which means that decoherence, i.e., loss of quantum information can be minimized. Moreover, recent advances in atomic/optical physics allows for the coherent control and manipulation of atomic external and internal states [6].

At the same time, solid state quantum devices, such as quantum dots or superconducting circuits, are readily miniaturized and integrated using well established technologies [7]. For these reasons, the possibility of combining the advantageous properties of atomic and solid state devices in hybrid quantum systems has recently attracted considerable interest [8–10]. In order to realize such a hybrid quantum system, the atoms need to be efficiently interfaced with near-resonant probe light for manipulation and interrogation. Moreover, the atoms need to be trapped in close vicinity of the solid state devices in order to be coupled via electric or magnetic interaction.

Ideally, the optical interface would be mediated by fiber-guided light which could bridge efficiently long distances. In this respect, using tapered optical fibers (TOF) provides both prerequisites, efficient light-atom coupling, and low-loss transmission of the light. These TOF feature a highly efficient coupling of the fiber-guided mode in and out of the nanofiber waist [11, 12], resulting in a strongly confined optical mode which couples to the atoms via the evanescent field [15, 32]. In this

case, the atomic ensembles can be directly interfaced with the fiber-guided light, making the quantum fields intrinsically mode-matched and efficiently coupled into single-mode optical fiber [16, 17]. The realization of such an interface between different quantum systems may not only provide key technological requirements for quantum information processing, but it also bares potential for the implementation of quantum communication schemes over long distances using optical fibers.

The transmission of bits of data on the level of single photons in combination with *quantum cryptography* techniques promises a provably secure way to exchange information [18, 19]. In regard to the quantum nature of photons they can be prepared in pairs of non-locally connected (entangled) states carrying an encoded qubit, which forms the basis for most optical quantum communication schemes [20]. Using optical fibers as transmission channels for these entangled photons would appear to be the best option, simply because of the high bandwidth and low losses provided by optical glass fibers over long distances. For the same reasons, classical telecommunication is mainly based on optical fiber networks.

Fiber-based quantum communication schemes have been realized by a few research groups, demonstrating quantum key distribution over hundred kilometers [21, 22]. However, their applications in large-scale (global) networks is not straightforwardly possible. Due to losses and decoherence of the quantum channels, the communication fidelity decreases exponentially with the fiber length, making direct quantum communication techniques impractical for distances much larger than 100 km [9]. This limitation can be overcome by subdividing the long distances to be bridged into smaller segments. The entanglement can be extended by connecting the adjacent segments via entanglement swapping in each section [20, 23]. Because the nature of this approach is probabilistic, it requires storing the successfully entangled segment state in a quantum memory, while waiting for the others to be generated. It can be shown that the number of required segments as well as the communication time rises only polynomially with growing distances [20]. A key element of such a "repeater" approach is the transfer of quantum information between ("flying") photonic qubits and stationary matter-based qubits providing low decoherence rates [20, 24, 25].

Most recently, quantum repeaters as well as quantum memories based on the coupling of freely propagating light beams with laser-cooled atomic ensembles have been successfully demonstrated [26, 27]. In these experiments, the entanglement, encoded in collective single spin excitations (spin waves), was stored in the ensemble and could subsequently transferred to single photons. This approach takes advantage of the collective enhancement of light-matter interaction (super radiance), making the transfer of quantum information very efficient. However, the dephasing of the spin wave due to thermal atomic motion limits the storage time. Furthermore, the mode-matching and fiber coupling with free beam optics limits the photon collection efficiency. Introducing fiber-coupled and trapped atoms instead might help to overcome these issues.

The coupling of laser-cooled atoms with fiber-guided light has been an active field of research over the past few years. For this purpose, two types of optical fibers have been considered: hollow core fibers and optical nanofibers. In the former, the atoms are funneled into a capillary in the center of the fiber where they couple to the guided fiber mode [28, 29], while in the latter, the atoms remain at the outside of a nanofiber with a diameter smaller than the wavelength of the guided light and couple to the evanescent field surrounding the fiber [15, 16]. The ultimate goal in both lines of research is to combine the coupling scheme with three dimensional trapping of the atoms in order to avoid dephasing due to thermal motion and collisions, thereby maximizing both the number of coupled atoms, as well as the optical density and the interaction time. In this context, it has been proposed to realize a two-color optical dipole trap which makes use of a red-detuned and blue-detuned evanescent light field around the optical nanofiber [30, 31].

In this thesis, I demonstrate the realization of an optical interface with trapped neutral cesium atoms carried by a two-color evanescent field surrounding the nanofiber waist of a TOF. This work is a first step towards fiber-based quantum memories and quantum hybrid systems. The atoms are localized in a one-dimensional optical lattice about 230 nm above the nanofiber surface and can be efficiently interfaced with a resonant light field sent through the nanofiber. Strong confinement of the atoms in all three dimensions is achieved by a periodic standing wave potential in conjunction with a azimuthally varying intensity distribution for the linearly polarized evanescent field. Due to the small trapping volumes the loading operates in the collisional blockade regime resulting in an occupancy of at most one atom per trapping site. Each of the trapped atoms absorbs up to 1.6% of the resonant propagating light power. In conjunction with the 2000 trapped atoms this yields an optical density (OD) of 32. Such strong coupling of the atoms and the fiber-guided modes even allows us to interrogate the atoms non-destructively by means of an off-resonant phase measurement.

Publications related to this thesis:

- E. Vetsch, D. Reitz, G. Sagué, R. Schmidt,S. T. Dawkins, and A. Rauschenbeutel, *Optical Interface Created by Laser-Cooled Atoms Trapped in the Evanescent Field Surrounding an Optical Nanofiber*, Phys. Rev. Lett. **104**, 203603 (2010).

- S. T. Dawkins, E. Vetsch, D. Reitz, R. Mitsch, and A. Rauschenbeutel, *Nondestructive Phase Detection with fiber coupled atoms*, In preparation (2010).

- G. Sagué, E. Vetsch, W. Alt, D. Meschede and A. Rauschenbeutel, *Cold Atom Physics Using Ultra-Thin Optical Fibers: Light-Induced Dipole Forces and Surface Interactions*, Phys. Rev. Lett. **99**, 163602 (2007).

- F. Warken, E. Vetsch, D. Meschede, M. Sokolowski, and A. Rauschenbeutel, *Ultra-sensitive surface absorption spectroscopy using sub-wavelength diameter optical fibers*, Optics Express **15**, 19 11952-11958 (2007).

Chapter 1

# Light propagation in step-index fibers

Standard optical glass fibers, used in telecommunication or for scientific purposes, are based on a cladded-core structure (see Fig. 1.1). Core and cladding are produced by chemical vapor deposition (CVD) of SiO_2 doped with germanium or fluorine, respectively, in order to obtain a slightly higher refractive index in the core. Due to the higher index of refraction, light is confined to the core and can be guided by total internal reflection along the fiber.

However, since the difference in the refractive index is less than 1%, the propagating mode leaks far out of the core in the form of the evanescent field and co-propagates in the cladding region. A thick layer of glass cladding is therefore required to isolate the guided light from the outside. Typical dimensions of the fibers are 2-5 μm-radius of the core surrounded by 60-μm glass cladding. The existence of the evanescent field, which is a consequence of the boundary conditions for electromagnetic waves at the core-cladding interface, is the basis for many applications employing air-cladded fibers. Chemical sensing [35, 36], light splitting and combining, etc. are some examples.

Recently, much attention has been given to sub-wavelength diameter tapered optical fibers (TOFs). These *nanofibers* feature a strong transverse confinement of the guided fiber mode. In addition, the projection of the mode outside the core results in an intense evanescent field surrounding the fiber. In the following, the theoretical concepts of guiding light in nanofiber waveguides and the distribution of fields outside the nanofiber, which is the basis of the current work, will be given.

1.1   Maxwell's equations in a step-index optical fiber

In this section, a brief introduction to the description of light propagation and the
field distribution in and outside an optical fiber, will be given. The exact solution
of Maxwell's equations is presented, thus providing the foundation of modeling the
trapping potential as well as the coupling of the evanescent field to the atoms. A
detailed treatment of these issues can be found in [32–34] and is closely followed
here.
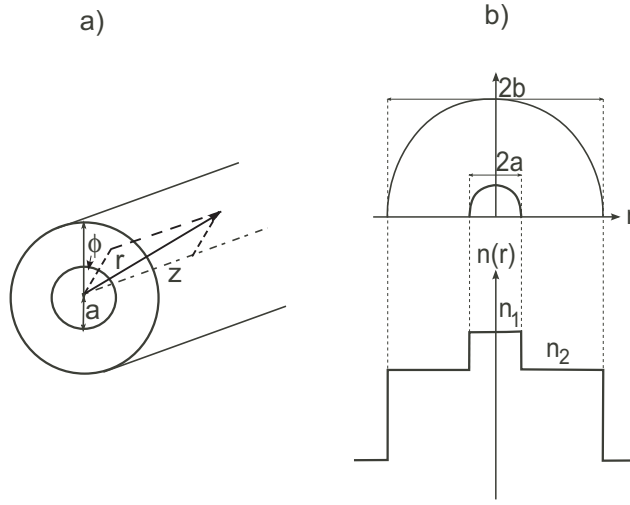
$$n(r) = \begin{cases} n_1 & \text{if } r < a \\ n_2 & \text{if } r > a \end{cases} \text{ with } n_1 > n_2$$

$$(1.1)$$

FIGURE 1.1:   a) Geometry of a standard glass fiber and b) the profile of its
refractive index as a function of r.

A schematic of the structure of a step-index cylindrical fiber is shown in Fig. 1.1.
Note that for a nanofiber the cladding is replaced by vacuum. The refractive index
n as a function of r is given by Eq. (1.1), where a denotes the core radius, n_1 the
refractive index inside the fiber, and n_2 the refractive index in the surrounding
medium (cladding). The wave equation of light propagation in such a fiber [33],

$$\vec{\nabla}^2 \vec{E} - \mu_0 \varepsilon(r) \frac{\partial^2 \vec{E}}{\partial t^2} = -\vec{\nabla}\left(\frac{\vec{E}}{\varepsilon(r)} \cdot \vec{\nabla}\varepsilon(r)\right) \tag{1.2}$$

can be derived from Maxwell's equations:

$$\vec{\nabla} \times \vec{H} = \varepsilon(r)\frac{\partial \vec{E}}{\partial t}, \qquad \vec{\nabla} \cdot \vec{H} = 0 \tag{1.3}$$

$$\vec{\nabla} \times \vec{E} = -\mu_0 \frac{\partial \vec{H}}{\partial t}, \qquad \vec{\nabla} \cdot (\varepsilon(r)\vec{E}) = 0$$

Here, $\vec{E}$ denotes the electric field vector, μ_0 the vacuum permeability, and $\varepsilon(= n^2)$ the electric permittivity of the medium. The wave equation for the magnetic field $\vec{H}$ takes the same form as Eq. (1.2). For a cylindrical symmetric wave guide, e.g. a circular step-index fiber, the right hand side of Eq. (1.2) vanishes. Due to this symmetry, it is convenient to derive the field components in cylindrical coordinates $(r,\ \phi,\ z)$. The solutions of Eq. (1.2) for the axial component take the simple form of

$$\begin{bmatrix} E_z(\vec{r},t) \\ H_z(\vec{r},t) \end{bmatrix} = \begin{bmatrix} E_z(r,\phi) \\ H_z(r,\phi) \end{bmatrix} \exp[i(\omega t - \beta z)], \tag{1.4}$$

where β is the axial propagation constant of the field. Moreover, employing Maxwell's equations in cylindrical coordinates:

$$\begin{aligned} i\omega\varepsilon E_r &= i\beta\frac{\partial}{\partial r}E_z + \frac{1}{r}\frac{\partial}{\partial\phi}H_z \\ i\omega\varepsilon E_\phi &= -i\beta H_r - \frac{\partial}{\partial r}H_z \\[2mm] -i\omega\mu H_r &= i\beta\frac{\partial}{\partial r}H_z + \frac{1}{r}\frac{\partial}{\partial\phi}E_z \\ -i\omega\mu H_\phi &= -i\beta E_r - \frac{\partial}{\partial r}E_z \end{aligned} \tag{1.5}$$

all remaining components, E_r, H_r, E_ϕ and H_ϕ, can be expressed in terms of E_z and H_z.

$$\begin{aligned} E_r &= \frac{-i\beta}{\omega^2\mu\varepsilon-\beta^2}\left(\frac{\partial}{\partial r}E_z + \frac{\omega\mu}{\beta}\frac{\partial}{r\partial\phi}H_z\right) \\ E_\phi &= \frac{-i\beta}{\omega^2\mu\varepsilon-\beta^2}\left(\frac{\partial}{r\partial\phi}E_z - \frac{\omega\mu}{\beta}\frac{\partial}{\partial r}H_z\right) \\[2mm] H_r &= \frac{-i\beta}{\omega^2\mu\varepsilon-\beta^2}\left(\frac{\partial}{\partial r}H_z - \frac{\omega\varepsilon}{\beta}\frac{\partial}{r\partial\phi}E_z\right) \\ H_\phi &= \frac{-i\beta}{\omega^2\mu\varepsilon-\beta^2}\left(\frac{\partial}{r\partial\phi}H_z + \frac{\omega\varepsilon}{\beta}\frac{\partial}{\partial r}E_z\right). \end{aligned} \tag{1.6}$$

The solution of the whole problem can now be reduced to the solution of the wave equation for the z-components of Eq. (1.2)

$$\left[\partial_r^2 + \frac{1}{r}\partial_r + \frac{1}{r^2}\partial_\phi^2 + (k^2 - \beta^2)\right]\begin{bmatrix} E_z(r,\phi) \\ H_z(r,\phi) \end{bmatrix} = 0, \tag{1.7}$$

where $k^2 = \mu_0\varepsilon\omega^2$.

This equation is separable with solutions of the form

$$\begin{bmatrix} E_z(r,\phi) \\ H_z(r,\phi) \end{bmatrix} = R(r)\exp[\pm il\phi], \tag{1.8}$$

where $l = 0, 1, 2, ...$
For the radial functions, $R(r)$, Eq. (1.7) becomes the Bessel differential equation

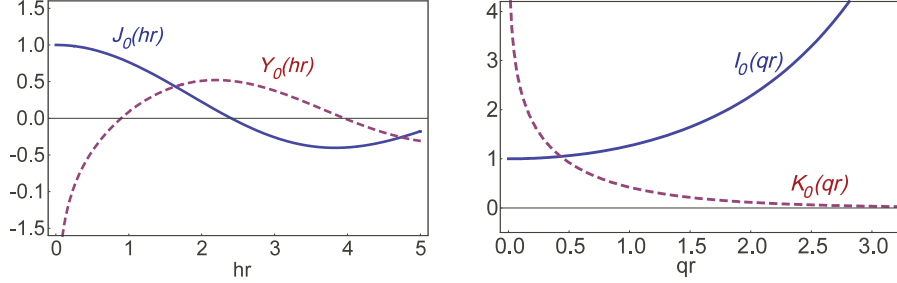$$\left[\partial_r^2 + \frac{1}{r}\partial_r + (k^2 - \beta^2 - \frac{l^2}{r^2})\right]R(r) = 0. \tag{1.9}$$

FIGURE 1.2: Plot of the Bessel functions of the first and second kind (J_0, Y_0, left), and the modified Bessel functions (I_0, K_0, right) all of order $l = 0$.

The general solutions of Eq. (1.9) are Bessel functions of order l depending on the sign of $k^2 - \beta^2$

$$R(r) = c_1 J_l(hr) + c_2 Y_l(hr) \text{ for } k^2 - \beta^2 > 0, \text{ with } h^2 = k^2 - \beta^2, \tag{1.10}$$

$$R(r) = c_3 I_l(qr) + c_4 K_l(qr) \text{ for } k^2 - \beta^2 < 0, \text{ with } q^2 = \beta^2 - k^2. \tag{1.11}$$

Here, J_l denotes the Bessel function of the first kind, Y_l the Bessel function of the second kind, I_l the modified Bessel function of the first kind and K_l the modified Bessel function of the second kind, all of order l.

The condition that any lossless modes be confined to the core, restricts the axial propagation constant β within the range of values given by

$$n_2 k_0 \leq \beta \leq n_1 k_0, \tag{1.12}$$

where $k_0 = \omega/c$ is the wave vector of the propagating field in vacuum. The solution of Eq. (1.9) will therefore take the form of Eq. (1.10) inside the core, for $r < a$, and the form of Eq. (1.11) in the surrounding medium, for $r > a$.

Since Y_l is singular at $r = 0$ (compare Fig. (1.2)), the fields in Eq. (1.9) are only finite if $c_2 = 0$. For a lossless mode the power density is restricted to the fiber, the guided fields must therefore vanish for large r.

Because I_l diverges as $r \to \infty$ (compare Fig. (1.2)), it requires $c_3 = 0$ in order to show an evanescent decay of the field outside the fiber.

The field components E_z and H_z can now be expressed as

$$E_z(r, \phi, z, t) = A J_l(hr) \exp[i(\omega t \pm l\phi - \beta z)], \tag{1.13}$$

$$H_z(r, \phi, z, t) = B J_l(hr) \exp[i(\omega t \pm l\phi - \beta z)], \tag{1.14}$$

$$\text{with } h = \sqrt{n_1^2 k_0^2 - \beta^2} \tag{1.15}$$

inside the core ($r < a$), and

$$E_z(r,\phi,z,t) = CK_l(qr)\exp[i(\omega t \pm l\phi - \beta z)], \qquad (1.16)$$
$$H_z(r,\phi,z,t) = DK_l(qr)\exp[i(\omega t \pm l\phi - \beta z)], \qquad (1.17)$$
$$\text{with } q = \sqrt{\beta^2 - n_2^2 k_0^2} \qquad (1.18)$$

outside the core ($r > a$).

Using the expressions above together with Eqns. (1.3), (1.4) and (1.6), E_r, E_ϕ, H_r and H_ϕ are expressed in terms of E_z and H_z.

For $r < a$

$$E_r(r,\phi,z,t) = -\frac{\beta}{h}\left[iAJ_l'(hr) - \frac{\omega\mu_0(\pm l)}{\beta}B\frac{J_l(hr)}{hr}\right]\exp[i(\omega t \pm l\phi - \beta z)],$$

$$E_\phi(r,\phi,z,t) = \frac{\beta}{h}\left[(\pm l)A\frac{J_l(hr)}{hr} + \frac{i\omega\mu_0}{\beta}BJ_l'(hr)\right]\exp[i(\omega t \pm l\phi - \beta z)],$$

$$E_z(r,\phi,z,t) = AJ_l(hr)\exp[i(\omega t \pm l\phi - \beta z)], \qquad (1.19)$$

$$H_r(r,\phi,z,t) = -\frac{\beta}{h}\left[iBJ_l'(hr) + \frac{\omega\varepsilon_1(\pm l)}{\beta}A\frac{J_l(hr)}{hr}\right]\exp[i(\omega t \pm l\phi - \beta z)],$$

$$H_\phi(r,\phi,z,t) = \frac{\beta}{h}\left[(\pm l)B\frac{J_l(hr)}{hr} - \frac{i\omega\varepsilon_1}{\beta}AJ_l'(hr)\right]\exp[i(\omega t \pm l\phi - \beta z)],$$

$$H_z(r,\phi,z,t) = BJ_l(hr)\exp[i(\omega t \pm l\phi - \beta z)], \qquad (1.20)$$

where $J_l'(hr) = dJ(hr)/d(hr)$ and $\varepsilon_1 = n_1^2\varepsilon_0$ is the dielectric constant inside the core or inside the nanofiber.

For $r > a$

$$E_r(r,\phi,z,t) = \frac{\beta}{q}\left[iCK_l'(qr) - \frac{\omega\mu_0(\pm l)}{\beta}D\frac{K_l(qr)}{qr}\right]\exp[i(\omega t \pm l\phi - \beta z)],$$

$$E_\phi(r,\phi,z,t) = -\frac{\beta}{q}\left[(\pm l)C\frac{K_l(qr)}{qr} + \frac{i\omega\mu_0}{\beta}DK_l'(qr)\right]\exp[i(\omega t \pm l\phi - \beta z)],$$

$$E_z(r,\phi,z,t) = CK_l(qr)\exp[i(\omega t \pm l\phi - \beta z)], \qquad (1.21)$$

$$H_r(r,\phi,z,t) = \frac{\beta}{q}\left[iDK_l'(qr) + \frac{\omega\varepsilon_2(\pm l)}{\beta}C\frac{K_l(qr)}{qr}\right]\exp[i(\omega t \pm l\phi - \beta z)],$$

$$H_\phi(r,\phi,z,t) = -\frac{\beta}{q}\left[(\pm l)D\frac{K_l(qr)}{qr} - \frac{i\omega\varepsilon_2}{\beta}CK_l'(qr)\right]\exp[i(\omega t \pm l\phi - \beta z)],$$

$$H_z(r,\phi,z,t) = DK_l(qr)\exp[i(\omega t \pm l\phi - \beta z)], \qquad (1.22)$$

where $K_l'(qr) = dK(qr)/d(qr)$ and $\varepsilon_2 = n_2^2\varepsilon_0$ denotes the dielectric constant in the cladding or in the surrounding medium.

The normalization constants A, B, C, and D as well as β, can be obtained by considering the boundary conditions. The tangential components $E_{\phi,z}$, $H_{\phi,z}$ have to be continuous at the core-cladding boundary

$$
\begin{aligned}
E_{\phi,z}(r = a)|_{\text{core}} &= E_{\phi,z}(r = a)|_{\text{cladding}}, \\
H_{\phi,z}(r = a)|_{\text{core}} &= H_{\phi,z}(r = a)|_{\text{cladding}}.
\end{aligned}
\tag{1.23}
$$

These considerations, together with Eqns. (1.19)–(1.22) yield the following relations for the constants A B, C and D

$$
\begin{aligned}
AJ_l(ha) - CK_l(qa) &= 0, \\
A\Big[\frac{i(\pm l)}{h^2 a} J_l(ha)\Big] + B\Big[-\frac{\omega\mu_0}{h\beta} J_l'(ha)\Big] + C\Big[\frac{i(\pm l)}{q^2 a} K_l(qa)\Big] + D\Big[-\frac{\omega\mu_0}{q\beta} K_l'(qa)\Big] &= 0, \\
BJ_l(ha) - DK_l(qa) &= 0, \\
A\Big[\frac{\omega\varepsilon_1}{h\beta} J_l'(ha)\Big] + B\Big[\frac{i(\pm l)}{h^2 a} J_l(ha)\Big] + C\Big[\frac{\omega\varepsilon_2}{q\beta} K_l'(qa)\Big] + D\Big[\frac{i(\pm l)}{q^2 a} K_l(qa)\Big] &= 0.
\end{aligned}
\tag{1.24}
$$

Equations (1.24) lead to a non-trivial solution provided that the determinant of their coefficients vanishes [34]. This requirement leads to the mode condition that determines the propagation constant β of each mode

$$
\Big(\frac{J_l'(ha)}{haJ_l(ha)} + \frac{K_l'(qa)}{qaK_l(qa)}\Big)\Big(\frac{n_1^2 J_l'(ha)}{haJ_l(ha)} + \frac{n_2^2 K_l'(qa)}{qaK_l(qa)}\Big) = l^2\Big[\Big(\frac{1}{ha}\Big)^2 + \Big(\frac{1}{qa}\Big)^2\Big]^2\Big(\frac{\beta}{k_0}\Big)^2,
\tag{1.25}
$$

Employing the solution for β, the following relations between the constants A, B, C and D, which determine the strength of the field components, can be found

$$
\begin{aligned}
\frac{C}{A} &= \frac{J_l(ha)}{K_l(qa)}, \\
\frac{B}{A} &= \frac{i\beta(\pm l)}{\omega\mu_0}\Big(\frac{1}{h^2 a^2} + \frac{1}{q^2 a^2}\Big)\Big(\frac{J_l'(ha)}{haJ_l(ha)} + \frac{K_l'(qa)}{qaK_l(qa)}\Big)^{-1}, \\
\frac{D}{A} &= \frac{C\,B}{A^2}.
\end{aligned}
\tag{1.26}
$$

Since the field amplitudes are related to the power of the electromagnetic field, A can be determined by accounting for the energy flux in z-direction via

$$
P_z = \frac{\omega}{2\pi}\int_0^{\frac{2\pi}{\omega}} dt \int_S S_z dS,
\tag{1.27}
$$

where P_z is the total power transmitted through the fiber and S_z is the component of the Poynting vector along the fiber axis (see Sect. 1.3.1).

Note that the ratio $B/A = E_r/E_\phi$ is complex accounting for a relative phase of $\pi/2$ between E_r and E_ϕ and thus for circular polarization of the transverse field. The term $\pm l$ in the equations above stems from the ansatz functions Eqns. (1.8) for the solution of the wave function in cylindrical coordinates. The $+$ $(-)$ sign refers to the solution with right-handed (left-handed) circulation of the transverse field $\vec{E}_\perp = (E_x, E_y)$ around the fiber axis. The solution for linearly polarized light can be composed as a superposition of left- and righthanded circular fields, i.e.

$$E_z^{lin} = \frac{1}{\sqrt{2}}(E_z^+ + E_z^-) \tag{1.28}$$

or can be obtained by using another type of ansatz function

$$E_z(r, \phi) = R(r)\cos[l\phi] \text{ or } E_z(r, \phi) = R(r)\sin[l\phi]. \tag{1.29}$$

In the next section the solutions of Eq. (1.25) for the propagation constants β and the associated modes will be discussed. These results will be used to derive the field intensity distribution and polarization orientation in the fundamental mode of an optical nanofiber.

1.2   Solution for the fields

The equation (1.25), which result from the boundary conditions, expresses the confinement of light in an optical fiber. The solution yields a discrete set of values for β, each of which represents a different propagation mode in the fiber. This result arises in general when treating confined waves in one or more dimensions, like e.g., the solutions of a particle confined in a potential well in quantum mechanics.

Rearranging equation (1.25), and making use of the relations

$$\begin{aligned} J_l'(x) &= J_{l-1}(x) - \frac{l}{x}J_l(x), \\ K_l'(x) &= -\frac{1}{2}[K_{l-1}(x) + K_{l+1}(x)], \end{aligned} \tag{1.30}$$

yields the two following sets of solutions

$$\frac{J_{l-1}(ha)}{haJ_l(ha)} = \left(\frac{n_1^2 + n_2^2}{2n_1^2}\right)\frac{K_{l-1}(qa) + K_{l+1}(qa)}{2qaK_l(qa)} + \frac{l}{(ha)^2} + R, \tag{1.31}$$

$$\frac{J_{l-1}(ha)}{haJ_l(ha)} = \left(\frac{n_1^2 + n_2^2}{2n_1^2}\right)\frac{K_{l-1}(qa) + K_{l+1}(qa)}{2qaK_l(qa)} + \frac{l}{(ha)^2} - R, \tag{1.32}$$

FIGURE 1.3: Plot of the right hand side (red) and left hand side (green) of equations (1.31) (left plot) and (1.32) (right plot) for $l = 1$ over the argument ha. The dashed lines mark the cut-off values of V. The intersections are solutions corresponding to either EH_{1m} or HE_{1m} modes.

with

$$R = \left[\left(\frac{n_1^2 - n_2^2}{2n_1^2}\right)^2 \left(\frac{K_{l-1}(qa) + K_{l+1}(qa)}{2qaK_l(qa)}\right)^2 + \left(\frac{l\beta}{n_1k_0}\right)^2 \left(\frac{1}{(qa)^2} + \frac{1}{(ha)^2}\right)^2\right]^{1/2}.$$

(1.33)

The $+(-)$ sign in Eq. (1.31 & 1.32) denotes the two sets of solutions, the HE $(-)$ and EH $(+)$ modes, representing the roots of equation (1.25) which is quadratic in $J'_l(ha)/haJ_l(ha)$. The designation of the modes is based on the contribution of E_z and H_z to the mode: E_z is larger (smaller) than H_z for the EH (HE) modes [34]. The equations 1.31 & 1.31 are transcendental in ha as well and can only be solved graphically or rather numerically by plotting each side as a function of ha using

$$(qa)^2 = a^2(n_1^2 - n_2^2)k_0^2 - (ha)^2.$$

(1.34)

Figure 1.3 shows the graphical solution of Eq. (1.31 & 1.32) for the EH_{1m} (HE_{1m}) modes. The left- and right-hand sides of Eq. (1.31 & 1.32) have been plotted as a function of the parameter ha for $l = 1$. Each crossing point represents one propagating mode in the fiber. The corresponding propagation constant β is determined by $(ha)_\times$, where both curves cross, via

$$\beta = \sqrt{n_1^2 k_0^2 - \frac{(ha)_\times}{a}}.$$

(1.35)

Each set of modes exhibits different solutions depending on the value l. These modes are labeled as EH_{lm} and HE_{lm}, where m denotes the different solutions of Eq. (1.31 & 1.32) for a fixed l. For the two special cases with $l = 0$ a differentiated nomenclature is used: EH_{0m} alias TM, and HE_{0m} alias TE. The notation TE and (TM) refers to the vanishing E_z (H_z) components of the *transverse electric* (*transverse magnetic*) modes. Whereas the hybrid modes EH and HE have six non vanishing field components, the TM and TE modes have only three [39].
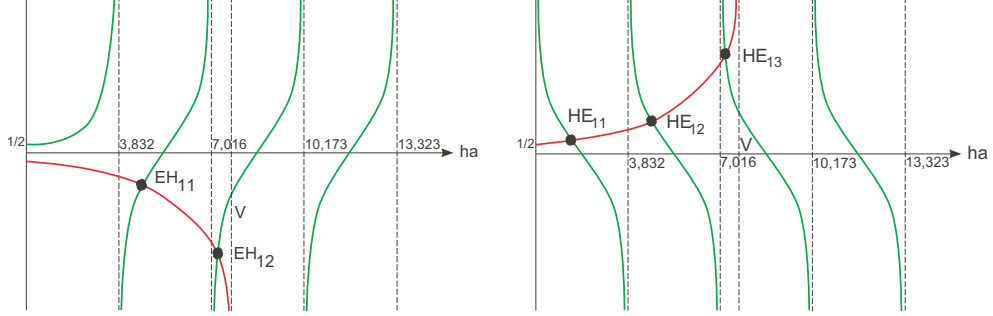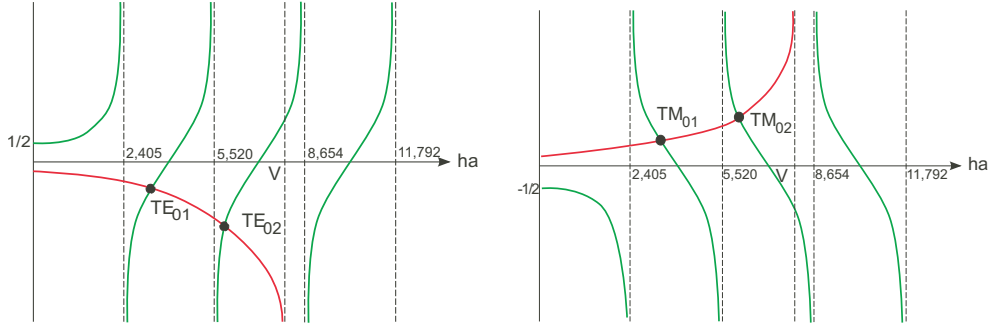
FIGURE 1.4: Plot of the right hand side (red) and left hand side (green) of equations (1.31) (left plot) and (1.32) (right plot) for $l = 0$ over the argument ha. The dashed lines mark the cut-off values of V. The intersections are the TE_{0m} and TM_{0m} modes, respectively.

As pointed out in [39], in geometric optics hybrid modes can be interpreted in terms of *skew rays*, i.e. circulating light trajectories around the fiber axis, whereas the transverse modes TM and TE imply non-rotating ray trajectories, that lie in the meridional plane. Hence, the number l can be associated with the z-component of the orbital angular momentum of the propagating electromagnetic field [34, 45].

From the plots in Figs. 1.3 and 1.4 it is evident that for a given l, the number of solutions is determined by $ha = V$, the position of the singularity on the righthand side of Eq. (1.31). Here, V denotes the fundamental parameter for the fiber-field system

$$V = k_0 a \sqrt{n_1^2 - n_2^2}. \tag{1.36}$$

It can be shown that all modes (apart from HE_{11}) have a cut-off value in V, which can be found by the m roots of $J_l(ha) = 0$ (dashed vertical lines in Figure 1.3 and 1.4). At the cut-off, each propagation constant takes the value of $\beta \equiv k_0 n = k_0 n_2$, where $n = \beta/k_0$ is the mode index, i.e., the effective refractive index of the corresponding mode, see Fig. 1.5. As a mode approaches cut-off, the fields penetrate deeply into the cladding medium. Thus, the mode is poorly confined and poorly guided, and most of the energy propagates in medium 2, leading to $n = n_2$. Similar argument holds for far above cut-off, where the mode is tightly bound to the core and thus $n = n_1$.

Below the cut-off value of $V = 2.405$ only the fundamental mode (HE_{11}) can propagate. Hence, single mode condition is reached for a given wavelength λ, if the radius of the fiber is small enough that only the fundamental mode can propagate. For many applications requiring a well-defined phase front of the propagating light (e.g. telecommunication, interferometry etc.), single-mode operation is compulsory. In the present work, the light-induced trapping potential is formed by two fields of
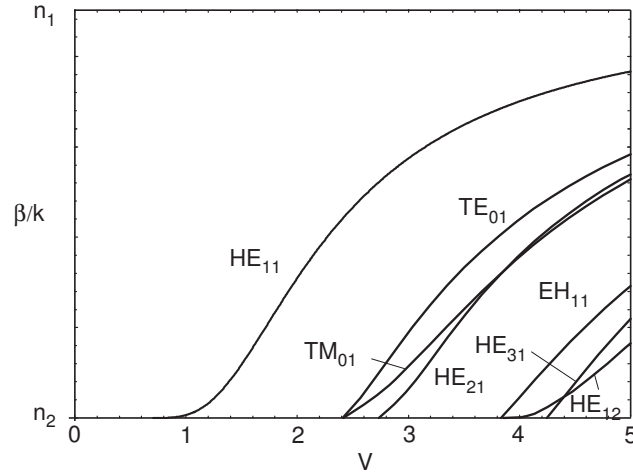
FIGURE 1.5: Normalized propagation constant β/k as a function of V for a few of the lowest-order modes of a step-index fiber [34], where k denotes the vacuum wavenumber.

different wavelengths, both of which propagate in the fundamental mode HE_{11} of a sub-wavelength optical fiber. Therefore, the analysis of the field distribution in the next section covers only the HE_{11} mode. Note that it has been separately proposed to realize a light-induced trapping potential which is based on the interference of two low-order modes of a blue detuned evanescent light field [40]. Details of this approach can be found in [39–41] and are not a part of this work.

1.3   Field distribution of the HE_{11} mode in and outside a nanofiber

In this section the intensity distribution and polarization orientation of the fundamental HE_{11} mode of an optical nanofiber are discussed. The solutions of Maxwell's equations Eq. (1.10) permit the exact modeling of the fields inside and outside a fiber with a diameter smaller than the wavelength of the guided light [32].

1.3.1 HE_{11} mode with rotating polarization

The field equations of the fundamental HE_{11} mode with rotating polarization in terms of the electric field $\vec{E}$ in and outside the fiber is given by
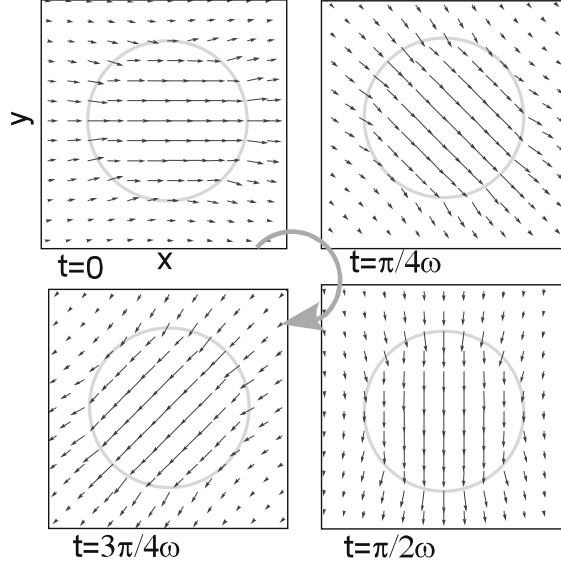
FIGURE 1.6:   Vectorial   plot   of   the   transverse   field   components
$\vec{E}_\perp = (E_x(x, y), E_y(x, y))$ at $z = 0$, for $t = 0$, $t = \pi/4\omega$, $t = \pi/2\omega$, $t = 3\pi/4\omega$
respectively for a 250-nm radius vacuum-clad glass-fiber ($n_1 = 1.46$) transmitting
σ^+-polarized light at a wavelength of $\lambda = 852$ nm.

$$E_r(r, \phi, z, t) = - iA\frac{\beta_{11}}{2h_{11}}[(1 - s_{11})J_0(h_{11}r) - (1 + s_{11})J_2(h_{11}r)]$$
$$\exp[i(\omega t \pm \phi - \beta_{11}z)],$$
$$E_\phi(r, \phi, z, t) = \pm A\frac{\beta_{11}}{2h_{11}}[(1 - s_{11})J_0(h_{11}r) + (1 + s_{11})J_2(h_{11}r)]$$
$$\exp[i(\omega t \pm \phi - \beta_{11}z)],$$
$$E_z(r, \phi, z, t) = AJ_1(h_{11}r)\exp[i(\omega t \pm \phi - \beta_{11}z)], \qquad (1.37)$$

for $r < a$ (inside the fiber), and

$$E_r(r, \phi, z, t) = - iA\frac{\beta_{11}}{2q_{11}}\frac{J_1(h_{11}a)}{K_1(q_{11}a)}[(1 - s_{11})K_0(q_{11}r) + (1 + s_{11})K_2(q_{11}r)]$$
$$\exp[i(\omega t \pm \phi - \beta_{11}z)],$$
$$E_\phi(r, \phi, z, t) = \pm A\frac{\beta_{11}}{2q_{11}}\frac{J_1(h_{11}a)}{K_1(q_{11}a)}[(1 - s_{11})K_0(q_{11}r) - (1 + s_{11})K_2(q_{11}r)]$$
$$\exp[i(\omega t \pm \phi - \beta_{11}z)],$$
$$E_z(r, \phi, z, t) = A\frac{J_1(h_{11}a)}{K_1(q_{11}a)}K_1(q_{11}r)\exp[i(\omega t \pm \phi - \beta_{11}z)], \qquad (1.38)$$

for $r > a$ (outside the fiber),

FIGURE 1.7: Ellipticity $\varepsilon = |E_r|/|E_\phi|$ of the polarization of the electric fields versus the radial distance r/a.

where

$$h_{11} = \sqrt{k_0^2 n_1^2 - \beta_{11}^2},$$

$$q_{11} = \sqrt{\beta_{11}^2 - k_0^2 n_2^2},$$

$$s_{11} = \left[\frac{1}{(h_{11}a)^2} + \frac{1}{(q_{11}a)^2}\right]\left[\frac{J_1'(h_{11}a)}{h_{11}aJ_1(h_{11}a)} + \frac{K_1'(q_{11}a)}{q_{11}aK_1(q_{11}a)}\right]^{-1}. \quad (1.39)$$
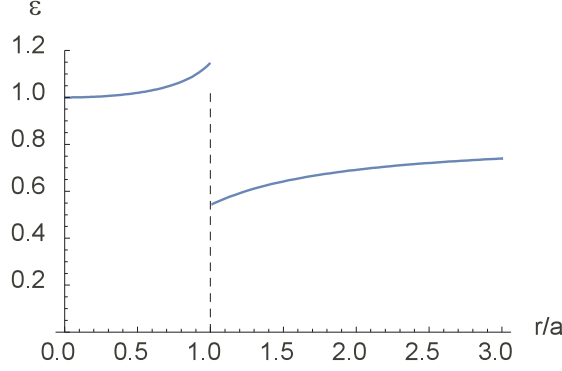
Note that from the relation $E_r/|E_r| = \pm i E_\phi/|E_\phi|$, obtained from Eq.(1.37)–(1.38), the radial and tangential components E_r and E_ϕ have a phase difference of $\pi/2$. Therefore, the orientation of the transverse field $\vec{E}_\perp = (E_r, E_\phi)$ rotates in time along the fiber axis. In Fig. 1.6 the vectorial field plot of $\vec{E}_\perp(t, z = 0)$ for different times t shows the corresponding phases of rotation. However, this rotation is not perfectly circular but elliptical and the ellipticity varies in space. Moreover, due to the non-vanishing longitudinal component E_z, the rotation of $\vec{E}$ in the transverse plane is superimposed with an elliptical rotation in a plane parallel to the fiber axis z. Thus, the normal vector of the polarization ellipse is not parallel but tilted by the angle $\alpha = \arctan(|E_z|/|E_\phi|)$ with respect to the fiber axis. The ellipticity $\varepsilon = |E_r|/|E_\phi|$, i.e., the aspect ratio of the major and minor axes, versus the radial distance is shown in Fig. 1.7. Inside the core and far outside in the cladding region the HE_{11} mode is almost purely circularly polarized. The deviation from pure circular polarization, however, increases when approaching the surface of the fiber. This behavior originates from the boundary conditions for the electric field [32], which lead to a discontinuity in the E_r component at the fiber surface, while the tangential components E_ϕ and E_z remain continuous. Hence, this sets the radial orientation of the ellipse, its major (minor) axis is directed perpendicular (tangential) to the fiber surface.
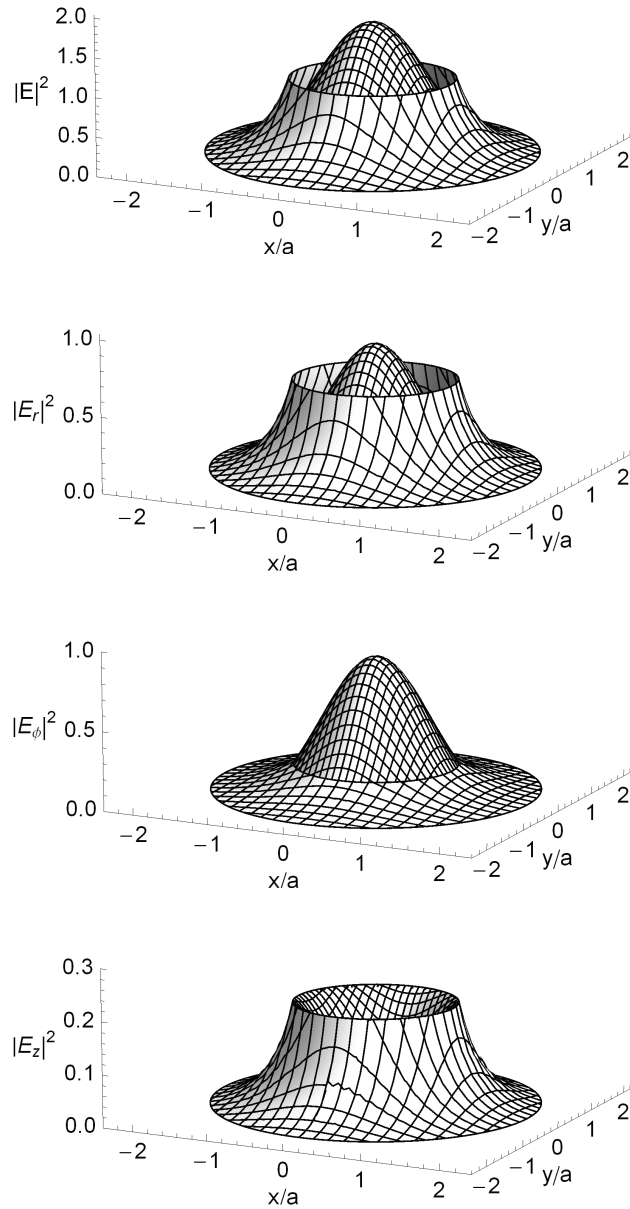
FIGURE 1.8: Normalized intensities $|E|^2$ in units of $|E(r = a)|^2$ including the cylindrical-coordinate components $|E_r|^2, |E_\phi|^2, |E_z|^2$ of the cycle averaged squared electric field modulus in the HE$_{11}$ mode for rotating polarization, plotted in the transverse plane (x, y).

(a)

(b)
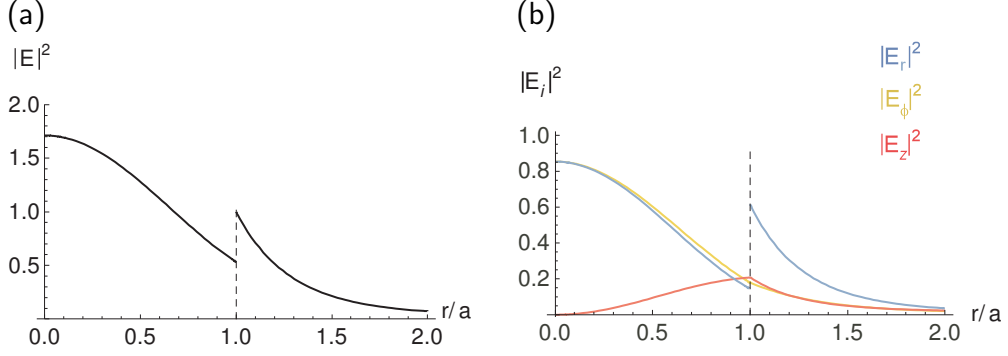
FIGURE 1.9: Radial intensity distribution (a) $|E(r)|^2$ and (b) $|E_i(r)|^2$ of the cylindrical-coordinate components of the HE_{11} mode for rotating polarization, normalized by $|E(r = a)|^2$.

Intensity distribution

The boundary conditions for the normal component E_r also lead to a discontinuity of the intensity at the surface of the fiber. The large difference in refractive index at the boundary of core and cladding causes a proportional jump in intensity, leading to an enhancement of the field strength outside the fiber. In the following the intensity will be given in terms of the electric field via:

$$I = \frac{1}{2} c \varepsilon_0 |\vec{E}|^2. \tag{1.40}$$

Here, $|\vec{E}|^2$ denotes the squared modulus of the electric field averaged over one oscillation period. Thus, the intensity distribution of the HE_{11} mode is given by

$$\left|\vec{E}(r)\right|^2_{\text{in}} = \frac{A^2 \beta_{11}^2}{2 h_{11}^2} \left[(1 - s_{11})^2 J_0^2(h_{11}r) + (1 + s_{11})^2 J_2^2(h_{11}r) + 2 \frac{h_{11}^2}{\beta_{11}^2} J_1^2(h_{11}r) \right], \tag{1.41}$$

for $r < a$, and

$$\left|\vec{E}(r)\right|^2_{\text{out}} = \frac{A^2 \beta_{11}^2}{2 q_{11}^2} \frac{J_1^2(h_{11}a)}{K_1^2(q_{11}a)} \left[(1 - s_{11})^2 K_0^2(q_{11}r) + (1 + s_{11})^2 K_2^2(q_{11}r) + 2 \frac{q_{11}^2}{\beta_{11}^2} K_1^2(q_{11}r) \right], \tag{1.42}$$

for $r > a$.

In figure 1.8, the corresponding three dimensional plot of the intensity distribution $|\vec{E}(r)|^2$ of the HE_{11} mode for rotating polarization in the transverse plane is shown. This example refers to a 250-nm radius silica-fiber ($n_1 = 1.45$), surrounded by vacuum ($n_2 = 1$) and transmitting circularly polarized light of 852-nm wavelength.

Due to a full revolution of $\vec{E}$ within one cycle, the cycle averaged squared modulus of the electric field, in Eq. (1.41) does not depend on the azimuthal coordinate ϕ. The same holds true for the constituents of the total intensity $|E_r|^2, |E_\phi|^2, |E_z|^2$, whose angular dependence is averaged out within one oscillation period. Hence, the intensity of the evanescent field in the HE$_{11}$ mode, excited by circularly polarized light, is distributed cylindrically symmetrically around the fiber.

Figure 1.9 shows the radial intensity distribution on the inside and the outside of a vacuum-clad fiber for the HE$_{11}$ mode. Here, $\left|\vec{E}(r)\right|^2$ is normalized to maximal intensity $\left|\vec{E}(r=a)\right|^2$ outside the fiber. Inside the fiber, the intensity is maximal at the center of the fiber ($r = 0$) and decays towards the surface. At the fiber surface, however, the intensity is enhanced due to the discontinuity of E_r and decays evanescently outside the fiber. The tangential components $E_{\phi,z}$ are continuous at the surface. Their contributions to the total intensity outside the fiber are about 25% each. The decay length of the evanescent field, given by $\Lambda = 1/q_{11}$ (Eq. 1.39) scales with the wavelength of transmitted light. This wavelength dependency is critical to the two-color trapping scheme and will be discussed in Sect. 2.3.

Power density

The normalization constant A of the field amplitudes in Eqs.(1.41 & 1.42) is related to the total power of the light propagating in the fiber via the Poynting vector

$$\langle\vec{S}\rangle = \frac{1}{2}\mathrm{Re}\left[\vec{E} \times \vec{H}^*\right]. \tag{1.43}$$

The z-component of the cycle-averaged Poynting vector $\langle S_z\rangle$, quantifies the energy flux of the electromagnetic field in the propagation direction, i.e., along the fiber axis. Integration of $\langle S_z\rangle$ over the transverse plane leads to the following expression for the power propagating inside and outside the fiber [44]

$$
\begin{aligned}
P_{\mathrm{in}} &= \int_0^{2\pi} d\phi \int_0^a \langle S_z\rangle_{\mathrm{in}} r dr, \\
P_{\mathrm{out}} &= \int_0^{2\pi} d\phi \int_a^\infty \langle S_z\rangle_{\mathrm{out}} r dr.
\end{aligned}
\tag{1.44}
$$

Using Eqns. (1.20), (1.22), and Eqns. (1.37), (1.38), the Poynting vector of the electromagnetic field in the HE$_{11}$ mode can be easily calculated. The resulting relation between the total transmitted power $P = P_{\mathrm{in}} + P_{\mathrm{out}}$ (Eq. (1.44)) and the normalization constant A reads

$$A = \sqrt{\frac{4\mu_0\omega P}{\pi a^2 \beta_{11}}}\left(D_{\mathrm{in}} + D_{\mathrm{out}}\right)^{-1/2}, \tag{1.45}$$

with

$$D_{\text{in}} = \Big[(1 - s_{11})(1 + (1 - s_{11})\frac{\beta_{11}^2}{h_{11}^2})(J_0^2(h_{11}a) + J_1^2(h_{11}a)) +$$

$$+ (1 + s_{11})(1 + (1 + s_{11})\frac{\beta_{11}^2}{h_{11}^2})(J_2^2(h_{11}a) - J_1(h_{11}a)J_3(h_{11}a))\Big], \qquad (1.46)$$

$$D_{\text{out}} = \frac{J_1^2(h_{11}a)}{K_1^2(q_{11}a)}\Big[(1 - s_{11})(1 - (1 - s_{11})\frac{\beta_{11}^2}{q_{11}^2})(K_0^2(q_{11}a) - K_1^2(q_{11}a)) +$$

$$+ (1 + s_{11})(1 - (1 + s_{11})\frac{\beta_{11}^2}{q_{11}^2})(K_2^2(q_{11}a) - K_1(q_{11}a)K_3(q_{11}a))\Big]. \qquad (1.47)$$

Where $D_{\text{in}}/(D_{\text{in}} + D_{\text{out}})$ and $D_{\text{out}}/(D_{\text{in}} + D_{\text{out}})$ are the fractions of the power of the fields that propagate inside and outside the fiber. P is the total power of the transmitted light, which can be directly measured at the fiber output.

1.3.2   HE$_{11}$ mode with quasi-linear polarization

From Eqns. (1.19 & 1.21) in Chapter 1.1, the solutions of the quasi-linearly polarized fields can be expressed in terms of the superposition of two circular fields

$$E_i^{(\text{lin})} = \frac{1}{\sqrt{2}}(E_i^+ + E_i^-), \quad i \in (r, \phi, z) \qquad (1.48)$$

The $+(-)$ sign in the equations above denotes the solution with right-handed (left-handed) rotation of the polarization around the fiber axis, respectively. In cartesian coordinates the fields become

$$E_x(r, \phi, z, t) = A_{\text{lin}}\frac{\beta_{11}}{2h_{11}}[(1 - s_{11})J_0(h_{11}r)\cos(\varphi_0)$$
$$- (1 + s_{11})J_2(h_{11}r)\cos(2\phi - \varphi_0)]\exp[i(\omega t - \beta_{11}z)],$$
$$E_y(r, \phi, z, t) = A_{\text{lin}}\frac{\beta_{11}}{2h_{11}}[(1 - s_{11})J_0(h_{11}r)\sin(\varphi_0)$$
$$- (1 + s_{11})J_2(h_{11}r)\sin(2\phi - \varphi_0)]\exp[i(\omega t - \beta_{11}z)],$$
$$E_z(r, \phi, z, t) = iA_{\text{lin}}J_1(h_{11}r)\cos(\phi - \varphi_0)\exp[i(\omega t - \beta_{11}z)] \qquad (1.49)$$
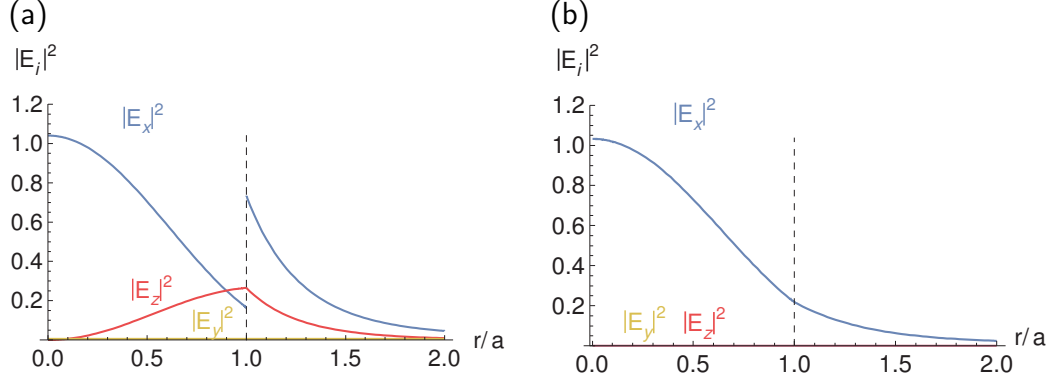
(a)

$|E_i|^2$

(b)

$|E_i|^2$

FIGURE 1.10: Radial intensity distribution $|E_i(r)|^2$ of the carthesian-coordinate components of the HE$_{11}$ mode for linear x-polarization, normalized to $|E(r=a)|^2=1$, (a) shown in $(x, y = 0)$ direction, and (b) shown in $(x = 0, y)$ direction.

for $r < a$ (inside the fiber), and

$$
E_x(r,\phi,z,t) = A_\mathrm{lin}\frac{\beta_{11}}{2q_{11}}\frac{J_1(h_{11}a)}{K_1(q_{11}a)}[(1-s_{11})K_0(q_{11}r)\cos(\varphi_0)
$$
$$
+ (1+s_{11})K_2(q_{11}r)\cos(2\phi-\varphi_0)]\exp[i(\omega t - \beta_{11}z)],
$$
$$
E_y(r,\phi,z,t) = A_\mathrm{lin}\frac{\beta_{11}}{2q_{11}}\frac{J_1(h_{11}a)}{K_1(q_{11}a)}[(1-s_{11})K_0(q_{11}r)\sin(\varphi_0)
$$
$$
+ (1+s_{11})K_2(q_{11}r)\sin(2\phi-\varphi_0)]\exp[i(\omega t - \beta_{11}z)],
$$
$$
E_z(r,\phi,z,t) = iA_\mathrm{lin}\frac{J_1(h_{11}a)}{K_1(q_{11}a)}K_1(q_{11}r)\cos(\phi-\varphi_0)\exp[i(\omega t - \beta_{11}z)], \qquad (1.50)
$$

for $r > a$ (outside the fiber).

Here, q_{11}, h_{11} and s_{11} are identical to those defined in Sec. 1.3.1. The normalization constant A_lin is related to the maximum amplitude of the electric field via $A_\mathrm{lin} = \sqrt{2}A$, with A defined for rotating polarization given in Sec. 1.3.1. The angle φ_0 describes the orientation of the transverse $\vec{E}_\perp = (E_x, E_y)$ field: $\varphi_0 = 0$ leads to polarization in the x-direction and $\varphi_0 = \pi/2$ to polarization in the y-direction. The designation quasi-linear polarization refers to the non-vanishing longitudinal component E_z of the HE$_{11}$ mode. Note that E_z is out of phase by $\pi/2$ with respect to the perpendicular components E_x and E_y. This phase difference causes an elliptical rotation of the $\vec{E}$ field in a plane parallel to the fiber axis z. The magnitude of E_z varies radially as well as azimuthally as does the ellipticity. For $\varphi_0 - \phi = 0$, and π, i.e., in the plane of polarization, E_z is substantial close to the fiber surface (see Fig. 1.10). In the plane perpendicular to polarization ($\varphi_0 - \phi = \pi/2$ and $3\pi/2$), however, E_z is zero and hence the polarization is purely linear.

In Fig. 1.11(a) the transverse field vectors $\vec{E}_\perp = (E_x, E_y)$ at $t = 0$ and $z = 0$ as functions of (x, y) are plotted. This example refers to a 250-nm radius vacuum-clad ($n_2 = 1$) glass-fiber ($n_1 = 1.46$), transmitting light of 852 nm, polarized in the x-direction. As can be seen in this plot, the electric field for the linearly polarized HE_{11} mode is perpendicular to the fiber surface for $\phi = 0$ and $\phi = \pi$ and parallel for $\phi = \pi/2$ and $\phi = 3\pi/2$. However, due to the boundary conditions for $\vec{E}$, the normal component is discontinuous at the fiber surface. Therefore, the circular curvature of the surface of the fiber dictates a sinusoidal variation of the polarization orientation angle $\theta = \arctan[E_y/E_x]$ with the azimuthal angle ϕ (see Fig. 1.11(b). The deviations of the polarization orientation from x-direction can be substantial for $\phi \neq n\frac{\pi}{2}$, $n = 0, 1, 2...$, and are highest at the fiber surface. For an increasing distance from the surface the deviation from x-polarization decreases. As an example, at a distance of $r = 2a$ from the fiber surface (i.e., at about the trap distance) and $\phi = \pi/4$ the ratio (E_y/E_x) is about 0.1 yielding $\theta = 0.1/2\pi$.

The boundary conditions for the $\vec{E}$ fields also result in an azimuthal dependency of the field distribution. Due to the discontinuity of the normal component at the boundary, linear, i.e., non-rotating, polarization breaks the cylindrical symmetry of the system. Thus, the evanescent field is maximal where $\vec{E}_\perp$ is normal and minimal where $\vec{E}_\perp$ is tangential to the fiber surface.

Following from Eqs. (1.49) and (1.50) the square of the electric field modulus for the HE_{11} mode averaged over one oscillation period is given by

$$\left|\vec{E}(r, \phi)\right|^2_{\text{in}} = \frac{A^2_{\text{lin}}\beta^2_{11}}{4h^2_{11}} \Big[(1 - s_{11})^2 J^2_0(h_{11}r) + (1 + s_{11})^2 J^2_2(h_{11}r) + 2\frac{h^2_{11}}{\beta^2_{11}} J^2_1(h_{11}r)$$
$$+ 2\Big(\frac{h^2_{11}}{\beta^2_{11}} J^2_1(h_{11}r) - (1 + s_{11})(1 - s_{11}) J_0(h_{11}r) J_2(h_{11}r) \Big) \cos[2(\phi - \varphi_0)] \Big],$$

$$(1.51)$$

$$\left|\vec{E}(r, \phi)\right|^2_{\text{out}} = \frac{A^2_{\text{lin}}\beta^2_{11}}{4q^2_{11}} \frac{J^2_1(h_{11}a)}{K^2_1(q_{11}a)}$$
$$\times \Big[(1 - s_{11})^2 K^2_0(q_{11}r) + (1 + s_{11})^2 K^2_2(q_{11}r) + 2\frac{q^2_{11}}{\beta^2_{11}} K^2_1(q_{11}r)$$
$$+ 2\Big(\frac{q^2_{11}}{\beta^2_{11}} K^2_1(q_{11}r) + (1 + s_{11})(1 - s_{11}) K_0(q_{11}r) K_2(q_{11}r) \Big) \cos[2(\phi - \varphi_0)] \Big],$$

$$(1.52)$$

(a)   (b)

FIGURE 1.11:   (a) Vectorial plot of the transverse field components
$\vec{E}_\perp = (E_x(x,y), E_y(x,y))$ at $t = 0$, $z = 0$ for a 250-nm radius vacuum-clad
glass-fiber ($n_1 = 1.46$) transmitting 852-nm wavelength light polarized in the x-
direction. (b) Polarization orientation angle as a function of the azimuthal angle
$\varphi = \arctan x/y$ for three different radial distances.

where $\left|\vec{E}\right|^2 = |E_x|^2 + |E_y|^2 + |E_z|^2$. The intensity distribution and the cartesian
components $|E_{x,y,z}(r,\phi)|^2$ according to equation (1.49) and (1.50) for the HE$_{11}$
mode with polarization in the x-direction ($\varphi_0 = 0$) is shown in Fig. 1.12. Here, the
same parameters as in Sect. 1.3.1 are used. The maximum total intensity of the
evanescent field is found at $\phi = 0$ and is composed of $|E_x(r,0)|^2 + |E_z(r,0)|^2$, which
is apparent from the term $\cos[2(\phi - \varphi_0)]$ in Eqs. (1.51) and (1.52). The minimum
total intensity, at $\phi = \pi/2$, consists only of the x-component $|E_x(r,\pi/2)|^2$, which
is about 30% of the maximum value (compare Fig. 1.10).

In contrast to weakly focused and freely propagating light beams, the intensity as
well as the polarization of light in the HE$_{11}$ mode varies azimuthally. Many applica-
tions involving light-atom interaction, however, demand a well-defined orientation
of the polarization, e.g., for the optical pumping of atoms. In view of these circum-
stances, a convenient approach may be to localize the atoms where the probing field
$\vec{E}$ is parallel to the surface of the fiber and thus purely linearly polarized. As I will
show in Sect. 2.3, a linear array of trapping sites for atoms can be accomplished
by means of light-induced dipole forces and by utilizing the azimuthal dependency
of the evanescent field of the quasi-linearly polarized HE$_{11}$ mode, which enables
strong azimuthal confinement of atoms trapped in the vicinity of the nanofiber.

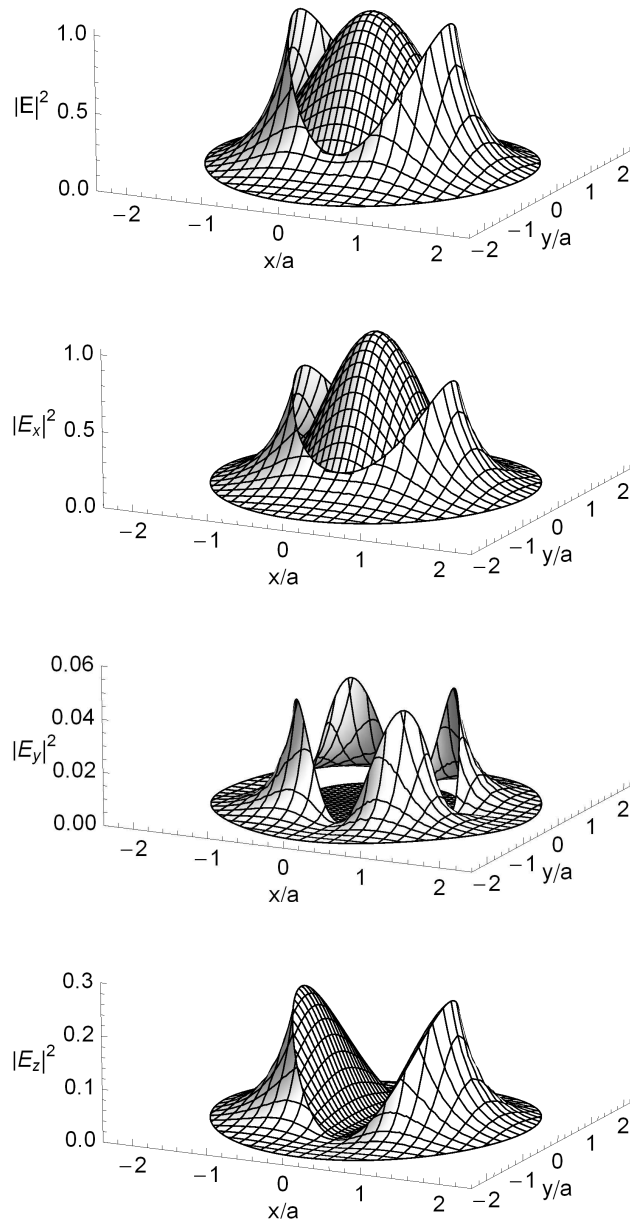FIGURE 1.12: Normalized intensities $|E|^2$ in units of $|E(x = a, y = 0)|^2$ including of the Cartesian-coordinate components $|E_x|^2, |E_y|^2, |E_z|^2$ of the cycle averaged squared electric field modulus in the HE_{11} mode for quasi-linear polarization, plotted in the transverse plane (x, y).
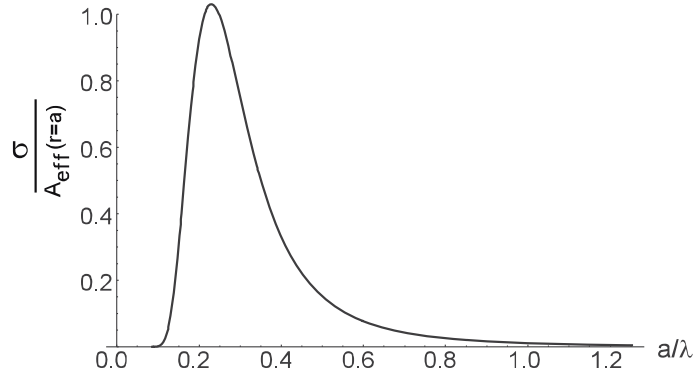
FIGURE 1.13: Normalized intensity of the evanescent field $I(r = a)/P = 1/A_{\text{eff}}(r = a)$ in units of $1/\sigma = (3\lambda^2/2\pi)^{-1}$ as a function of the normalized fiber radius a/λ. Calculated for circularly polarized light and assuming a refractive index of 1.46. The resulting functional form holds universally for any λ.

Confinement of the fiber-guided light

In the upper examples, light is considered to be guided by a fiber with diameter $2a$ which is smaller than the light wavelength. Such strong transversal confinement of light results in a significant intensity of the field outside the fiber. By employing the analysis from Sect. 1.1, it can be shown that the intensity of the evanescent field increases for decreasing fiber diameter and takes a maximum value when $a/\lambda = 0.23$ (see Fig. 1.13) [36]. A further reduction of fiber radius makes the mode only weakly guided, i.e., the mode area A_{eff} diverges and the intensity converges to zero. This result holds universally for all wavelengths in the visible and near-infrared region, i.e., where the refractive index of the glass fiber is about 1.46.

In the optimal case, the mode field area $A_{\text{eff}}(= P/I)$ is a significant fraction of the resonant absorption cross-section $\sigma \simeq 3\lambda^2/2\pi$ of alkali-atoms. Hence, atoms in close vicinity of an appropriate fiber can be efficiently coupled to the fiber-guided light via the evanescent field. By the same argument, relatively low powers of in-coupled (far off-resonant) dipole lasers are sufficient in order to form the light-induced potentials necessary for trapping the atoms (see Sect. 2.3).

In the present work, a fiber with 250-nm radius is used in order that a/λ be close to 0.23 for the various wavelengths employed (1064, 852 and 780 nm), thus ensuring single-mode operation and strong confinement.

1.4   Tapered optical fibers (TOFs)

The theoretical considerations of light propagation in an optical nanofiber have been discussed in the previous section. Such nanofibers can be realized as the waist of tapered optical fibers (TOFs) that optimally match the mode of a standard single mode optical fiber with the fundamental nanofiber mode [37].
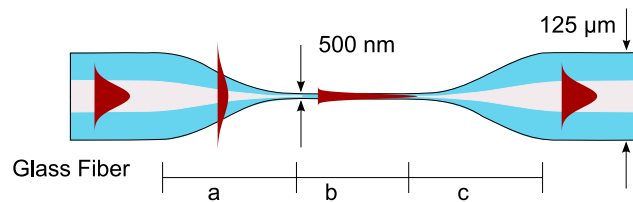
FIGURE 1.14: Schematic of a tapered optical fiber (TOF) showing the light propagation and conversion of the fundamental mode in the tapered region (a) to the nanofiber waist (b) and back again to the fiber guided mode (c). The intensity profiles of the guided modes are represented by the red curves.

Figure 1.14 shows a schematic of a tapered optical fiber (TOF) with a four-part structure; the fiber waist (b) surrounded by two taper transitions (a) and (c) to the original fiber. The intensity of the corresponding mode of light propagation is represented by the red filled curves. In the unprocessed part of the single mode TOF, the light is guided inside the core via total internal reflection at the core cladding boundary. This propagation mode is often approximated by the weakly guided and linearly polarized fundamental mode LP_{01} [34]. In the tapered sections the weakly guided LP_{01} mode of the unstretched fiber is adiabatically transformed into the strongly guided HE_{11} mode of the nanofiber and back to the LP_{01} mode on the opposite side of the TOF [11]. The decreasing diameter of the core in the first taper leads to a compression of the guided mode until the core radius becomes the size of about the wavelength of the light, whereby the guided mode expands into the cladding. In this case, the glass cladding acts as the new core and the surrounding medium becomes the new cladding. Further decreasing the fiber diameter causes the mode field to be more and more laterally confined until the light approaches the waist. Thus, the intensity of the light field at the sub-wavelength diameter waist is very high and is accessible from the outside via the evanescent field. At the second taper transition the mode transformation is accomplished in reverse. In order to minimize transmission loss, the taper transitions have to be carefully shaped in order to prevent energy transfer to higher order modes in the cladding which are not guided by either the nanofiber waist or the fiber core. In various work, the adiabadicity criteria of taper transitions were analyzed [11–14], however, the realization of highly efficient TOFs is technologically challenging.
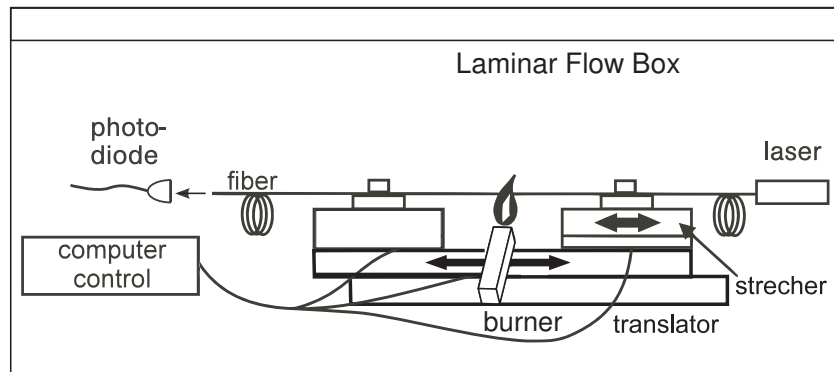
FIGURE 1.15: Schematic of the pulling rig [37]. A standard glass-fiber is clamped between two stacked translation stages, which move and stretch the glass-fiber above the flame of a stationary gas burner. The pulling procedure is performed under clean room conditions in a laminar flow box.

Flame pulling of TOFs

The TOF being used throughout this work was produced in a computer-controlled fiber pulling rig, which is described in detail in the Ph.D. thesis of F. Warken [37]. A standard optical glass fiber (Liekki 6/125 Passive) with 6 μm core- and 125 μm outer diameter is tapered to a 500-nm diameter and 5-mm long waist, yielding an overall transmission through the TOF of 97% (see Fig. 1.17).

The pulling process of this TOF can be briefly described as follows: The polymer coating is removed and the glass fiber is carefully cleaned at the tapering position before being fixed in the pulling rig. The pulling rig consists of two linear translation stages, the translator and the stretcher, that allow sub-micrometer actuation of the positioning with precisely aligned V-groove holders, on which the fiber is clamped and tightened (see Fig. 1.15). An electronically controlled hydrogen-oxygen burner is placed between these two holders, which provides a very clean and laminar flame. The flame heats approximately 1 mm of the fiber to about 1500°C, making it soft and malleable, while the translator moves the fiber back and forth above the flame as the stretcher simultaneously elongates it. Due to volume conservation the fiber diameter is thus gradually reduced. This so-called "flame brushing technique" allows one to produce almost any profile and waist diameter of the TOFs [37]. The required trajectories of the traveling stages are calculated by simulating the pulling process on a computer. In particular, linear conical tapers with a constant slope were found empirically to be optimal for the fiber mentioned above. At the crucial diameters, below 40 μm, where the core mode is transformed into a cladding mode, a very shallow slope should ensure impedance matching, thus minimizing transmission loses.

(a)

(b)
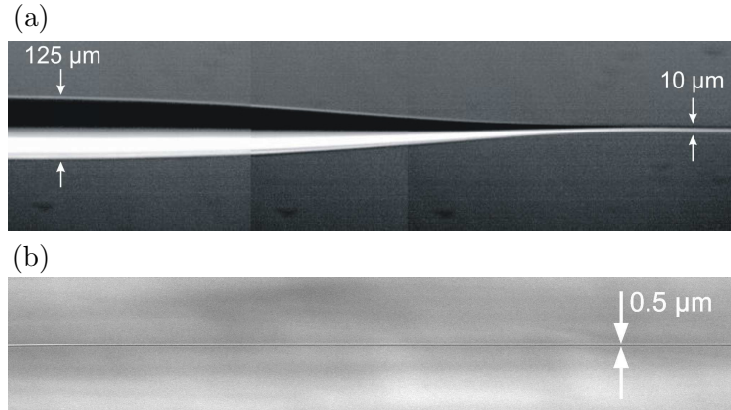
FIGURE 1.16: (a) Optical microscope picture of a TOF. (b) SEM picture of the waist of a TOF. The diameter of the waist was measured to be 0.5 μm.

In order to find the best taper parameters laser light was launched into the fiber and its transmission was monitored during the pulling process (see Fig.1.17). An optimum slope angle was found at 1.5 mrad with transmission of better than 99% for a 500-nm diameter waist [42], while keeping the length of the TOF reasonably short (≈ 7 cm). Furthermore, by monitoring the Rayleigh scattered light from the nanofiber, we have found that the polarization of the transmitted light is not significantly changed in the taper transition and the nanofiber waist. We are even able to precisely align the polarization of the fiber-guided light on the nanofiber waist with a residual ellipticity of less than one percent for a non-polarization maintaining fiber (see, Sect. 3.3.3).

Figure 1.16 shows exemplarily a micrograph of a taper transition (a), and a SEM (Scanning Electron Microscope) picture of the waist of a TOF with a diameter of 500 nm (b) [37]. Several electron microscopic imaging have also been produced [37,39], showing a reproducible and homogenous waist diameter as well as a surface roughness below the resolution limit of a SEM (≈ 1 nm).

These unique physical properties in conjunction with a high transmission makes the TOF ideally suited for realization of a two-color evanescent wave trap around the sub-wavelength diameter waist. The most critical factor in this context turns out to be the robustness against fusing in vacuum. However, for optimal conditions, i.e., a perfectly straight TOF, and gently stretched nanofiber, these TOFs are capable to carry few hundreds of milliwatts of laser light in vacuum without showing any degradation of the fiber.
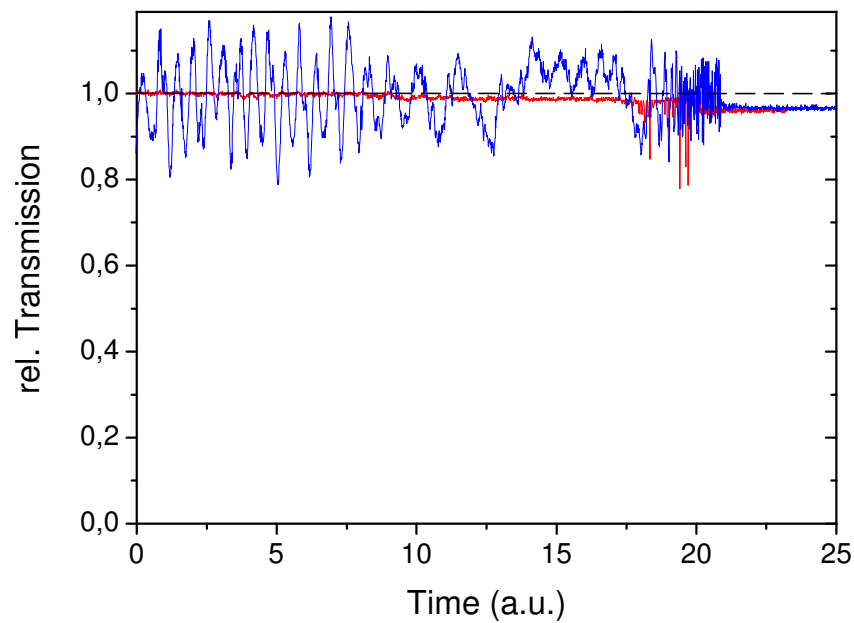
FIGURE 1.17: Transmission of a 780 nm (blue) and 850 nm (red) laser light through a TOF during the pulling procedure as a function of time. The oscillations of the transmission at 780 nm at the beginning are caused by interferences with higher order modes. The final diameter of the fiber waist is 500 nm (t=22), allowing single mode transmission of 97% for both wavelengths.

Chapter 2

Atom-field interaction

In order to exploit the unique quantum properties of neutral atoms, it is necessary to both isolate them from the environment and to achieve coherent control of the relevant internal and external degrees of freedom. Both of these steps involve the understanding and utilization of the light-atom interaction.

This chapter gives a theoretical background of light and atom interactions, required for the understanding of the principles of laser cooling and trapping. This treatment will be based on the classical Lorentz model which describes the interaction of a two-level atom with light in an intuitive way. Based on these results, the concepts of atom trapping in a far off-resonant light field by means of light induced dipole forces, will be extended to real world multilevel atoms.

Furthermore, a quantum mechanical model of the atomic eigenstates in the presence of far-detuned light fields will complete the theoretical part, which will allow us to estimate the effects of interrogation and manipulation of the atomic states in such a perturbed system.

2.1   Lorentz model

The interaction of a monochromatic light field and a neutral two-level atom is well described by a classical harmonic oscillator model (Lorentz model) [47]. In this model the atom is reduced to an electron (mass m_e, charge $-e$) bound to a massive core ($m_{\mathrm{core}} \gg m_{\mathrm{e}}$, with charge $+e$) by a harmonic potential. In the presence of a light field this electron is driven by the time varying electric field $\mathbf{E}(t) = \mathbf{e}E_0 e^{-i\omega t}$+c.c., with the polarization vector $\mathbf{e}$ and the amplitude E_0, leading to the equation of motion of a driven harmonic oscillator

$$\ddot{\mathbf{x}}(t) + \Gamma_\omega \dot{\mathbf{x}}(t) + \omega_0^2 \mathbf{x}(t) = -\frac{e}{m_e}\mathbf{E}(t), \tag{2.1}$$

where the damping is described by the energy dissipation rate due to classical dipole radiation [47]

$$\Gamma_\omega = \frac{e^2\omega^2}{6\pi\varepsilon_0 m_e c^3}, \tag{2.2}$$

and ω_0 is the resonance angular frequency of the oscillator. The stationary solution of Eq. (2.1)

$$\mathbf{x}(t) = -\frac{\alpha(\omega)}{e}\mathbf{E}(t), \tag{2.3}$$

yields an induced dipole moment of the atom $\mathbf{d}(t) = -e\mathbf{x}(t) = \alpha(\omega)\mathbf{E}(t)$, where

$$\alpha(\omega) = \frac{e^2}{m_e}\frac{1}{\omega_0^2 - \omega^2 - i\Gamma_\omega\omega}, \tag{2.4}$$

is the polarizability of the atom.

The polarizability $\alpha(\omega)$ is a complex function of the frequency, where the real and imaginary part describe the in-phase and the quadrature components of the atomic dipole moment $\mathbf{d}$, respectively.

By employing $e^2/m_e = 6\pi\varepsilon_0 c^3\Gamma_\omega/\omega^2$ and the damping rate on resonance $\Gamma \equiv \Gamma_{\omega_0} = (\omega_0/\omega)^2\Gamma_\omega$ the following relations for the phase and amplitude of the atomic response, describing the dispersion and absorption, can be obtained

$$\mathrm{Re}[\alpha(\omega)] = 6\pi\varepsilon_0 c^3\frac{(\omega_0^2 - \omega^2)\Gamma/\omega_0^2}{(\omega_0^2 - \omega^2)^2 + \Gamma^2(\omega^3/\omega_0^2)^2}, \tag{2.5}$$

$$\mathrm{Im}[\alpha(\omega)] = 6\pi\varepsilon_0 c^3\frac{\Gamma^2\omega^3/\omega_0^4}{(\omega_0^2 - \omega^2)^2 + \Gamma^2(\omega^3/\omega_0^2)^2}. \tag{2.6}$$
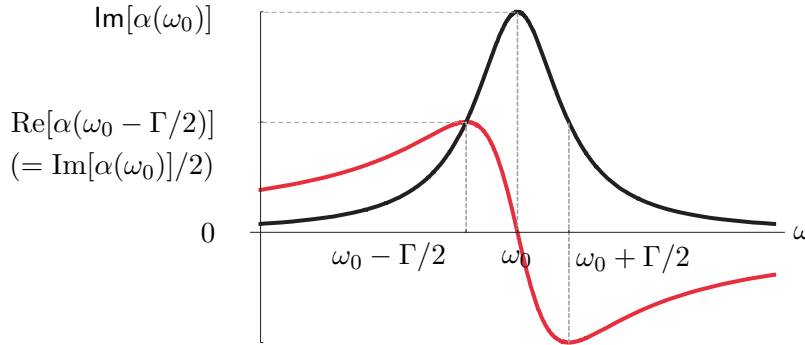

FIGURE 2.1: Real (red) and imaginary (black) parts of the polarizability $\alpha(\omega)$ as a function of the angular frequency ω in the classical Lorentz model.

2.1.1 Scattering rate

The time averaged power dissipation due to the damping rate Γ of a driven harmonic oscillator, described by

$$P = \left\langle \mathrm{Re}[\dot{\mathbf{d}}(t) \cdot \mathbf{E}(t)] \right\rangle = \frac{\omega |E_0|^2}{2} \mathrm{Im}[\alpha(\omega)], \qquad (2.7)$$

shows that the quadrature part of the atomic dipole moment describes the absorption of energy of the light field. In a classical model, energy is dissipated continuously, however in a quantum mechanical picture photons are emitted at the transition from an excited state $|e\rangle$ to the ground state $|g\rangle$ with a scattering rate

$$R_s = \frac{P}{\hbar\omega} = \frac{|E_0|^2}{2\hbar} \mathrm{Im}[\alpha(\omega)]. \qquad (2.8)$$

Note that furthermore the classical model applies only for low intensities of the driving field ($I = |E_0|^2/2c\epsilon_0$), where the polarizability does not depend on I. However, in the near resonant and high intensity regime the ground and excited state population of the atoms equilibrates, which leads to the saturation of the polarizability [5]

$$\mathrm{Im}[\alpha(\omega, I)] = \frac{6\pi\varepsilon_0 c^3}{\omega_0^3} \frac{1}{1 + I/I_0 + (2\Delta/\Gamma)^2}, \qquad (2.9)$$

$$\mathrm{Re}[\alpha(\omega, I)] = \frac{6\pi\varepsilon_0 c^3}{\omega_0^3} \frac{2\Delta/\Gamma}{1 + I/I_0 + (2\Delta/\Gamma)^2}, \qquad (2.10)$$

where $\Delta = \omega - \omega_0$, Γ is the decay rate of the excited state or the full width at half maximum (FWHM) of the transition line in units of rad/s, and

$$I_0 = \Gamma \frac{\pi\hbar\omega_0^3}{12\pi c^2} \qquad (2.11)$$

is the saturation intensity. Thus, the scattering rate becomes

$$R_s(I, \Delta) = \frac{\Gamma}{2} \frac{I}{I_0} \left[1 + \frac{I}{I_0} + \left(\frac{2\Delta}{\Gamma}\right)^2 \right]^{-1}. \qquad (2.12)$$

At resonance ($\Delta = 0$) and strong saturation ($I \gg I_0$), the scattering rate of single atoms can be substantial $\Gamma/2 \approx 10^7$ photons/s. However, even at moderate saturation in conjunction with strong transversal confinement of the probe light, scattering results in a significant absorption [43]. Hence, the resonant light-atom interaction can be very efficient for interrogation and manipulation of atomic states.

For detunings larger than $\Gamma/2$ the in-phase part of the atomic dipole moment becomes dominant (see Fig. 2.1), leading to a phase shift of the light with negligible absorption (see Sect. 4.3). At the same time, the back action of the induced dipole moment on the driving electric field results in dipole forces being exerted on the atoms.

2.1.2 Dipole potential

The time-averaged interaction potential of the induced dipole moment $\mathbf{d}$ and the (linearly polarized) driving electric field $\mathbf{E}$ is given by

$$U = -\frac{1}{2}\left\langle \mathbf{d}(t)\cdot\mathbf{E}(t)]\right\rangle = -\frac{1}{4}|E_0|^2\mathrm{Re}[\alpha(\omega)]. \tag{2.13}$$

Here, the first factor of $-\frac{1}{2}$ accounts for the induced dipole moment and another $\frac{1}{2}$ for the cycle average of squared electric field modulus.

For an atom (in the electronic ground state) subjected to a linearly polarized light field Eq. (2.13) describes the light-induced dipole potential, which in a spatially varying light field $\mathbf{E}(\mathbf{r},t)$ gives rise to dipole forces exerted on the atom $\mathbf{F} = -\nabla U(\mathbf{r})$. Considering the intensity of the field $I(\mathbf{r}) = |E_0(\mathbf{r})|^2/2c\epsilon_0$ and Eq. (2.5) the following expression for the optical dipole potential is obtained

$$U(\mathbf{r},\Delta) = -\frac{1}{2c\epsilon_0}I(\mathbf{r})\mathrm{Re}[\alpha(\Delta)]. \tag{2.14}$$

From the plot in Fig. 2.1 it is evident that for red detuning ($\Delta = \omega - \omega_0 < 0$) the potential $U(\mathbf{r})$ is attractive, i.e. the atom is attracted towards the intensity maximum of the light field. Conversely, for blue detuning ($\Delta = \omega - \omega_0 > 0$) the potential is repulsive, pushing the atom towards the intensity minimum. Strongly focused laser beams offer large intensity gradients ($\partial_i I(\mathbf{r})$), making optical trapping of dielectric particles (in, e.g., optical tweezers) with relatively low powers possible.

For large detunings of the trapping light, i.e., $|\omega_0 - \omega| \gg \Gamma$, the frequency dependent part of the dipole potential and of the scattering rate reduces to

$$U = -\frac{3\pi c^2 I\Gamma}{2\omega_0^3}\left(\frac{1}{\omega - \omega_0} + \frac{1}{\omega + \omega_0}\right) \tag{2.15}$$

$$R_s = \frac{3\pi c^2 I\Gamma^2}{2\hbar\omega_0^3}\frac{\omega^3}{\omega_0^3}\left(\frac{1}{\omega - \omega_0} + \frac{1}{\omega + \omega_0}\right)^2. \tag{2.16}$$

Using the rotating wave approximation and dropping fast oscillating terms, this leads to an expression for the rate of off-resonant scattering induced by the dipole fields

$$R_s = \frac{\Gamma}{\hbar\Delta}U. \tag{2.17}$$

By definition of the polarizability $\alpha(\omega)$ (Eq. (2.8)) the scattering of photons and the dipole force are interconnected and are strongest for near resonant light. However, photon scattering from the dipole trap lasers should be avoided since it leads to heating of the atoms and shortens the coherence and the lifetime of atomic states. In order to minimize the scattering rate (Eq. (2.17)) while maintaining strong dipole forces, far off resonant trapping laser fields ($|\Delta| \gg \Gamma$) with sufficiently high intensities have to be used.

2.1.3   Multilevel atoms

For large detunings of the trapping laser fields, the multilevel structure of real atoms and the multitude of transitions to various energy eigenstates have to be taken into account. Therefore, the application of the classical Lorentz model (Eq. (2.1)) encounters its limits. However, in a semiclassical picture, with a multilevel atom with n dipole-allowed transitions from the ground state to excited states, each transition can be approximated as an independent harmonic oscillator. The general solution can be constructed as a sum of the contribution of all individual oscillators weighted by the oscillator strength f_j of each transition, yielding

$$\alpha(\omega) = \sum_{j=1}^{n} f_j \alpha_j(\omega). \tag{2.18}$$

The oscillator strength can be calculated by modeling the atomic wave function or determined from the experimentally obtained data of transition line widths [49]. For the cesium D-lines, the latter method is more precise because the excited $6P$ states decay only to the $6S_{1/2}$ ground state. The relation between the linewidth (decay rate) Γ_j and the oscillator strength f_j reads

$$f_j = \Gamma_j \frac{2\pi\varepsilon_0 m_e c^3}{e^2 \omega_j^2} \frac{g_e}{g_g}, \tag{2.19}$$

where $\omega_j = (E_{e_j} - E_g)/\hbar$ denotes the transition frequency of the j-transition and $g_e/g_g = (2J'+1)/(2J+1)$ is the ratio between the degeneracies of the excited and ground states. Hence, the real and complex parts of the polarizability become

$$\mathrm{Re}[\alpha(\omega)] = 2\pi\varepsilon_0 c^3 \sum_j \frac{2J'+1}{2J+1} \frac{(\omega_j^2 - \omega^2)\Gamma_j/\omega_j^2}{(\omega_j^2 - \omega^2)^2 + \Gamma_j^2(\omega^3/\omega_j^2)^2}, \tag{2.20}$$

$$\mathrm{Im}[\alpha(\omega)] = 2\pi\varepsilon_0 c^3 \sum_j \frac{2J'+1}{2J+1} \frac{\Gamma_j^2\omega^3/\omega_j^4}{(\omega_j^2 - \omega^2)^2 + \Gamma_j^2(\omega^3/\omega_j^2)^2}. \tag{2.21}$$

The resulting scattering rate as well as the dipole potential of a cesium atom in the ground state can now be obtained analogously to Eqns. (2.8) and (2.14). Note that the calculation of potentials of excited states requires a full quantum mechanical description of the light-matter interaction (see next section).
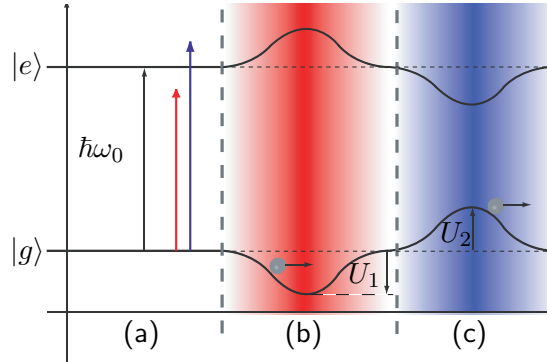
FIGURE 2.2:   AC-Stark shift of a two-level atom in a red-detuned and blue-detuned laser beam, respectively. (a) Unperturbed level diagram of the ground state $|g\rangle$ and excited state $|e\rangle$. The red and blue arrows indicate the respective detuning. (b) Shift of the ground and excited state in the presence of red-detuned light. Dark regions indicate high intensities. Note that an excited atom is repelled from the trap region. (c) For blue detuning the shifts are inverted.

2.2   AC-Stark shift

One of the main motivations of laser cooling and trapping is the storage of atoms over times sufficiently long enough to efficiently store and retrieve quantum information (qubits) encoded in the atomic states using (near) resonant light. Due to the weak coupling of neutral atoms to their environment, coherent manipulation of atomic states can be robust against external perturbations [5]. Therefore, the feasibility of storing atoms, almost without loss of the atomic coherence, makes optically trapped neutral atoms prime candidates for the implementation of quantum memories and quantum repeaters in the context of quantum information processing and transmission [23,27]. For this purpose, far off-resonant detuned lasers are used which ensure low scattering rates and thus provide a long coherence time. However, the interaction of the trapping light field inherently perturbs the atomic states and can influence the interaction with resonant light.

The presence of an intense red-detuned light field lowers the ground state energy of the atom (see Fig. 2.2). The lowest potential energy of the atom, i.e., the location where the atom can be trapped, is associated with the largest negative shift, and is found at the local intensity maximum. In general, the light shift of the excited state is different from that of the ground state. Thus, in strongly confining traps the differential light shift (ac-Stark shift), of the connected pair of states leads to a strong position dependent shift accompanied with inhomogeneous broadening of the atomic transition. Moreover, for resonantly driven atoms the trapping potential can be even repulsive while the atom is excited, leading to dipole force fluctuation and heating.

For blue-detuned light the ac-Stark shift leads to an increase of the atomic potential energy which, for special beam geometries (e.g., hollow beams, optical lattices etc.), enables trapping of atoms in the region of minimum intensity [40,58]. In this case, the differential light shift can be locally minimized. However, due to diffraction of such strongly confined laser beams the potential minimum is never completely field free. Thus, confinement in blue-detuned traps is less efficient and more prone to inhomogeneous broadening.

The straightforward approach to avoid the perturbation of the trapping fields is to switch off the trapping light and to perform the measurement on the free-falling atoms [29]. However, a drawback of this method is the limited time-of-flight and the short recapture range of optical traps. Another approach employs so-called magic wavelengths in red-detuned traps in order to eliminate the differential ac-Stark shift [60,61]. The principle idea is based on a clever choice of the wavelength of the trapping light for which an atom experiences shifts of equal sign and magnitude of the excited state and of the ground state.

In Ref. [65] it has been shown theoretically that the differential light shifts for cesium atoms, subjected to the combined red-detuned and blue-detuned trapping fields in a nanofiber trap, can be eliminated analogously.

However, the theoretical approach to the description of the ac-Stark shift in a nanofiber trap is incomplete. The model in Ref. [65] is based on the formalism derived for the static Stark shift in [66], which separates the interaction into a monopolar (scalar) and a quadrupolar (rank 2 tensor) symmetry, whereas the dipolar (axial vector) part is neglected. Meaning that, the extension of this model to the case of a dynamic interaction is only valid for linearly polarized light fields. Since the polarization of the evanescent field of a strongly guided mode HE_{11} varies in space and time [32,34], the treatment of the ac-Stark shift in the nanofiber trap thus requires a more general model. An appropriate description of the ac-Stark shifts induced by arbitrary polarized light fields can be found in Ref. [62] and [67] and is closely followed here.

In this work we analyze a generalized model describing the ac-Stark shift in optically-trapped cesium atoms. This allows us to find the perturbed eigenenergies and eigenstates in the presence of both trapping light fields in a nanofiber trap.

Based on these results, we estimate the influence of the ac-Stark effect on the transition amplitude between the ground and excited states in order to determine the coupling efficiency as well as the absorption spectra of the trapped atoms interacting with a resonant probe light. We show that for certain cases the trapped atoms exhibit shifts of the energy levels with a negligible mixing of the atomic states.

Furthermore, we demonstrate that the experimentally obtained absorption spectra for trapped cesium atoms are in good agreement with the numerical calculation of the light shifts.

Theory

The general quantum mechanical description of atoms subjected to a monochromatic laser field makes use of the "dressed states" approach [63], in which both the atomic states as well as the light field are quantized. For light waves that can be described by a single radiation mode with large photon numbers, the field equations take the equivalent form as for a classical electromagnetic wave.

In this work we will thus consider the interaction of an atom and a classical optical field

$$\boldsymbol{\mathcal{E}}(\mathbf{r}, t) = \frac{1}{2}\mathcal{E}\mathbf{e}e^{-i\omega t + i\mathbf{k}\cdot\mathbf{r}} + \text{c.c.}, \tag{2.22}$$

where c.c. designates the complex conjugate of the preceding term, $\mathcal{E}$ denotes the electric field amplitude, ω is the angular light frequency, $\mathbf{k}$ is the wave vector, and $\mathbf{e}$ is the complex polarization vector. In the dipole approximation the coupling term of the Hamiltonian in the interaction picture reads

$$\begin{aligned} V_E \equiv -\boldsymbol{\mathcal{E}} \cdot \mathbf{d} &= -\frac{1}{2}\mathcal{E}\mathbf{e} \cdot \mathbf{d}e^{-i\omega t} + \text{H.c.} \\ &= V_-e^{-i\omega t} + V_+e^{i\omega t}, \end{aligned} \tag{2.23}$$

where

$$\mathbf{d} = \sum_i^N e\mathbf{r}_i \tag{2.24}$$

is the electric dipole moment operator and $\mathbf{r}_i$ represents the position vector of the ith electron and H.c. represents the Hermitian conjugate. The total Hamiltonian of the system "atom + field" is thus given by

$$\begin{aligned} H &= H_0 + V_E \\ &= (H_{\text{elect.}} + V_{\text{hfi}}) + V_-e^{-i\omega t} + V_+e^{i\omega t}, \end{aligned} \tag{2.25}$$

where $H_0 = H_{\text{elect.}} + V_{\text{hfi}}$ denotes the atomic Hamiltonian accounting for the electronic and hyperfine structure.

For atoms with a finite nuclear and electronic angular momentum $\mathbf{I}$ and $\mathbf{J}$, respectively, the $\mathbf{I}\cdot\mathbf{J}$ coupling leads to the energy eigenstates represented by the hyperfine states (hfs) $|\Psi\rangle = |n, F, M_F\rangle$, which are angular momentum eigenstates of the operator $\mathbf{F} = \mathbf{J} + \mathbf{I}$. Here, the quantum number F is referred to the total angular momentum, M_F is the projection of F onto the quantization axis, and n denotes all remaining quantum numbers $\{n(ls)JI\}$ characterizing the (fine) structure of the atoms. Compared to the level splitting arising due to the hyperfine interaction (V_{hfi}), the effect of the ac-Stark shift is assumed to be small. Hence, we may treat the energy correction of the atomic states in the presence of a weak variable electromagnetic field in terms of time-dependent perturbation theory.

For periodically varying fields, this treatment gets even simpler if we apply Floquet's theorem [62, 64]. By employing the basis of *quasienergy* states of the system composed of an atom and a field, we can use the result for the Stark shift in a static electric field

$$\Delta E_0 = \sum_{i \neq 0} \frac{|\langle \Psi_0 \,|\, \mathcal{E}\mathbf{e} \cdot \mathbf{d} \,|\, \Psi_i \rangle|^2}{E_0 - E_i}, \tag{2.26}$$

however, instead of using the unperturbed energies E_i of the intermediate states of the atom we have to employ the energies $E_i + \hbar\omega$ and $E_i - \hbar\omega$ of the complete system. These two energies are referred to the absorption and emission of a single photon in the transition from the initial state $|\Psi_0\rangle = |n, F, M_F\rangle$ to an intermediate state $|\Psi_i\rangle = |n'', F'', M_F''\rangle$ over which the summation in Eq. (2.26) is performed. Note that higher orders of the perturbation theory correspond to the absorption and the emission of a larger number of photons.

Hence, by applying time-independent second-order perturbation theory with an effective electric field amplitude (depending on the polarization of the field (cf. Eq. (2.22)), the following expression for the energy correction (ac-Stark shift) of the atomic state $|\Psi_0\rangle$ is obtained

$$
\begin{aligned}
\Delta E_{\mathrm{ac}} = {} & \frac{1}{4}\mathcal{E}^2 \sum_i \frac{\langle \Psi_0 \,|\, \mathbf{e}^* \cdot \mathbf{d} \,|\, \Psi_i \rangle \langle \Psi_i \,|\, \mathbf{e} \cdot \mathbf{d} \,|\, \Psi_0 \rangle}{E_0 - E_i + \hbar\omega} \\
& + \frac{1}{4}\mathcal{E}^2 \sum_i \frac{\langle \Psi_0 \,|\, \mathbf{e} \cdot \mathbf{d} \,|\, \Psi_i \rangle \langle \Psi_i \,|\, \mathbf{e}^* \cdot \mathbf{d} \,|\, \Psi_0 \rangle}{E_0 - E_i - \hbar\omega},
\end{aligned} \tag{2.27}
$$

where we sum over the non-degenerate sub-space and make use of the abbreviation $i = \{n'', J'', F'', M_F''\}$.

By introducing the operator

$$V_{EE}(\boldsymbol{\mathcal{E}}, \omega) = \frac{1}{4}\mathcal{E}^2 \{(\mathbf{e}^* \cdot \mathbf{d}) R_{E_0}(\omega)(\mathbf{e} \cdot \mathbf{d}) + (\mathbf{e} \cdot \mathbf{d}) R_{E_0}(-\omega)(\mathbf{e}^* \cdot \mathbf{d})\}, \tag{2.28}$$

with

$$R_{E_0}(\pm\omega) = (E_0 - \hat{H}_0 \pm \hbar\omega)^{-1} = \sum_i \frac{|\Psi_i\rangle \langle \Psi_i|}{E_0 - E_i \pm \hbar\omega}, \tag{2.29}$$

being the resolvent operator ($\hat{H}_0$ is the unperturbed atomic Hamiltonian), the energy shift in Eq. (2.27) can be recast as an expectation value

$$\Delta E_{\mathrm{ac}} = \langle \Psi_0 | V_{EE}(\boldsymbol{\mathcal{E}}, \omega) | \Psi_0 \rangle, \tag{2.30}$$

while the contributions due to mixing of states are accounted by the off-diagonal matrix elements $\langle \Psi_0 | V_{EE}(\boldsymbol{\mathcal{E}}, \omega) | \Psi_0' \rangle$.

In general $V_{EE}(\boldsymbol{\mathcal{E}}, \omega)$ is not diagonal in the hfs basis, thus in order to find the new eigenstates and eigenenergies one has to diagonalize the atomic Hamiltonian including the ac-Stark interaction. However, we assume relatively small light shifts in a dipole trap compared to the large hyperfine splitting of the relevant $|n, F, M\rangle$ states ($\Delta E_{\text{hfi}} > 150$ MHz for the $6P_{3/2}$ states).

Under the assumptions of small light shifts V_{EE} can be regarded as diagonal in $|n, F\rangle$. In this case, only the matrix elements between the states $|n, F, M\rangle$ and $|n, F, M'\rangle$ need to be considered for the further calculation (i.e., replace F' with F in the following calculations).

Furthermore, the order of the operators in Eq. (2.28) may be changed and rewritten in a spherical tensor form [67]

$$V_{EE}(\boldsymbol{\mathcal{E}}, \omega) = \frac{1}{4}\mathcal{E}^2 \sum_{K=0,1,2} \{\mathbf{e}^* \otimes \mathbf{e}\}_K \cdot \Big[\{\mathbf{d} \otimes R_{E_0}(\omega)\mathbf{d}\}_K + (-1)^K \{\mathbf{d} \otimes R_{E_0}(-\omega)\mathbf{d}\}_K\Big],$$
(2.31)

leading to a decomposition of V_{EE} into a scalar ($K = 0$), vector ($K = 1$), and tensor ($K = 2$) part.

In the following we will abbreviate the notation for the matrix elements of V_{EE} by

$$T_{M,M'} = \langle n, F, M_F | V_{EE}(\boldsymbol{\mathcal{E}}, \omega) | n, F', M'_F \rangle.$$
(2.32)

By employing the Wigner-Eckart theorem we find an explicit expression for each matrix element

$$\begin{aligned}
T_{M,M'} &= \frac{1}{4}\mathcal{E}^2 \sum_{\substack{K=0,1,2 \\ \mu=-K\ldots K}} \{\mathbf{e} \otimes \mathbf{e}^*\}_{K,\mu} C^{F',M'}_{F,M,K,\mu} \alpha^{(K)}_{nF}(\omega) \\
&= \frac{1}{4}\mathcal{E}^2 \sum_{\substack{K=0,1,2 \\ \mu=-K\ldots K}} (-1)^{K+\mu}\{\mathbf{e}^* \otimes \mathbf{e}\}_{K,-\mu}(-1)^{F-M_F} \begin{pmatrix} F & K & F' \\ -M & \mu & M' \end{pmatrix} \alpha^{(K)}_{nF}(\omega),
\end{aligned}$$
(2.33)

where $\alpha^{(K)}_{nF}(\omega)$ is the reduced atomic polarizability

$$\alpha^{(K)}_{nF}(\omega) = \langle n, F \, \| \, \{\mathbf{d} \otimes R_{E_0}(\omega)\mathbf{d}\}_K + (-1)^K \{\mathbf{d} \otimes R_{E_0}(-\omega)\mathbf{d}\}_K \, \| \, n, F' \rangle. \quad (2.34)$$

The expression for $\alpha^{(K)}_{nF}$ can be conveniently recast and evaluated via

$$\begin{aligned}
\alpha^{(K)}_{nF}(\omega) = (-1)^{I-J+F}\sqrt{2K+1}\sqrt{2F+1}\sqrt{2F'+1} \begin{Bmatrix} F & K & F' \\ J & I & J \end{Bmatrix} \\
\times \sum_{n''J''} \begin{Bmatrix} J & K & J \\ 1 & J'' & 1 \end{Bmatrix} \langle nJ \| \mathbf{d} \| n''J'' \rangle \langle n''J'' \| \mathbf{d} \| nJ \rangle \\
\times \left[\frac{1}{E_{n,J} - E_{n'',J''} + \hbar\omega} + \frac{(-1)^K}{E_{n,J} - E_{n'',J''} - \hbar\omega}\right],
\end{aligned}$$
(2.35)

where the reduced electric dipole matrix elements $\langle nJ\|\mathbf{d}\|n''J''\rangle$ can be obtained via the oscillator strengths $f_{nJ,n''J''}$ for the $|nJ\rangle \leftrightarrow |n''J''\rangle$ transitions (cf. [50])

$$f_{nJ,n''J''} = \frac{2m_e}{3\hbar^2 e^2}\frac{E_{nJ}-E_{n''J''}}{2J+1}|\langle nJ\|\mathbf{d}\|n'',J''\rangle|^2. \qquad (2.36)$$

Here, we employed the notations $C^{J,M}_{j_1,m_1,j_2,m_2}$ for Clebsch-Gordan (CG) coefficients, and $\begin{pmatrix} j_1 & j_2 & J \\ m_1 & m_2 & M \end{pmatrix}$, $\begin{Bmatrix} j_1 & j_2 & j_3 \\ j_4 & j_5 & j_6 \end{Bmatrix}$ for the Wigner 3-j and 6-j symbols, respectively.

The compound tensor $\{\mathbf{e} \otimes \mathbf{e}^*\}_{K,\mu} = \sum_{i,j} C^{K,\mu}_{1,i,1,j}\mathbf{e}_i(\mathbf{e}^*)_j$ accounts for the spatial orientation and polarization of the light field. The parametrization of the polarization in Cartesian coordinates by the angle θ,

$$\mathbf{e} = e_x \sin\theta + ie_y \cos\theta, \qquad (2.37)$$

which is related to the degree of linear polarization $l = \cos 2\theta$, and to the ellipticity $A = \sin 2\theta$, reduces the tensor $\{\mathbf{e} \otimes \mathbf{e}^*\}_{K,\mu}$ to

$$\{\mathbf{e}^* \otimes \mathbf{e}\}_{0,0} = -\frac{1}{\sqrt{3}}(\mathbf{e}^* \cdot \mathbf{e}) = -\frac{1}{\sqrt{3}}$$

$$\{\mathbf{e}^* \otimes \mathbf{e}\}_{1,\mu} = -\frac{1}{\sqrt{2}}(\mathbf{e}^* \times \mathbf{e})_\mu = -\frac{A}{\sqrt{2}}\delta_{\mu,0}$$

$$\{\mathbf{e}^* \otimes \mathbf{e}\}_{2,\mu} = -\frac{1}{\sqrt{6}}\delta_{\mu,0} + \frac{l}{\sqrt{2}}\delta_{\mu,\pm 2}. \qquad (2.38)$$

Note that the quantization axis (z-axis) is chosen as the propagation direction of the light.

The 3-j symbol in Eq. (2.33) indicates the coupling of the hfs states with different M_F quantum numbers through the ac-Stark interaction and makes the operator V_{EE} in general non-diagonal in this sub-space. Nevertheless, for linearly and circularly polarized light, the correct choice of the quantization axis makes $T_{M,M'}$ diagonal.

If the field is oriented in such a way that an axis of rotational symmetry of the system exists, i.e., z-axis along propagation direction for circular polarization, and z-axis along the electric field $\mathcal{E}$ for linear polarization, M_F is a constant of motion. Thus, the off-diagonal elements of $T_{M,M'}$ vanish and $|F, M_F\rangle$ become also eigenstates of the Stark operator.

In the case of linear polarization, we find similar expressions for the diagonal energy correction as for the case of static electric fields, involving a scalar (α^s_{nF}) and a tensor (α^T_{nF}) term [66]

$$\Delta E_{\rm ac} = T_{M,M} = -\frac{1}{4}\mathcal{E}^2\left[\alpha^s_{nF}(\omega) - \alpha^T_{nF}(\omega)\frac{3M_F^2 - F(F+1)}{2F(2F-1)}\right]. \qquad (2.39)$$

For the case of circular polarization (i.e., $A = \pm 1$), the additional vector term $(\alpha_{nF}^a M_F)$ shifts the energy levels in analogy to the Zeeman shift, yielding following expression for the ac-Stark shift

$$\Delta E_{\text{ac}} = T_{M,M} = -\frac{1}{4}\mathcal{E}^2 \left[\alpha_{nF}^s(\omega) + A\alpha_{nF}^a(\omega)\frac{M_F}{2F} - \alpha_{nF}^T(\omega)\frac{3M_F^2 - F(F+1)}{2F(2F-1)} \right],$$
(2.40)

with

$$\alpha_{nF}^s = \frac{1}{\sqrt{3(2F+1)}}\alpha_{nF}^{(0)},$$

$$\alpha_{nF}^a = -\sqrt{\frac{2F}{(F+1)(2F+1)}}\alpha_{nF}^{(1)},$$

$$\alpha_{nF}^T = -\sqrt{\frac{2F(2F-1)}{3(F+1)(2F+1)(2F+3)}}\alpha_{nF}^{(2)}.$$
(2.41)

The expression for the ac-Stark shift (Eq. (2.40)) holds only if F and M_F are good quantum numbers, which in practise can be assured by applying a quantizing magnetic field along the propagation direction of the light.

For the general case of elliptical polarization (i.e., $|A| < 1$), M_F is not a constant of motion. Thus, the off-diagonal elements of the following form have to be taken into account

$$T_{M,M\pm 2} = \frac{3\mathcal{E}^2}{16}l\alpha_{nF}^T(\omega)\frac{[(F\pm M+1)(F\pm M+2)(F\mp M)(F\mp M-1)]^{1/2}}{F(2F-1)}.$$
(2.42)

With the final form of the reduced polarizabilities (Eq. (2.35)), it can be easily proven that for $J = 0, 1/2$ states (as the ground states of alkali-atoms such as Cs and Rb with $J = 1/2$), the tensor polarizability $\alpha_{nF}^{(2)}$ vanishes, and for linearly polarized light the ac-Stark shift is only determined by the scalar component in Eq. (2.39), which is independent of the orientation of the quantization axis and of the M_F quantum number. The explanation for this behavior is based on a symmetry argument, i.e., the fact that the quadratic Stark shift for electrons with an angular momentum of $J_z = 0, \pm 1/2$ is independent of the spatial orientation of the field. Hence, the corresponding hfs $|F, F_z\rangle$ which are linear superpositions of these electronic states times nuclear states are all shifted equally.

For states with $J > 1/2$, however, the orientation of the electric field with respect to the quantization axis is of relevance to the tensor shift. This leads to optical coupling between $M_F' = M_F \pm 2$ states and lifts the degeneracy of the new eigenstates.

2.3 Light shifts and potentials in a two-color dipole trap

In the following we consider the energy shifts, i.e., potentials of the ground and excited states of cesium with $J = 1/2$ and $J = 3/2$ respectively, subjected to two light fields of different wavelengths and different polarizations. This analysis is devoted to the estimation of the light shifts of the $|6S_{1/2}\rangle$ and $|6P_{3/2}\rangle$ states in order to examine the perturbation of the D2-transition of optically trapped cesium atoms in a two-color evanescent light field around a nanofiber.

For this dipole trap, the intense evanescent fields around the nanofiber lower the ground state energy of the atoms in the vicinity of the fiber surface, and thus induce the dipole trapping potential. The red-detuned light field as well as the van der Waals force attracts the atoms towards the nanofiber while the blue-detuned light field forms a repulsive potential and repels the atoms from the fiber surface [15,31]. Due to the different radial decay lengths of the far red- and blue-detuned evanescent fields of the fundamental HE_{11} mode one can thus create a radial potential minimum at a few hundred nanometers from the nanofiber surface by properly choosing the respective powers (see Fig. 2.3 (a)).

Confinement along the fiber axis is achieved by launching an additional, counter-propagating red-detuned laser beam through the fiber, thereby realizing a red-detuned standing wave, see Fig. 2.3 (b), whereas the blue-detuned running wave leads to a translation invariant repulsive field along the nanofiber. Azimuthal confinement of the atoms stems from the azimuthal dependence of the evanescent field intensity of the quasi-linearly polarized HE_{11} mode (see Fig. 2.3 (c)). In order to maximize the azimuthal confinement we use orthogonal linear polarizations, i.e., the azimuthal intensity maximum of the red-detuned field coincides with the azimuthal intensity minimum of the blue detuned field.

Figure 2.3 (d) shows the two resulting 1d arrays of trapping minima on both sides of the fiber, visualized by the equipotential surfaces 40 μK and 125 μK above the trapping minimum.

In this configuration, the potential minima can be found at the anti-nodes of the red-detuned standing wave in the plane of maximum intensity which is parallel to the polarization direction of the red-detuned light field. At these points, the blue-detuned field is polarized tangential to the fiber surface, making both trapping fields purely linearly polarized in the vicinity of the trapping minimum [31]: The (longitudinal) z-components of the red-detuned evanescent fields interfere destructively at the anti-nodes due to their phase shift of $\pi/2$ with respect to the transverse components (see Sect. 1.1). In addition, the z-component of the blue-detuned field vanishes because its polarization vector is oriented parallel to the fiber surface (see Sect. 1.3.2).
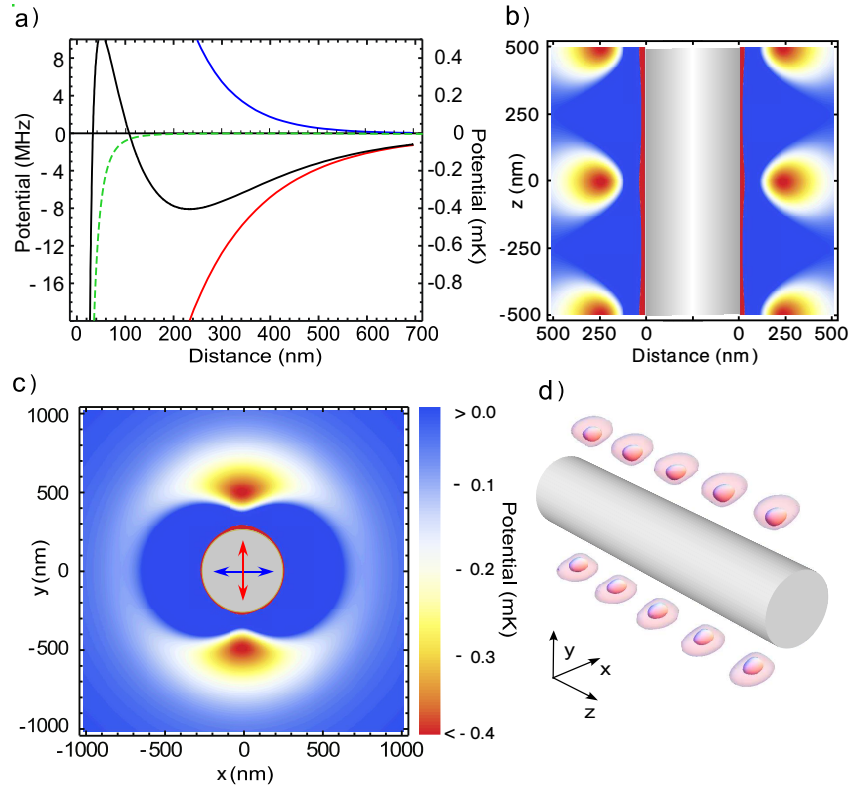
FIGURE 2.3: (a, black line) Light-induced potential plus the van der Waals potential as a function of distance from the surface of a 500-nm diameter nanofiber for a ground state cesium atom ($S_{1/2}$) formed by a red-detuned (wavelength 1064 nm, red line) and blue-detuned (wavelength 780 nm, blue line) two-color evanescent light field. We assumed a power of $P_{\mathrm{red}} = 2 \times 2.2$ mW (standing wave) and $P_{\mathrm{blue}} = 25$ mW and orthogonal linear polarization of the red-detuned and blue-detuned fields, indicated by the arrows in Fig.(c). The green dashed line indicates the v.d.W potential solely. (b) Contour plots of the same potential as in (a). The red-detuned standing wave ensures axial confinement. (c) Azimuthal plot of the same potential as in (a) and (b). The planes of the plots in (a)–(c) are chosen such that they include the trapping minima in all three cases. (d) Contour plot of the resulting array of trapping sites on both sides of the fiber showing equipotential surfaces 40 μK and the 125 μK above the trapping minimum.

The ground state potential for cesium atoms, induced by the linearly polarized evanescent fields in the mentioned configuration, as a function of cylindrical coordinates (r, ϕ, z) reads

$$U(r, \phi, z) = -\frac{1}{4} \left(4\alpha_g^s(\omega_{\mathrm{red}})\mathcal{E}_{\mathrm{red}}^2(r, \phi) \cos^2\left(\beta_{\mathrm{red}}z\right) + \alpha_g^s(\omega_{\mathrm{blue}})\mathcal{E}_{\mathrm{blue}}^2(r, \phi + \pi/2) \right),$$
(2.43)

where the radial and azimuthal dependency of the respective electric fields $\mathcal{E}(r, \phi)$ is given by Eq. (1.52) in Sect. 1.3.2, $\beta_{\mathrm{red}} = n_{\mathrm{eff}} k_{\mathrm{red}}$ is the propagation constant of $\mathcal{E}_{\mathrm{red}}$ and thus the lattice constant of the standing wave potential, n_{eff} is the effective refractive index, k_{red} is the wave number of the red-detuned light field [34], and $\alpha_g^s(\omega)$ is the scalar polarizability of the ground state. Note that admixtures of circularly polarized light lift the degeneracy of the Zeeman sub-states, i.e., the ground state potential becomes M_F dependent. Nevertheless, at the vicinity of the trap center, where the polarizations of the fields are essentially linear, equation (2.43) remains valid. The strongest deviation from linear polarization for the red-detuned field can be found for small displacements in the axial direction. The estimated thermal motion of atoms in our trap results only in a displacement of about 12 nm from the trap center (see Sect. 3.4) where the ellipticity is negligibly small (i.e., $A \approx 0.002$).

We also note that the contribution of the v.d.W. potential to the trapping potential at radial distances beyond 100 nm from the fiber surface can be completely neglected (see Fig. 2.3 (a)).

Numerical evaluation

For the calculation of the light-shifts of the ground and excited state manifold of cesium $|6S_{1/2}, F = 4, M\rangle$, and $|6P_{3/2}, F = 5, M\rangle$ respectively, we applied the formalism discussed in the previous section. We diagonalized the Hamiltonian of this system which includes the the Stark interaction of each light field. For the calculation of the ac-Stark shifts of the $|6P_{3/2}, F = 5\rangle$ manifold, we considered the dipole allowed coupling to the states listed in Fig. 2.4. The corresponding polarizabilities have been derived from Eq. 2.35 and the oscillator strengths given by [50].

Figures 2.3(a) and 2.5 show the resulting energy shifts of the respective states of atomic cesium in the vicinity of a 500-nm diameter fiber. Here, we assumed the powers and wavelengths (780 nm with 25 mW, and 1064 nm with 2×2.2 mW) that are used in the experimental part of this work. These numerical results have been obtained from the eigenvalues of the summed tensors of both fields, i.e., the solutions of the eigenvalue problem $\det \|T_{M,M'}^{\mathrm{blue}} + T_{M,M'}^{\mathrm{red}} - \Delta E_{\mathrm{ac}}\delta_{M,M'}\| = 0$ in Eq. (2.33) and Eq. (2.43) evaluated using Mathematica.

The resulting light-shift of the ground state at the trap center ($r = 230$ nm, $\phi = 0$, $z = 0$) yields -8 MHz and the shift and splitting of the excited state manifold (see Fig. 2.6) yield -11 to $+9$ MHz at the trapping minimum, depending on the new $|F', m'\rangle$ sub-state.
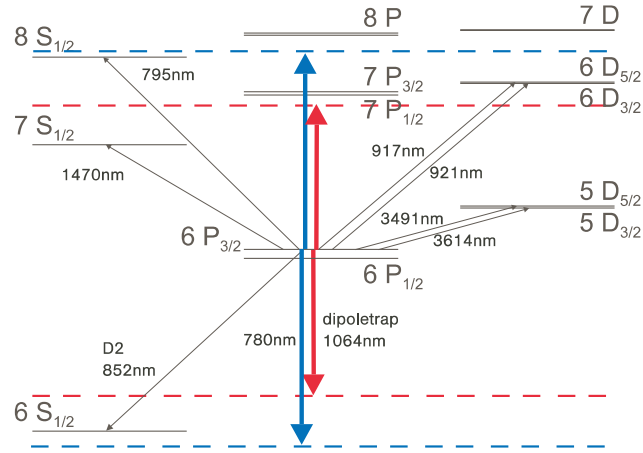
FIGURE 2.4:   Level diagram and transition wavelengths of atomic cesium. The $6P_{3/2}$ state couples additionally to the ground state also to a multitude of energetically higher lying states, which have to be taken into account for the calculation of its light shift.
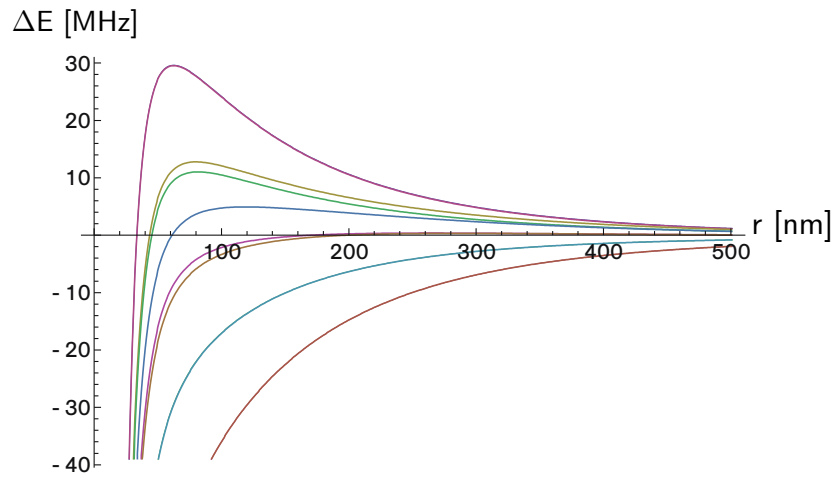
FIGURE 2.5:   Optical potentials for the $|6P_{3/2}, F = 5, M\rangle$ sub-state manifold including the v.d.W. potential as a function of the radial distance from the fiber surface. Note that the degeneracy is lifted by the presence of two mutually orthogonally polarized light fields.

FIGURE 2.6:   AC-Stark shift of the $|6S_{1/2}, F = 4\rangle$ ground state and the $|6P_{3/2}, F = 5\rangle$ excited state manifold of atomic cesium at the trap center, located 230 nm above the surface of the fiber. The quantization axis is aligned along the polarization direction of the leading field in the trap ($\mathcal{E}_{\text{red}}$). The red squares indicate the light shifts predicted by the reduced model, i.e., when neglecting the off-diagonal coupling (see text).
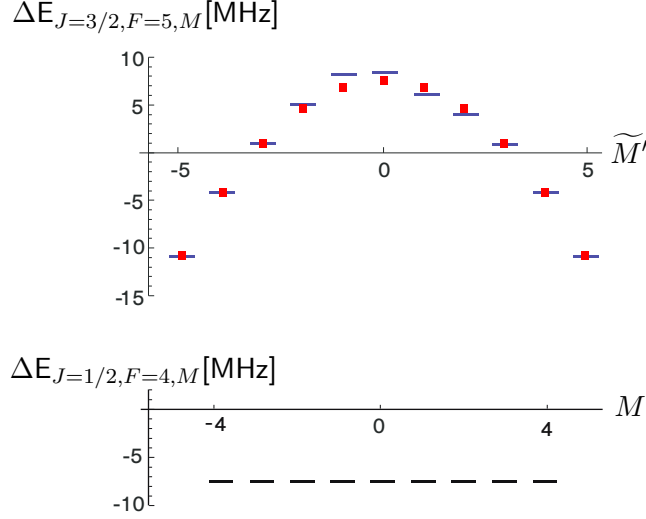
Results and Discussion

From the definition of the reduced polarizability in Eq. (2.35) and symmetry arguments, it can be shown that for linearly polarized light the $J = 1/2$ ground state exhibits only a non-vanishing scalar contribution (α_g^s) to the ac-Stark shift, which maintains the $|n, J = 1/2, F, M_F\rangle$ states as eigenstates including the degeneracy of the M_F sub-levels. Note that elliptically polarized light, as well as a non-vanishing (longitudinal) $\mathcal{E}_z$-component of the HE$_{11}$ mode, introduce a "fictitious magnetic field" due to the vector polarizability (cf. Eq. (2.33)). This breaks the degeneracy through a Zeeman-like shift and creates coherences among the M_F sub-states. However, the field configuration in our setup features essentially linear polarizations at the trapping minima. Hence, the electric dipole transitions between $J = 1/2 \leftrightarrow J' = 1/2$ states (e.g., D1-line $|6S_{1/2}\rangle \leftrightarrow |6P_{1/2}\rangle$) are expected not to be significantly influenced by the presence of two linearly polarized trapping fields.

In contrast to the $J = 1/2$ states, the non-vanishing tensor component (α_e^T) makes the potential of the $J = 3/2$ excited states in a optical dipole trap strongly dependent on the F and M_F quantum numbers including a change in sign (see Fig. 2.5). For a single linearly polarized light field (polarized along quantization axis), the ac-Stark shift scales quadratically in M_F (cf. Eq. (2.40)), leaving a two-fold de-

generacy corresponding to the pairs of M_F numbers with the same magnitude (but opposite sign).

However, the presence of a second orthogonally polarized light field breaks the rotational symmetry of the system, such that no orientation of the quantization axis can be found for which the excited states $|J = 3/2, F, M_F\rangle$ are eigenstates. In this case the non-vanishing off-diagonal coupling ($T_{M,M\pm2} \neq 0$ in Eq. 2.33) gives rise to mixing between the degenerate $|M_F\rangle$ sub-states. The new energy eigenstates thus become superpositions of these sub-states

$$|n, F, m\rangle = \sum_{M_F} c_{M_F,m'} |n, F, M_F\rangle \,, \tag{2.44}$$

where the mixing coefficients $c_{M_F,m}$ of the eigenstates in the $|M_F\rangle$ basis can be obtained by diagonalization of the Hamiltonian in the presence of both light fields in Eq. (2.33). The mixing of the excited states may result in simultaneous coupling to various hyperfine states via the $J = 1/2 \leftrightarrow J' = 3/2$ transitions, which may influence the resonant atom-light interaction in our system in addition to inhomogenous broadening.

Nevertheless, for M_F states defined with respect to the quantization axis chosen along the polarization vector of the dominating field (red-detuned field) the effect of hfs mixing can be neglected. For the trap parameters considered in the experimental part, we find only a small deviation of the ac-Stark shift of the $|6P_{3/2}, F = 5, M_F\rangle$ states of at most 1 MHz out of 9 MHz less shift for the low M_F numbers (and 0.03 MHz deviations for $M_F = \pm F$ states) when neglecting the off-diagonal matrix elements of the Stark operator ($T_{M,M\pm2} \to 0$) (see Fig. 2.6).

In addition, a weak bias magnetic field applied parallel to the red-detuned field could be used in order to insure that M_F is still a good quantum number. Provided that the off-diagonal coupling of the ac-Stark interaction induced by blue-detuned field is weaker than the splitting of the Zeeman levels, mixing of the M_F states can be completely neglected [67].

For a better understanding of the experimental results regarding the shifts and broadening of the absorption spectra of trapped cesium atoms under the influence of the two-color dipole fields we applied the formalism discussed above. The experimentally observed spectra for the D2 transitions in a trapped atomic ensemble with evenly populated M_F states are in good agreement with the theoretical predictions of the ac-Stark effect even when assuming negligible mixing of hfs (see Sect. 4.1).

Chapter 3

Trapping of neutral atoms

Introduction

In view of the excellent coherence properties of neutral atoms, which are essential for many applications in quantum optics and quantum information technology, they are one of the most promising candidates as carrier and storage units of quantum information [6].

However, in general the control of neutral atoms is technically challenging, due to the relatively weak interaction of the induced electric dipoles with electromagnetic fields. For this reason alkali atoms, i.e., sodium, rubidium, cesium, etc. are predominantly employed, because of their strong interfacing to light via the D-transitions. These strong electric dipole transitions provide almost perfectly closed sub-transitions and are accessible with tunable lasers, making alkali atoms suitable for laser cooling and for optical trapping (see Sect. 3.1).

Light-induced dipole forces act in general on any polarizable particle in a strong gradient electro-magnetic field and have been proposed for trapping of particles since the first realization of a laser in the 1960s [70, 71]. The first applications of these forces have been found in, e.g., biology as optical tweezers. However, light induced dipole forces exerted on neutral atoms are very weak, thus only very cold atoms can be considered for optical trapping. In this context, T. Hänsch, A. Schawlow [72], D. Wineland and H. Dehmelt [73] independently proposed already in 1975 the cooling of atomic gases with near resonant laser light.

The first three-dimensional laser-cooling scheme for atoms was realized by S. Chu [75] in 1985, permitting the first experimental demonstration of optical trapping of neutral atoms [76]. The development of laser-cooling in combination with the magneto-optical trap (MOT) [77] led to the utilization of dipole traps for atoms in many varieties. Among focused laser beams, evanescent waves on prisms [78–80] or

planar wave guides [84] have been readily applied, from trapping of ensembles of neutral atoms to forming of an all-optical Bose-Einstein condensate (BEC) [80].

Recently, optical nanofibers with diameters smaller than the wavelength of the guided light have attracted considerable interest in the field of quantum optics due to their high potential as light-matter interfaces. Because of the strong light confinement and thus high intense evanescent fields featured by a nanofiber for almost unlimited lengths, these fibers are ideal tools for both trapping of atoms and interfacing them to light.

In this context, various theoretical works, e.g., by Dowling and Gea-Banacloche [30], and Balykin et al. [31] followed this idea, and have proposed to realize a two-color optical dipole trap which makes use of a red-detuned and blue-detuned evanescent light field surrounding the optical nanofiber.

In this work, I demonstrate the first realization of a trap for neutral cesium atoms in the evanescent field of a nanofiber via light induced dipole forces in combination with efficient interfacing of the atoms with the fiber guided light. In the coming chapter, I introduce prerequisites of atom trapping and present our experimental setup. Furthermore, I report on the experimental characterization of our nanofiber-based trap.

3.1   Magneto-optical trap (MOT)

The magneto-optical trap (MOT) is nowadays used as a standard source of cold atoms. It became a versatile tool for many atomic physics applications: It allows one to capture and cool atoms from a dilute gas at room-temperature down to about hundred microkelvin [5], to store them for a certain time or to transfer atoms directly into other traps.

For this work, a three-dimensional MOT is employed in order to accumulate a dense cloud of cold cesium atoms around the nanofiber. By carefully adapting the parameters of the operation of the MOT a dense sample of the cold atoms can be efficiently loaded into the trapping sites surrounding the nanofiber.

The working principle of a MOT is based on cooling and trapping using spatially modulated scattering forces induced by near resonant laser light. Here, the laser cooling mechanism relies on velocity-dependent cooling forces which dissipate the kinetic energy of the atoms, and on position-dependent restoring forces which lead to spatial confinement of the atoms.
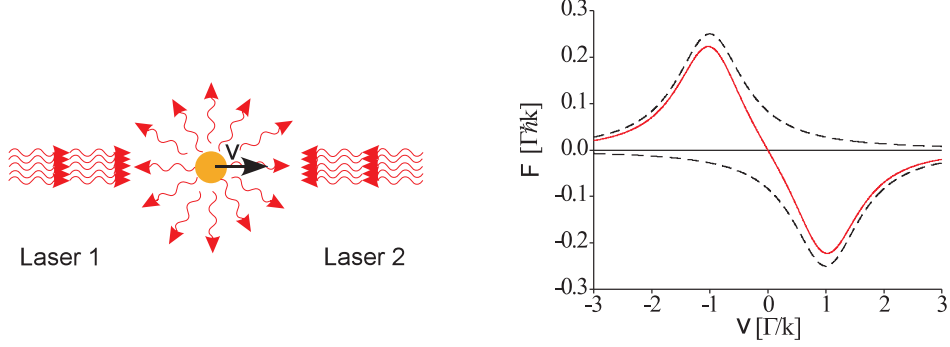
FIGURE 3.1: Doppler cooling. (a) The Doppler effect leads to preferential photon scattering from the counter-propagating beam, whereas the direction of spontaneous emission is random. (b) Light forces versus velocity for a detuning of $\Delta = -\Gamma$. The functional form of the scattering rate of the atoms leads to a Lorentzian-like force dependency on velocity (dashed lines) with maxima at $v = \Gamma/k$. The cooling force results from the combination of both forces (red solid line).

3.1.1 Doppler cooling/Velocity dependent forces

Doppler cooling can be well explained by the picture of an atom moving parallel to two counter-propagating laser beams which are slightly red-detuned ($\Delta < 0$) with respect to the atomic resonance. The Doppler shift of the resonance frequency of a moving atom compensates for the detuning and leads to preferential photon scattering of the counter-propagating laser beam. The absorption of one photon by the atom implies the change of the atomic momentum by $\hbar k$, where k is the wave number of the incident light. In the subsequent spontaneous decay, the reemission direction of the photon is arbitrary. Hence, for many such scattering events the averaged recoil momentum per photon $\langle p \rangle = \hbar k$ points into the propagation direction of the laser beam, leading to a friction-like slowing down of the atoms (see Fig. 3.1). The cooling force $F(v)$ results from the combined light forces induced by the counter-propagating laser beams and is determined by the scattering rate R_s, the average recoil momentum $\hbar k$, and the doppler shift kv

$$F(v) = \hbar k [R_s(I, \Delta - kv) - R_s(I, \Delta + kv)], \tag{3.1}$$

where

$$R_s(I, \Delta) = \frac{\Gamma}{2} \frac{I}{I_0} \left[1 + \frac{I}{I_0} + \left(\frac{2\Delta}{\Gamma} \right)^2 \right]^{-1}, \tag{3.2}$$

(see Sect. 2.1). The Lorentzian dependence of the scattering rate on the detuning (Eq .(3.2)) leads to a Lorentzian velocity dependence of the cooling force with a maximum (minimum) at $v = (-)\Delta/k$ for the respective beam. For atoms within this velocity range, the cooling force is linear in v ($F = \alpha v$), leading to a viscous drag.
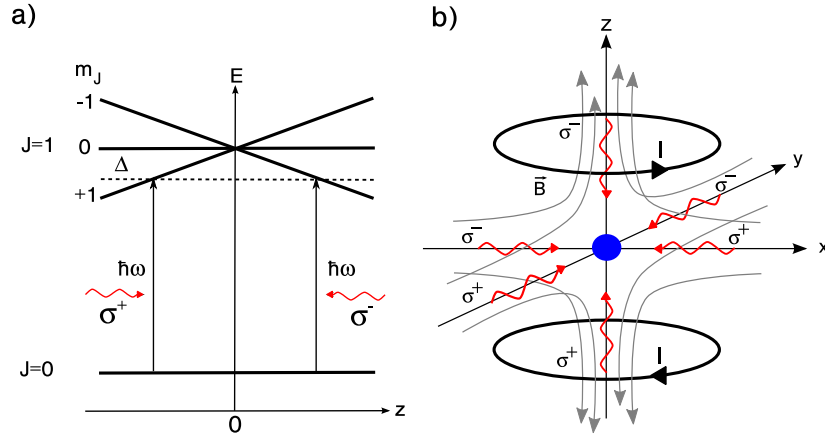
FIGURE 3.2: (a) One dimensional scheme of a magneto optical trap for atoms with ground and excited states $J = 0$ and $J' = 1$, respectively. A magnetic field $B_z = b \cdot z$ leads to a position dependent energy shift of the Zeeman sublevels (denoted by m_J). Regarding the selection rules ($\Delta m = \pm 1$) for the σ^+, σ^- polarized laser beams (red curly arrows), the laser beam which pushes the atom towards the center $z = 0$ is preferentially absorbed. (b) Six circularly polarized beams crossing at the center of the trap form the 3D-molasses. The linear magnetic field gradient is created using two coils in anti-Helmholtz configuration (circulating arrows). The direction of the magnetic field is indicated by grey lines.

Optical molasses

The straightforward extension of the Doppler cooling scheme to three dimensions is realized by three mutually orthogonal pairs of counter-propagating laser beams crossing at the trap center. In this intersection region the laser beams provide viscous friction and form an *optical molasses* for atoms moving in any direction. However, the arising viscous friction can not cool the atoms to absolute zero temperature. The randomness of the recoil due to the spontaneous emission leads to a fluctuation of the momentum around $\langle p \rangle = 0$, equivalent to a diffusive drift or a *random walk* in phase space. Thus, the atoms undergo heating and cooling at the same time. In this simple model of laser-cooling, the theoretical minimum temperature that can be reached is determined by the equilibrium of cooling and heating, which is referred to the Doppler-limit or the "Doppler temperature" defined as

$$T_D = \hbar\Gamma/2k_{\mathrm{B}}, \tag{3.3}$$

where k_{B} is the Boltzmann constant.

Position dependent force

The principle of the restoring forces in a MOT is best illustrated by a reduced one-dimensional model (see Fig. 3.2a). An atom subjected to a magnetic field whose magnitude is radially increasing from zero at the trap center, experiences a lift of the degeneracy of the excited state Zeeman multiplicity and a position dependent shift. Due to the selection rules ($\Delta m = \pm 1$) for the σ^+ and σ^- polarized laser beams respectively, an atom displaced from the center gets shifted into resonance with the beam that pushes the atom back towards the center. This extension features the great advantage that atoms can be cooled and trapped in a small volume, which results in a high density of the cold atom sample, such that atoms can efficiently be loaded into a dipole trap.

A more comprehensive theory accounting for the multilevel structure of real atoms in conjunction with spatially varying light polarization and magnetic fields predicts cooling even beyond the Doppler limit [5, 86]. In this context so-called "Sub-Doppler" cooling techniques, e.g., polarization gradient-, Sisiphus-, Raman sideband-, evaporative cooling etc., have been developed which allow to reach temperatures even beyond the recoil limit and achieve quantum degeneracy (i.e, BEC) [5, 89]. The D2-cooling transition for cesium yields a Doppler temperature of 125 μK, and the measured MOT temperature is typically $70 - 100$ μK. These values are lower than the depth of the optical potential ($U/k_B \sim 0.4$ mK) formed by the evanescent field of the nanofiber, meaning that the temperature is in principle low enough to confine the atoms inside the trap.

However, the temperature quantifies only the mean kinetic energy, the corresponding Maxwell-Boltzmann energy distribution in the MOT covers atoms with much higher energies which escape from the trap. Such an "evaporative" escape of the atoms from the high energy tail of the Maxwell-Boltzmann distribution leads to a decrease of the thermal energy of the remaining atomic ensemble.

For interacting atoms, i.e., when atoms collide during the loading, the ensemble can re-thermalize. In this case the temperature equilibrates at a value for which the atoms experience an effectively infinitely deep potential well, typically about 1/9-th of the trap depth U_0 for a three dimensional potential well [87]. As a consequence, the temperature of the captured atoms in the nanofiber trap is expected to be lower than the temperature in the MOT (see Sect. 3.4). Note that in absence of interatomic collisions the energy distribution is truncated at $E_0 = U_0$, thus without re-thermalization the temperature can be much larger than $1/9 U_0$.
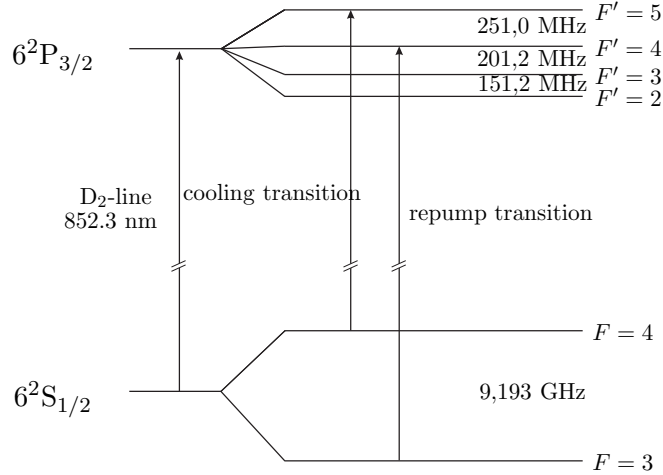
FIGURE 3.3: Hyperfine level scheme of the D2-line of the caesium atom. The arrows indicate the cooling and repump transitions.

3.2 Experimental setup

3.2.1 Cooling-Laser system

Efficient laser-cooling of atoms requires the light field formed by a single transversal radiation mode in each spatial direction, as well as frequency stability of the order less than the linewidth of the cooling transitions. For cooling in our cesium-MOT we employ the strongest of the D2-transitions (i.e., $6S_{1/2}, F = 4 \rightarrow 6P_{3/2}, F' = 5$) at 852 nm wavelength. The optical setup is depicted in Fig. 3.5. As a laser-light source we use a tapered amplifier system (TA) which is seeded by a frequency stabilized external cavity diode laser (ECDL) in Littman configuration (Sacher, TEC-420). The frequency stabilization is realized by a Doppler-free saturation spectroscopy [90, 92] and an electronic feed-back loop to the piezo actuator of the external cavity, yielding a long term stability of about 1 MHz. The amplified laser beam passes twice through an acousto-optical modulator (double-pass AOM), which is used for fast and independent control of the laser detuning and power, necessary for loading the atoms from the MOT into the dipole trap. This cooling beam is coupled into a single-mode optical fiber and split into a six pathway fiber cluster (Schäfter+Kirchhoff). Each of these fiber-ports is connected to an output collimator generating a six beam MOT with a $1/e^2$-beam diameter of 13 mm, a power of up to 30 mW per beam, and polarizations according to the requirements for position dependent forces (see Fig. 3.2(b)). The hyperfine structure of cesium with $I = 9/2$, $J = 1/2$ and $J' = 3/2$ reveals a relatively small level splitting of the excited state (see Fig. 3.3), such that the cooling laser which drives the closed transition $F = 4 \rightarrow F' = 5$ also weakly excites the $F = 4 \rightarrow F' = 4$ transition. For

the latter case, the subsequent decay branches also in the $F' = 4 \rightarrow F = 3$ channel, which results in a reduction of the population in $F = 4$. Since the atoms pumped into the $F = 3$ state are too far detuned to be coupled to the cooling beams, a weak repump laser driving the $F = 3 \rightarrow F' = 4$ transition is used to repump the population back to the $F = 4$ state. The repump laser (ECDL) (Sacher, TEC-100) is frequency stabilized in the same way as the cooling laser. Its beam is superposed with the cooling beam using a 90:10 beam splitter (BS) before entering the fiber cluster, yielding about 120 μW power per beam.

3.2.2   Vacuum setup

The operation of a MOT and a dipole trap critically depends on collisions with background gas molecules; for an adequate trap lifetime of about 1 s ultra high vacuum (UHV) conditions are mandatory (i.e., pressure $< 10^{-9}$ mbar). Our setup consists of a cylindrical stainless steel chamber ($\varnothing$200 mm $\times$ 200 mm) which contains a moveable holder for the tapered optical fiber (TOF) and a microscope objective for imaging. Optical access for the MOT beams and the camera is provided by seven view ports which are anti-reflection (AR) coated for a wavelength of 852 nm, (reflectivity $R < 0.1\%$). The two ends of the TOF enter and exit the chamber via a teflon based vacuum feed through [93]. The chamber is attached via a T-connector (CF150) to a turbo-molecular pump (Pfeiffer TPH180) and an ion-getter pump (Varian, Starcell 150), providing a pressure below 10^{-11} mbar without baking the chamber. An additional UHV gate valve (VAT, 10840) is used to separate the mechanical pumps thus enabling operation of the ion pump solely. The mechanical pumps including the pre-vacuum pump (Leybold, SC15D) are lubricant-free which avoids contamination of the vacuum. As a source of cesium, dispensers (SAES Getters) containing chemically bound cesium are used. They release atomic cesium when electrically heated at about 600° C. The cesium vapor enters the vacuum after passing an elbow pipe which avoids direct deposition of cesium on the nanofiber. The presence of cesium raises the pressure to about 8×10^{-10} mbar, indicated by the current of our ion-getter pump. We note that the pressure indicated by this gauge with electrodes covered with alkali metals is typically higher than the true value [94]. When measuring the transmission of a weak laser beam through the TOF we observe a gradually decrease of transmission due to adsorption of cesium on the nanofiber. Increasing the laser power to few ten microwatts immediately restores the initial transmission. Given that much higher powers are used for trapping, possible heating of the nanofiber to few hundreds degree Celsius might cause desorption of molecules from the fiber surface other than cesium. This would raise the collision rate with the trapped atoms in the vicinity of the fiber compared to the rest of the chamber, and would lower the trap lifetime. However, the measured lifetime of the trap (3.5 s under molasses cooling (cf. Sect. 4.2)) might suggest unchanged vacuum conditions in the vicinity of the nanofiber.

3.2.3 Magnetic fields

The magnetic field gradient in our MOT is realized by the quadrupole magnetic field created by two coils in anti-Helmholtz configuration along the z-axis ((29) in Fig. 3.4). The coils have a diameter of 200 mm and carry a current of 8 A providing a magnetic field gradient of 9 Gauss/cm. The magnetic field gradient can be electronically controlled and switched off within 1 ms ($1/e$-decay time) using a field-effect transistor (FET). In order to compensate misalignments due to stray magnetic fields we use two pairs of Helmholtz coils aligned in the x- and y-direction with respect to the coordinate system defined in Fig. 3.4. These create a constant magnetic field, which superimpose on the quadrupole field thus shift controllably the field zero point in the x, y-plane. Displacement in the z-direction can be compensated by changing the relative currents of the quadrupole coils. The required currents of the compensation coils have been found after alignment of the MOT-beams and running the MOT with a switching quadrupole field. For an applied bias field of $(2\,\mathrm{G}, 0, 0) = (\mathrm{B_x}, \mathrm{B_y}, \mathrm{B_z})$ the MOT-cloud expands isotropically in space almost without changing its center of gravity. The necessary current for this adjustment is 0.15 A for the coils in the x-direction.
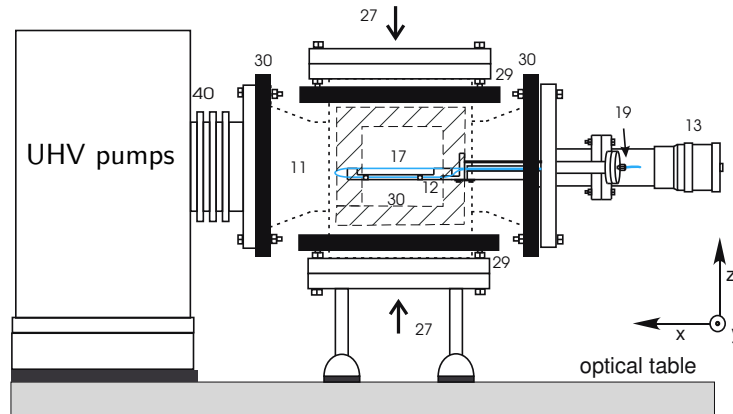
FIGURE 3.4: Schematic of the vacuum setup and the electromagnetic coils. The quadrupole coils are denoted by 29 (horizontal black bars). The compensation coils are labeled by 30. All other components are listed in Table 3.1.

FIGURE 3.5: Complete schematic of our experimental setup. All components apart from mirrors are labeled and listed in Table 3.1. The dotted and dashed arrows indicate the beam path of the red-detuned and blue-detuned laser respectively. Solid lines identify the probe, as well as the cooler and repump laser beams.

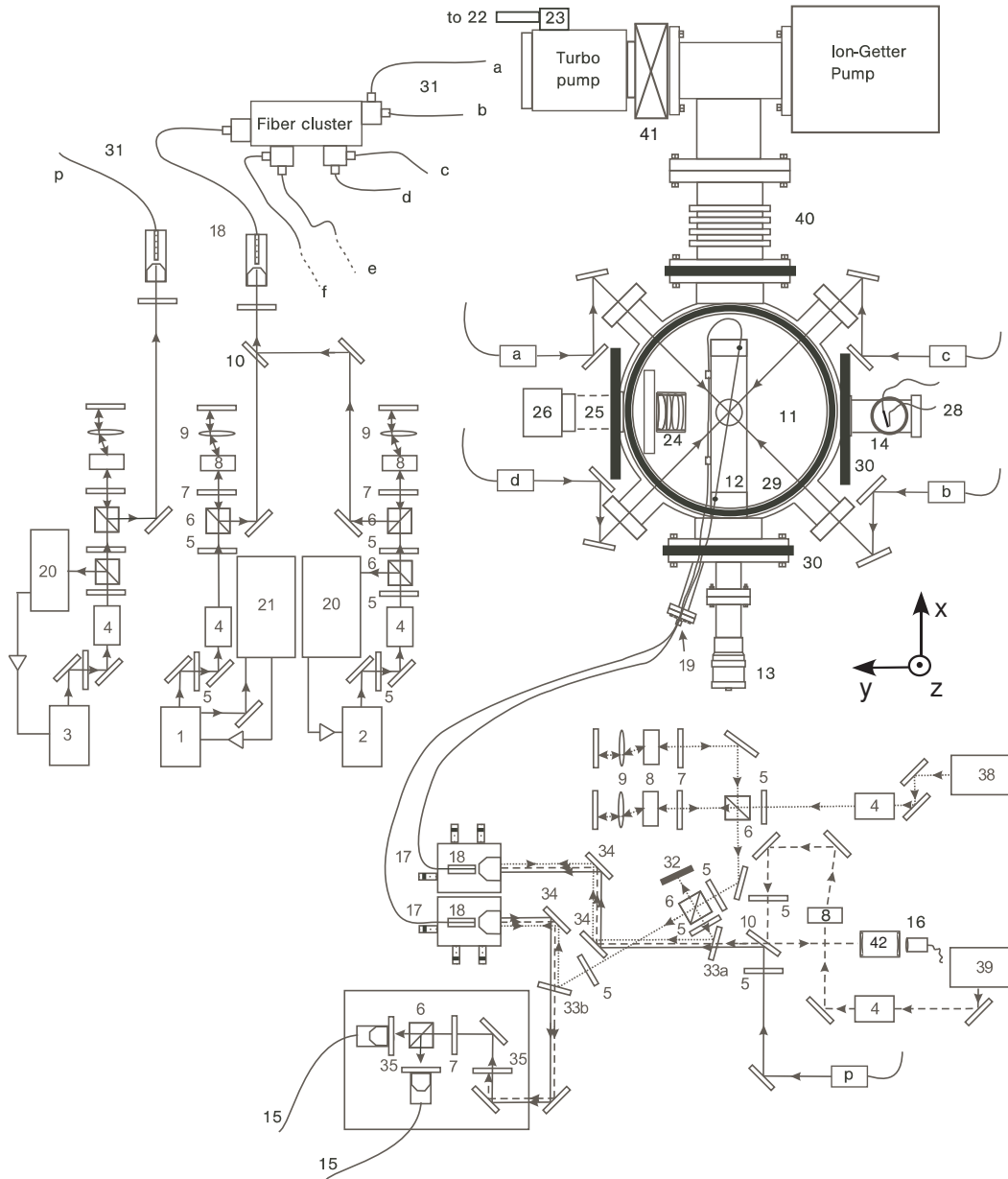| Number	Description
1	cooling laser (Sacher, TEC-420-850)
2	repump laser (Sacher, TEC-100-850)
3	probe laser (Sacher, TEC-500-850)
4	Faraday isolator
5	$\lambda/2$ plate
6	polarization beam splitter
7	$\lambda/4$ plate
8	acousto-optical modulator
9	convex lens
10	glass substrate
11	vacuum chamber
12	fiber mount
13	fiber positioner
14	Cs dispensers (SAES-Getters)
15	avalanche photodiode (APD) (PerkinElmer, C30902E)
16	photodiode
17	TOF
18	fiber coupler
19	vacuum feed-through for fibers
20	polarization spectroscopy setup
21	saturation spectroscopy setup
22	pre-vacuum pump (Leybold, SC15D)
23	pre-vacuum valve
24	microscope objective
25	camera objective
26	EMCCD camera (Andor, DU897)
27	to vertical MOT beam
28	electrical feed through
29	magnetic coils
30	compensation coils
31	polarization-maintaining optical fiber
32	beam dump
33a,b	dichroic mirrors (Laseroptik, custom made)
34	broad-band mirrors
35	optical band-pass filters $2\times$(Thorlabs, BP850)
36	optical low-pass filter (Thorlabs, LP780)
37	photodetector
38	Nd-YAG laser at 1064 nm (Spectra Physics, EXLSR-1064-650)
39	diode laser at 780 nm (Toptica LD-780-0150)
40	vibration damper
41	UHV valve (VAT, 10840)
42	Fabry-Perot spectrum analyzer

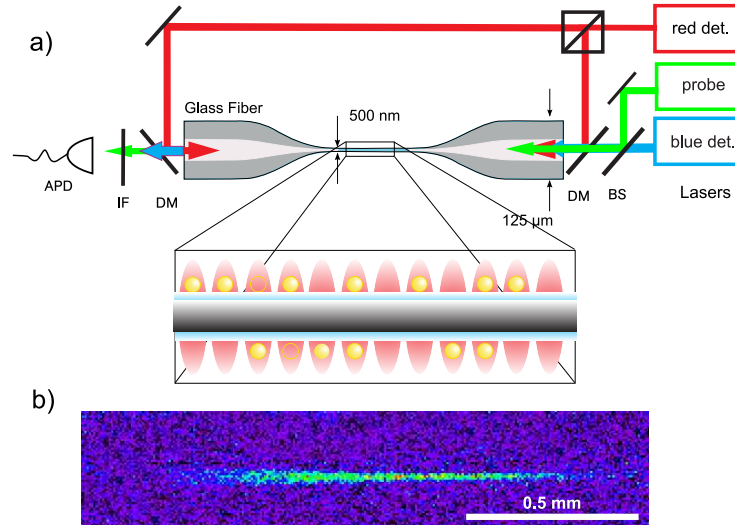TABLE 3.1: List of elements labeled in Fig. 3.5.

FIGURE 3.6:   (a) Optical setup of the fiber-based atom trap. The blue-detuned
running wave laser in combination with the red-detuned standing wave laser create
the trapping potential. A resonant laser is used for probing the atoms via the
evanescent field. (b) Fluorescence image of the trapped atomic ensemble.

3.3   Nanofiber trap

Figure 3.6 (a) shows a schematic of our nanofiber trap. We use a laser at a wave-
length of 1064 nm which is red-detuned with respect to the D1 (894 nm) and D2
(852 nm) transitions of cesium. Using a beam splitter (BS), two beams are gener-
ated and coupled into both ends of the TOF in order to realize the standing wave.
A laser at a wavelength of 780 nm is used for forming the blue-detuned potential
and is superposed with one of the red-detuned laser beams using a phase neutral
dichroic mirror (DM). The probe laser is resonant with the D2 ($F = 4 \rightarrow F' = 5$)
transition. It is superposed with the blue-detuned laser beam using a second beam
splitter and its power transmitted through the TOF (≈ 1 pW) is measured using an
avalanche photodiode (APD) in combination with an interference filter (IF). Typi-
cal powers of the trapping lasers are 2–4 mW for each of the red-detuned beams and
10–35 mW for the blue-detuned beam, depending on the desired trap positions and
depths. In the following, the powers of 2.2 mW for each of the red-detuned beams
and 25 mW for the blue-detuned beam are considered, which, in conjunction with
mutually orthogonal polarizations, yield a trap depth of about 0.4 mK at a distance
of 230 nm from the fiber surface (see Sect. 2.2, Fig. 2.3). The calculated trapping
frequencies for these parameters are 200 kHz, 300 kHz, and 140 kHz in the radial,
axial, and azimuthal direction, respectively. Large detunings of the trapping light

fields are chosen in order to ensure a low scattering rate (≈ 10 s^{-1}), compatible with a theoretical trap lifetime due to recoil heating of up to 200 s [31].

The power and detuning of each laser beam in our setup are computer controlled via the double-pass AOMs. Additionally, the current of the TA can be rapidly switched off in order to completely extinguish the cooling light. The probe laser has a short term linewidth of about 1 MHz, which allows us to resolve the natural linewidth of the $F = 4 \rightarrow F' = 5$ transition of cesium (5.2 MHz). The state of polarization of the dipole laser beams at the nanofiber waist can be monitored and aligned by observing the angular distribution of the Rayleigh scattered light using CCD cameras (see Sect. 3.3.3). The TOF has been fabricated by flame pulling of a single mode fiber (Liekki, Passive 6/125) in our computer controlled fiber pulling rig [37]. The nanofiber waist has a homogeneous diameter of 500 nm over its length of 5 mm. In the tapered sections, the weakly guided LP$_{01}$ mode of the unstretched fiber is adiabatically transformed into the strongly guided HE$_{11}$ mode of the nanofiber waist and back [11]. This results in a highly efficient coupling of light into and out of the nanofiber yielding an overall transmission through the TOF of about 99 % (cf. Sect. 1.4). The lasers are coupled into the ends of the TOF using conventional fiber couplers and the TOF enters and exits an ultra-high vacuum chamber via a vacuum feed-through [93]. Inside the chamber (pressure $\approx 8 \times 10^{-10}$ mbar), the six-beam magneto-optical trap (MOT) produces a cold cesium atom cloud with a $1/e^2$-diameter of 1.2 mm which is spatially overlapped with the nanofiber. Using this setup, we are able to transfer the atoms directly from the MOT into the trapping minima around the nanofiber just by appropriately changing the detuning and the power of the MOT beams.

3.3.1   Loading of the trap

Optical dipole traps offer a nearly conservative potential which makes it necessary to cool the atoms using dissipative light forces in order to transfer them into the trapping sites. Alternatively, the trapping fields could be switched on abruptly in order to capture atoms [76], however, this method never yields a higher atomic density inside the dipole trap than in the MOT. In addition, it strongly depends on the exact timing of both trapping lasers. We therefore employ a constantly present trap, which is found to result in a much higher atom density than provided from the MOT-cloud, thereby maximizing the number of trapped atoms.

Loading of our two-color trap is accomplished analogously to the procedure of loading a focused beam dipole trap [95]: The red- and blue-detuned trapping light fields are present in the nanofiber at all times. During the first 2 s the atoms are captured and cooled in the MOT. In the following 80 ms the atoms are transferred and cooled into the trapping minima along the nanofiber. For this purpose, the power of the MOT cooling laser, repump laser and the magnetic field gradient are
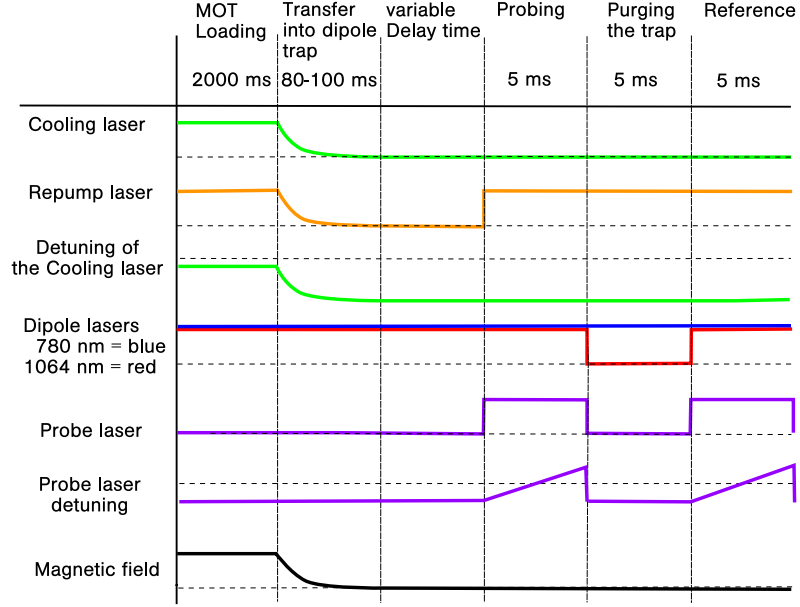
FIGURE 3.7: Timing sequence of the experiment. The colored curves show the sequences of the powers and detunings of all laser used in our setup. The dashed lines indicate the respective zero line. The magnetic field is ramped down after loading the MOT.

ramped down to zero and the negative detuning of the cooling laser is increased to about -80 MHz (see Fig. 3.7). We found that the high negative detuning of the cooling beams is crucial for loading of our nanofiber trap. Because the cesium atoms in the excited $6P_{3/2}$ state experience an inverted (repulsive) potential in the trap (see Fig. 2.5), scattering of light from the MOT-beams leads to additional heating thus to premature loss of atoms from the trap. Moreover, we find signatures of polarization gradient cooling [86] in the MOT during the loading sequence, which is found most efficient at high negative detunings and low intensities [96], resulting in a temperature of about 1/6 of the Doppler temperature (see Sect. 3.4).

Loading efficiency

The optimal loading sequence has been found empirically and corresponds to exponentially decaying functions ($\propto \exp\left(-t/\tau\right)$) of all MOT parameters, with a common time constant in the range of $\tau = 40 - 60$ ms, yielding a maximal atom number after about 100 ms of loading. For this purpose we monitored the loading procedure by measuring the absorption of the probe beam for different decay time constants τ. Here, the power of the transmitted probe light $P_{\text{out}} \propto P_{\text{in}} \exp(-\alpha N_{\text{atoms}})$ decreases exponentially with the number of trapped atoms [15], thus the absorbance ($A \equiv -\ln(P_{\text{out}}/P_{\text{in}}) \propto N_{\text{atoms}}$) indicates the number of trapped atoms.
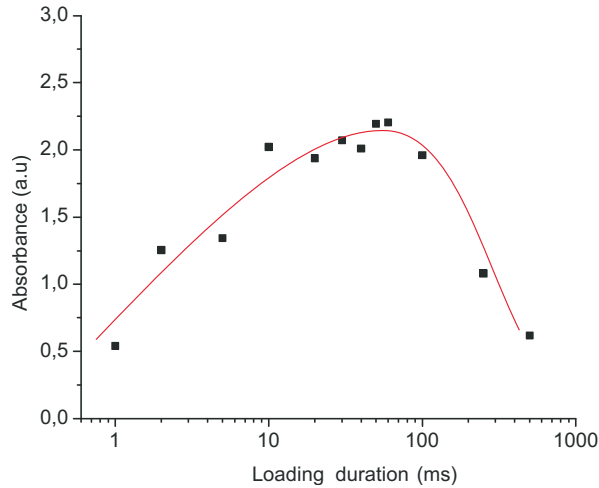
FIGURE 3.8: Loading curve of the nanofiber trap, measured from the absorption of the probe beam as a function of loading duration. Each of the data points have been taken for a loading time constant of $\tau = 50$ ms and a different loading duration (see text). The red solid line is a guide to the eye.

Figure 3.8 shows exemplarily the resulting loading curve for $\tau = 50$ ms: After filling the MOT for 2 s, the loading sequence has been applied with a fixed time constant τ and the loading duration has been varied in order to find the optimal time to interrupt this sequence. In the first 50 ms the absorbance and thus the number of trapped atoms rises exponentially and reaches a maximum already after 80 ms. For loading durations much longer than 100 ms the number of trapped atoms decreases rapidly: The substantial change in the MOT-parameters for that long time leads to an expansion of the MOT-cloud as well as to its acceleration under gravity. Hence, loading from the residual cold-atom cloud is not efficient any more and does not compensate the (light induced) losses of atoms.

In order to load as many atoms as possible, while keeping the temperature of the trap very low, we thus apply the loading sequence for 80 ms. Note that by ramping down the power of the repump laser the atoms get efficiently pumped into the lower ($F = 3$) hyperfine ground state ($> 99\%$ after 100 ms), which decouples the atoms from the cooling laser in order to reduce further heating due to scattering of light.

We further note that due to the small trapping volumes the loading is expected to operate in the so-called *collisional blockade* regime resulting in an occupancy of at most one atom per trapping site [97]. The resulting maximum average occupancy of 0.5 in conjunction with the distance of about 500 nm between the standing wave antinodes thus limits the maximum number of trapped atoms to 2000 per millimeter.
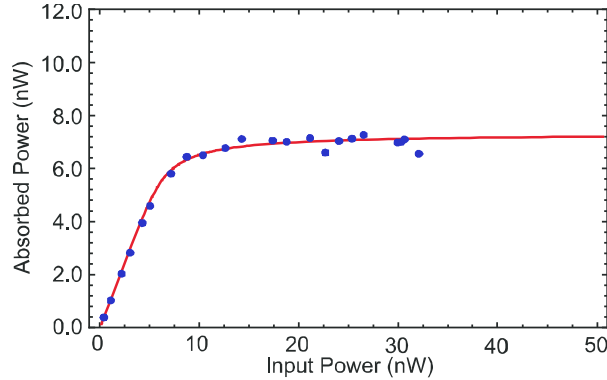
FIGURE 3.9: Saturation measurement. (blue circles) The absorbed power of the resonant fiber-guided probe light has been measured for different values of the input power. The asymptotic value of the absorbed power for strong saturation indicates the number of trapped atoms. The red line is a theoretical fit, see text.

3.3.2 Atom number measurement

In order to determine more quantitatively the number of trapped atoms, we carry out a saturation measurement: We tune the probe laser to the Stark-shifted resonance of the trapped atoms and measure the absorbed power as a function of the incident power (see Fig. 3.9). At high saturation ($s = I/I_{\mathrm{sat}} \gg 1$), the atomic ensemble absorbs about $P_{\mathrm{Abs}} \approx 7.5$ nW of probe light power. By comparing this value with the power radiated by a single fully saturated cesium atom (cf. Sect. 2.1)

$$P_{\mathrm{Cs}} = \frac{\Gamma}{2} \frac{s}{1+s} \hbar \omega_0 \approx 3.8 \text{ pW}, \tag{3.4}$$

we infer that $N = P_{\mathrm{Abs}}/P_{\mathrm{Cs}} \approx 2000$ atoms are present in the fiber-based trap. The solid red line in figure 3.9 is a theoretical fit based on a saturation model taking into account the spatially varying intensity or power $I(z) = P(z)/A_{\mathrm{eff}}$ along the atomic ensemble due to absorption

$$dP(z) = \frac{n(z)\sigma_0/A_{\mathrm{eff}}}{1 + P(z)/P_{\mathrm{sat}}} P(z) dz, \tag{3.5}$$

where $P_{\mathrm{sat}} = I_{\mathrm{sat}} A_{\mathrm{eff}}$ is the saturation power, $A_{\mathrm{eff}} = I(r)/P$ the position dependent effective optical mode area of the evanescent field (see Sect. 1.3.2), σ_0 the atomic absorption cross section on resonance, and $n(z)$ the atomic line-density ($\int_L n(z) dz = N$). The solution of this generalized Beer's law, known as Wright Omega function (or LambertW-function), can be easily evaluated numerically and is used to fit the measured dependency of the absorbed power and the incident power (i.e., $P_{\mathrm{Abs}}(L, P_0)$ vs. P_0). The resulting saturation power $P_{\mathrm{sat}} = 0.7(1)$ nW, is consistent with the saturation intensity of the cesium D2-line at a radial distance of 230 nm ($P_{\mathrm{sat}}^{\mathrm{theo}} = 0.8$ nW). For this theoretical value, we assumed orthogonal polarization (σ-polarization), evenly populated M_F states, and inhomogeneous broadening of 20 MHz of the atomic transition due to the ac-Stark shift (cf. Sect. 2.2).

3.3.3   Polarizations of the evanescent fields

The implementation of three dimensional trapping potentials around the nanofiber requires an optimal control of the polarization at the waist of the TOF. Since the TOF used in our setup is not intrinsically polarization maintaining, the state of polarization of the dipole laser beams at the nanofiber waist needs to be carefully aligned and monitored during the experiments. For this purpose, the angular distribution of the Rayleigh scattered light, which is emitted by the nanofiber, is observed via two CCD cameras aligned perpendicular to the fiber axis. Small apertures of the cameras (NA $\approx 1/140$) ensure a high angular resolution ($\delta\alpha \approx 5°$).

According to the radiation characteristics of dipole emitters, driven by linearly polarized light $I(\varphi) \propto \sin^2 \varphi$, with φ being the azimuthal angle with respect to the direction of polarization, no light should be detected along the direction in which the dipoles oscillate ($\varphi = 0, \pi$) (see Fig. 3.10 (a)). Since the HE_{11} mode carried by the nanofiber exhibits spatially varying polarization (cf. Sect. 1.3.2), polarizers (PBS) are placed in front of the cameras in order to separate the different polarization components. By rotating the plane of polarization of the input beam a sinusoidal modulation of the scattering intensities is expected, where the extinction ratio, i.e., the ratio of minimum and maximum intensity (ER)$= I_{min}/I_{max}$, indicates the degree of ellipticity of the polarization (see Fig. 3.10 (b)). Any deviation from linear polarization of the fiber-guided light, e.g., induced by a birefringent TOF, is indicated by a non-vanishing I_{min}, which can be compensated by using phase retarders (e.g., Berek-compensators or a combination of $\lambda/2$ and $\lambda/4$-wave plates).

The line profiles of the imaged scattering along the nanofiber in Fig. 3.11 show an almost uniform change of intensity with polarization angle φ. The variation of the intensity along the nanofiber is caused by surface imperfections and density fluctuations in the glass material. These randomly distributed scattering centers inside the fiber lead to almost equal observed intensities of the z- and x-polarization components. Without any separation of these components by using a polarizer, only a small angular intensity variation is observable, presumably due to the azimuthal dependence of the y-polarization component (see Fig. 3.10 (blue points)).

We note that the azimuthal phase dependency of the electric field component E_z of the HE_{11} mode (see Sect. 1.3.2) gives rise to destructive interference of the z-polarized scattered light propagating along the y-direction ($\varphi = 0, \pi$), thus reducing the minimal intensity of the x-polarization component I^x_{min} to zero (for linearly polarized fiber-guided light). The same argument holds for the electric field component E_y, therefore also I^z_{min} is expected to be zero for pure linear polarization.

The measured extinction ratios of the x- and z-polarization components reveal an average residual ellipticity of 5% and 9% with and without pre-compensation, respectively, which is compatible with the ellipticity of the beam at the output of the TOF (2% and 5%) when accounting for the angular resolution of the cameras.
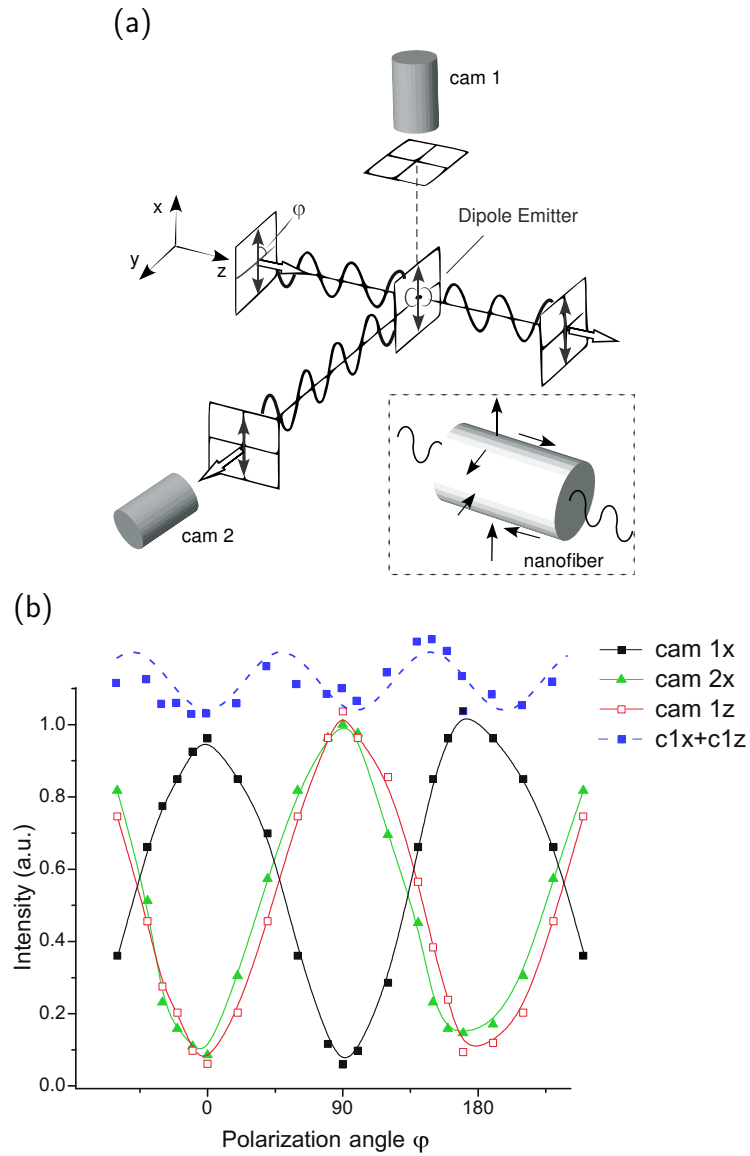
FIGURE 3.10:   The angular dependency of Rayleigh scattering visualized as the radiation pattern of a dipole emitter (a). Light which is polarized in the x-direction is preferentially scattered in the perpendicular z- and y-directions. The nanofiber provides field components in all three dimensions (see inset in (a)). The detected intensities of the z- and x-polarization components (red and black line, respectively) of camera 1 and 2 (x-component, green line) for different polarization angles φ are shown in plot (b), the solid lines are guides to the eye. The residual ellipticity of the light polarization is determined by the extinction ratio $I_{\min}/I_{\max}$. Without polarizers being used the perceived intensity (blue dashed line) varies only weakly with φ. The coordinate system is defined with respect to the polarization of incoming light. For this measurement laser light with a wavelength of 1064 nm has been used.
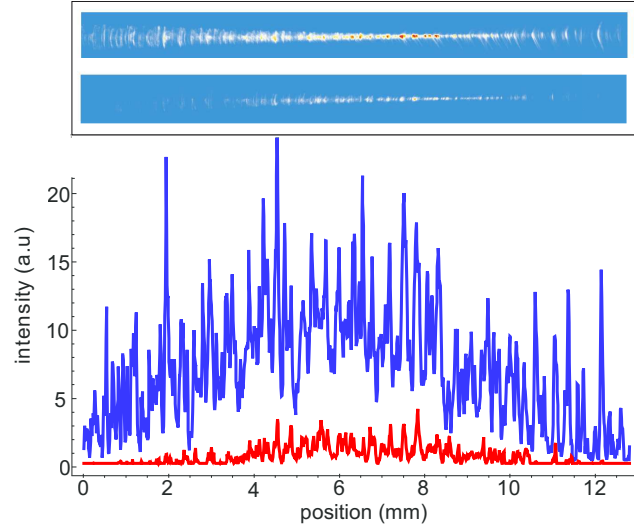
FIGURE 3.11: (top) Imaged Rayleigh scattered light ($\lambda = 1064$ nm) emitted by the nanofiber for parallel and orthogonal polarization (with respect to the image plane) yielding minimum and maximum intensity respectively. The Plot below shows the corresponding horizontal profiles for parallel (blue line) and orthogonal (red line) polarization, respectively. The nanofiber waist ranges from 4 to 9 mm.

Similar results are obtained for simultaneous transmission of the red-detuned and blue-detuned (1064 nm and 780 nm) lasers for the same configuration as used for atom trapping. In spite of their relatively large powers and intensities, the birefringence of the nanofiber due to an optical Kerr effect or due to thermal influences is negligible. Drifts of the ambient temperature, however, causes significant changes of the polarizations. Nonetheless, the temperature stabilization in our laboratory ensures a measured variation of the ellipticity of only a few percent over days.

3.3.4   Trap depth and -frequencies

For the trap configuration used throughout this work, the calculated trapping potential (see Fig. 2.3) with a trap depth of $U_0 = 0.4$ mK yields a strongly confining geometry in all three dimensions. This results in high oscillation frequencies of the trapped atoms $\nu_r = 200$ kHz, $\nu_z = 300$ kHz, and $\nu_\varphi = 140$ kHz in the radial, axial, and azimuthal direction, respectively. Here, the oscillation frequency ν_i of trapped atoms is related to the curvature $\partial_i^2 U(\mathbf{r_0})$ of the potential $(U(\mathbf{r}) = U_0 R(\mathbf{r}))$ at the trap center $\mathbf{r}_0$ in the ith direction, which is equivalent to the ith spring constant of a three dimensional harmonic oscillator, i.e.,

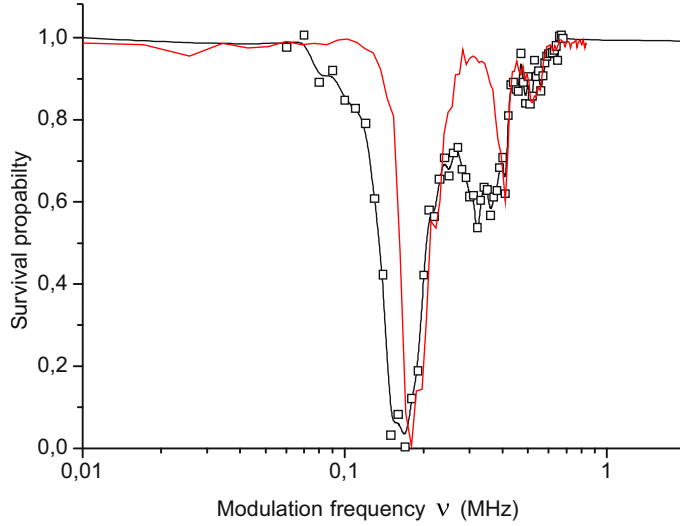$$\nu_i = \frac{1}{2\pi} \sqrt{U_0 \partial_i^2 R(\mathbf{r}_0)/m}, \tag{3.6}$$

FIGURE 3.12: Determination of the trapping frequencies. (squares) Measured survival probability as a function of the excitation frequency ν, the black line is a guide to the eye. The red curve results from a Monte-Carlo simulation of the excitation process for our trap parameters.

where m is the atomic mass. Using the expression for the classical turning point for atoms with a given energy E_0,

$$x_i = \sqrt{2E_0/(2\pi\nu_i)^2 m}, \tag{3.7}$$

we can estimate the localization of the atomic motion inside the trap.

Note that in the quantum mechanical picture, the localization of the atom is dictated by the uncertainty principle. For a harmonic oscillator the position uncertainty for minimal energy reads [5]

$$\Delta x_i = \sqrt{\frac{\hbar}{4\pi\nu_i m}}. \tag{3.8}$$

Hence, we expect a maximum confinement of atoms down to about $\Delta x_r = 22$ nm, $\Delta x_z = 28$ nm, and $\Delta x_\varphi = 33$ nm along the axial, radial, and azimuthal direction, respectively, in our trap.

Determination of the tapping frequencies

In order to verify the calculated trap geometry and to spot possible experimental imperfections we performed a measurement of the trapping frequencies. Therefore, we employed the method of resonant and parametric heat-out [6]. After loading the atoms into the trap, the power of the red-detuned trapping laser is sinusoidally

modulated with a variable frequency using the AOM, thereby modulating the trap depth and the position of the potential minimum [39]. A modulation depth of 10% of the laser power over $t_0 = 20$ ms ensures a significant parametric (and resonant) excitation of the atomic oscillation at the respective frequency. Note that for a harmonic potential, resonant and parametric excitation would occur only at frequencies ν_i and $2\nu_i$, respectively. This excitation heats up the atomic motion and results in an increased loss rate of atoms.

In Fig. 3.12 we plotted the recorded survival probability, i.e., the relative atom number $N(\nu, t_0)/N_0(t_0)$ as a function of the excitation frequency ν, where $N_0(t_0)$ corresponds to the atom number measured at the time t_0 without excitation. In this plot, significant losses around $\nu = 180 \pm 20$ kHz and $\nu = 360 \pm 50$ kHz indicate resonant and parametric excitation of the radial oscillation mode, respectively. A small dip around $\nu = 520 \pm 50$ kHz exhibits weak parametric excitation of the axial mode. The spectrum of parametric excitation of the azimuthal mode (around 280 kHz) is unresolvable because it coincides with the signatures of the radial modes. Resonant excitation of the axial and azimuthal mode is negligible because the power modulation does not change the position of the trapping minimum in these directions. The measured trapping frequencies are in good agreement with our calculations within the experimental uncertainties. Only deviations of about 10% to the low frequency side of the expected central frequencies and a slight broadening are visible.

For a better understanding of the excitation and heating process in our trap, we computed a theoretical excitation spectrum. The survival probabilities for different modulation frequencies have been obtained from numerical Monte-Carlo simulations of the classical trajectories of thermal atoms in a time-varying potential of the nanofiber trap (see Sect. 3.4). Therefore, the same parameters have been used as for the measurement. Additionally, we assumed an initial temperature of 28 μK of the atoms (see Sect. 3.4).

The resulting spectrum (see Fig. 3.12, red line) exhibits pronounced resonance dips, similar to the experimental results, showing signatures of parametric and resonant heating in our trap. The shift and broadening of these dips in both spectra reflects the anharmonicity of our potential, which, however, is less pronounced than observed in our experiments. We believe that the deviations from the theoretical spectrum originate from small misalignments of the polarizations and power drifts of the trapping lasers, which lower the trap depth and thus lead to reduced trapping frequencies. Another explanation might be a small variation of the potentials along the nanofiber. In this context, probing of the evanescent field along the nanofiber, e.g., using a second nanofiber [41], could allow one to resolve the axial intensity variation very precisely in this case.
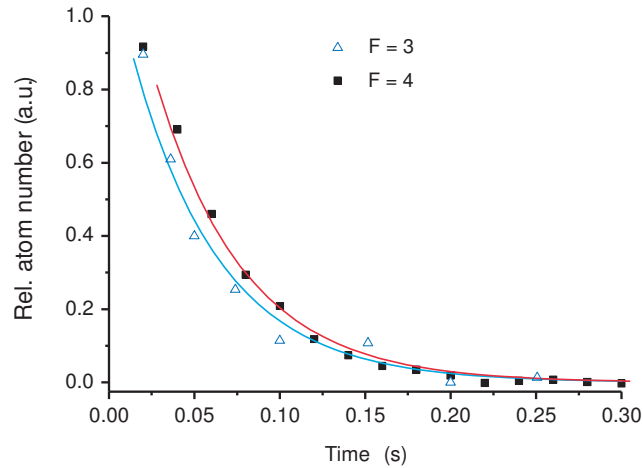
FIGURE 3.13: Evolution of the number of trapped atoms, pumped into the $F = 3$ and into the $F = 4$ state, as a function of time. The atom number decreases exponentially $\propto \exp(-t/\tau)$ with a state independent decay time ($\tau = 52 \pm 4$ ms), revealing absence of cold collisions (see text).

3.3.5   Trap lifetime

The storage time of the atoms in the trap has been examined by measuring the absorbance of fiber-guided probe light caused by the atoms for different delay times: The change of the absorbance (for a detuning of $\Delta = -20$ MHz) of the probe light was measured in discrete time steps for each individual experimental run. We find that the absorbance, and thus the number of stored atoms, decreases exponentially with a time constant of about 50 ms, smaller than what would be expected from losses due to background-gas collisions for the measured pressure in our vacuum chamber (≈ 4 s) [98] and from recoil heating due to light scattering (200 s).

The same short time constants have been found for a range of trap configurations, i.e., varying the trap depth and position from 0.2 mK to 1 mK, and 200 nm to 350 nm distance from the surface, respectively. For much higher trap depths, the cooling seems to be inefficient, which becomes apparent due to the low atom number in the and the rapid atom losses.

At shorter distances from the fiber surface or lower potential depths, the confinement in the trapping sites is less robust against power fluctuation [39] which also results in higher atom losses. Only lowering of the axial confinement, while keeping reasonable trap depth by unbalancing our standing wave potential ($P_{\mathrm{red1}} = 4.6$ and $P_{\mathrm{red2}} = 0.6$ mW), leads to a small improvement of the lifetime up to 85 ms. This result gives rise to the assumption that position fluctuations in axial direction, presumably due to phase fluctuations of the trapping fields, have a substantial impact on the trap lifetime (see Sect. 3.5.4). For a further decrease of the axial

confinement, the lifetime reduces again to about 40 ms, because the atoms leave the 5 mm wide trapping region due to thermal motion along the nanofiber. We note that in all relevant cases atom losses due to tunneling towards the fiber surface is negligible because of the high repulsive potential barrier in our trap. Also surface interactions are expected to be negligible at distances larger than 100 nm due to the low conductivity of glass [105, 106].

We further note that by employing molasses cooling of the atoms during the storage time, using the MOT-beams with a detuning of $\Delta \approx -80$ MHz and relatively low intensities ($I/I_\mathrm{sat} \approx 1$), we are able to compensate heating and losses in our trap. The maximal trap lifetime measured in fluorescence experiments (see Sect. 4.2) is found to be $\tau = 3.5(2)$ s, which is expected to be limited only due to background-gas collisions.

Cold collisions

In order to investigate the influence of *hyperfine-changing* collisions (HFC) on the atom losses, and to estimate the number of atoms trapped in each potential well, we performed the lifetime measurements for atoms prepared in the $F = 4$ and the $F = 3$ hyperfine ground state, respectively. Since atom losses due to HFC occur if at least one of the colliding cold atoms is in the energetic higher hyperfine ground state (i.e., $F = 4$) [99]; the energy released from the collision-induced $F = 4 \rightarrow F = 3$ transition suffices to expel the atoms from the trap. For the low volume of each trapping sites and high oscillation frequencies these collision between cesium atoms would lead to rapid atom losses (< 100 μs) [99]. Collisions within a pure $F = 3$ population, however, should not show any significant influence on the trap lifetime [6]. We therefore optically pumped the trapped atoms, while loading them into the nanofiber trap, into one of the desired states with high purity ($\gtrsim 99\%$), and checked that the population stayed unchanged until each measurement was performed. For probing of the "dark" $F = 3$ population the atoms were repumped to the "bright" $F = 4$ state after the respective delay time using the repump beams of our MOT.

The evolution of the atom number of the trapped ensemble, pumped into the $F = 3$ and into the $F = 4$ state, are shown in Fig. 3.13. We find that the lifetime of the trapped atoms is independent of the hyperfine ground state population. Thus, we can conclude that no such HFC collisions between the atoms occur after loading the trap. Furthermore, this result confirms that an occupancy of at most one atom per trapping site is already reached due to light-induced collisions caused by the MOT-beams during the loading procedure.

With regard to the negligible cold- or background gas collisions, heating is expected to be the dominant loss mechanism in our trap. This will be the subject of the next sections.

3.4   Temperature measurement

Since the temperature is determined by the balance of heating and cooling processes, the detailed study of the temperature of the atoms trapped in the evanescent field of a nanofiber might reveal possible technical or physical origins of heating and limits of cooling mechanisms. Moreover, the measurement of the temperature provides information about the confinement of atoms in our trap, which is of importance in regard to the interaction of the atoms and light. For example, the thermal motion of the atoms in a dipole trap leads to inhomogeneous broadening of their transition frequencies due to spatial dependent light shifts. In addition, the delocalization with respect to the propagation direction of the fiber-guided light leads to dephasing of the atoms with respect to the probe field, and thus limits the coherence time of light-atom interactions.

Method

The temperature of a small sample of cold atoms is not directly accessible, e.g., by contact measurement, but can be deduced from the position, momentum or energy distribution. A time-of-flight measurement as it is used for the temperature measurement in, e.g., focused beam traps [6], cannot be applied because of the atoms' close proximity to the fiber surface. Thus, we will follow the approach of *adiabatic lowering* of the trap reviewed by W. Alt [100]. This method relies on a slow lowering of the trap depth from initial value U_0 to U_{low} such that only the atoms with energies smaller than a certain threshold E will remain trapped. For such an adiabatic lowering, the threshold energy E is only dependent on the final trap depth U_{low}. By an appropriate change of U_{low} the energy threshold E can be varied in order to find the cumulative energy distribution, out of which the temperature can be estimated.

The adiabadicity criterion is to change the dipole potential on a time scale longer than the largest oscillation period. An optimized time sequence of $U(t)$ for an anharmonic potential is found by [100]

$$U(t) = \begin{cases} U_0 & \text{for } t = 0 \\[2ex] U_0 \left(1 - \frac{t^2}{4T_c^2}\right) & \text{for } 0 < t < T_c\sqrt{2} \\[2ex] U_0 \frac{T_c^2}{t^2} & \text{for } t > T_c\sqrt{2} \end{cases} \tag{3.9}$$

with the critical time $T_c \approx 10 \times 2\pi/\Omega_\varphi = 0.1$ ms. In view of the high anharmonicity of our trapping potential we further reduced the lowering time by a factor of 10 (see Fig. 3.14).
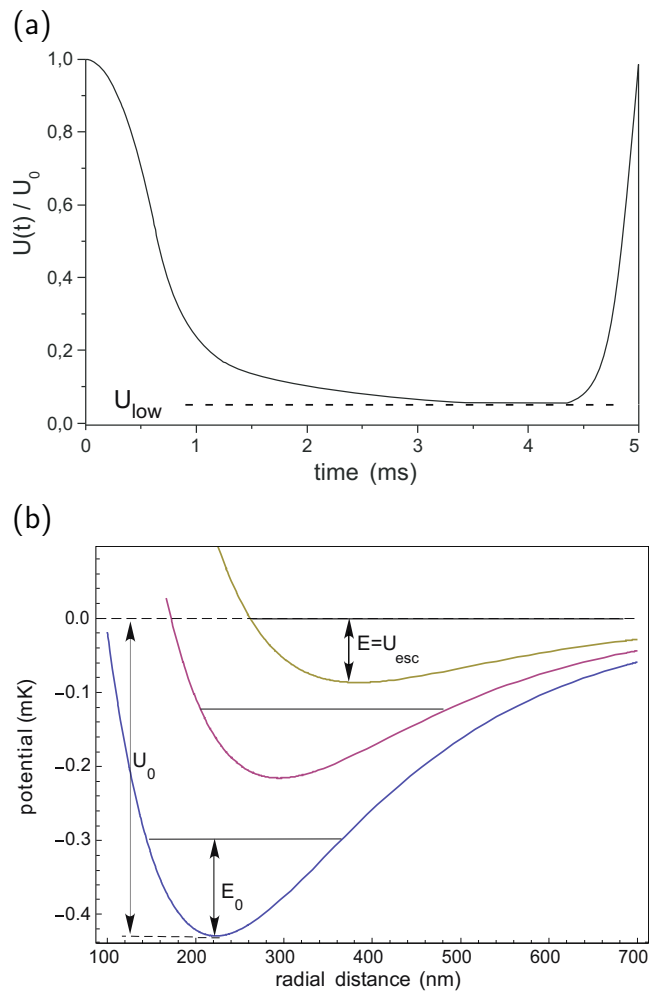
FIGURE 3.14:   (a) Time sequence $U(t)$ optimized for adiabatically lowering of
the trap depth. (b) By lowering the potential depth from U_0 to U_{low} the atomic
energy E decreases from the initial value E_0 due to adiabatic cooling. Since E
decreases slower than U the atom escapes from the trap if the energy reaches the
potential depth U_{esc}.

The adiabatic reduction of the depth of a "conservative" potential does not conserve energy, but it is rather the action integral over one oscillation period,

$$S = \oint p \, dx = \sqrt{2m} \oint \sqrt{E - U(x)} \, dx, \tag{3.10}$$

which is conserved [103]. In this case, it can be shown that the energy E of the atom is reduced due to "adiabatic cooling", but this is less than proportionally with respect to U. Hence, at a certain depth U_{esc}, when the energy E reaches the threshold U_{esc}, the atom escapes from the trap. The threshold energy $E_{\mathrm{esc}} = U_{\mathrm{esc}}$, in this case, is lower than the initial energy ($E_{\mathrm{esc}} < E_0$) (see Fig. 3.14 (a)). As a consequence, the measurement of the energy distribution in this way is inherently affected by adiabatic cooling, which has to be considered in our experimental results.

Experimental realization

The experimental procedure of the measurement of the temperature was performed directly after loading about 2000 atoms into the trap with an initial trap depth of $U_0 = 0.4$ mK. The potential was lowered afterwards according to Eq. (3.9) by changing the power of the red-detuned laser using the AOM. In order to detect the fraction of "surviving" atoms we measured the absorption of a detuned light pulse of 0.5 ms length before lowering the trap and after restoring the original potential with the same radial distance to the fiber. The restoring ramp does not have to follow the adiabatic form, since no atoms are lost upon increasing the trap depth. A low power of the probe light ensures that the scattering rate of the atoms (30 kHz) is small compared to their oscillation frequency in the trap ($\gtrsim 140$ kHz), thereby reducing the effects of recoil heating [127]. By this means, we find a loss rate of less than 10% after 5 ms without any lowering of the potential. The measurements for differently lowered potential depths (U_{low}) result in an altered energy distribution, which needs to be corrected by transforming U_{low} into the corresponding initial energy E_0. Since no analytic expression is known accounting for adiabatic cooling in the anisotropic potential of our trap, we performed a numerical Monte-Carlo simulation in order to find the adequate relation between U_{esc} and E_0 (see Fig. 3.15).

Numerical simulation

For estimation of the effects of adiabatic lowering of our trap (and to estimate the effects of parametric and resonant heating (see Sect. 3.3.4)), we have carried out a numerical simulation of the motion of atoms inside the three dimensional time-varying potential of our nanofiber trap $V(r, \varphi, z, t) = U(t)R(r)\cos(2\varphi)\cos^2(\beta z) + $ (v.d.W+gravity) (cf. Sect. 2.3). For that purpose, the classical equations of motion have been solved numerically using the Kutta-Merson algorithm [104], implemented into a C^{++} programm.
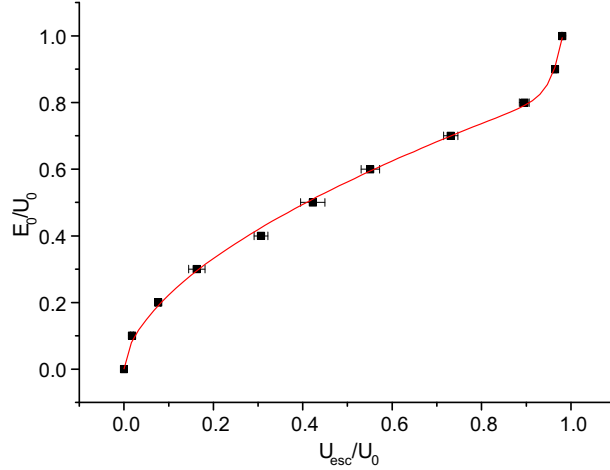
FIGURE 3.15: Initial energy E_0 as a function of the escape depth U_{esc}. The data points are obtained from a Monte-Carlo simulation of $10,000$ trajectories in the 3D-potential well of our trap. The error bars indicate the escape range. The red line represent a fit using an analytic function ($y = ax^b + cx^d$).

This simulation of the atomic trajectories has been performed under the same conditions (i.e., trap depth and lowering function $U(t)$) as the measurement. In order to enhance the calculational speed the radial potential function $R(r)$ was approximated as a sum of two exponential functions fitted to the exact solutions of the red- and blue-detuned fields. In this program, the chosen accuracy (10^{-3}) is compatible to a step time of 3 ns. The atomic trajectories for different initial energies E_0 are calculated as $U(t)$ is varied according Eq. (3.9). The final depth U_{low} is held for 1 ms such that all unbound atoms have enough time to leave the trap. If the atoms displace reasonably far from the trap center, i.e., more than 2 μm, $\pi/2$ and 250 nm in radial, azimuthal and axial direction from the trap minimum, respectively, they are considered as lost. This procedure is repeated many times for random starting positions (with respect to E_0) and phases of the atomic oscillation in order to find the probability $p(E_0, U_{low})$ of an atom remaining trapped for a certain E_0 and U_{low}. The obtained probability distribution $p(E_0, U_{low})$ runs from unity to zero for an decreasing U_{low}. Here, the escape depth U_{esc} is defined as the lowered depth (U_{low}) for which $p(E_0, U_{low}) = 0.5$, the according escape range ΔU_{esc} defines the energy resolution. Both quantities are obtained by fitting an error-function $\mathrm{erf}\{(U_{low} - U_{esc})/\Delta U_{esc}\}$ on $p(E_0, U_{low})$.

The resulting relation between U_{esc} and E_0, evaluated from eleven sets of simulations with different E_0, is plotted in Fig. 3.15. The non-linear dependency of the escape depth on the initial energy, where E_0 is larger than U_{esc}, suggests adiabatic cooling for atoms with energies $E_0 < 0.7U_0$. For atomic energies approaching the trap depth U_0 lowering of the potential according Eq. 3.9 in our simulations results in raising of the escape depth (i.e, $U_{esc} > E_0$), probably because lowering of the trap in this case is not adiabatic anymore.
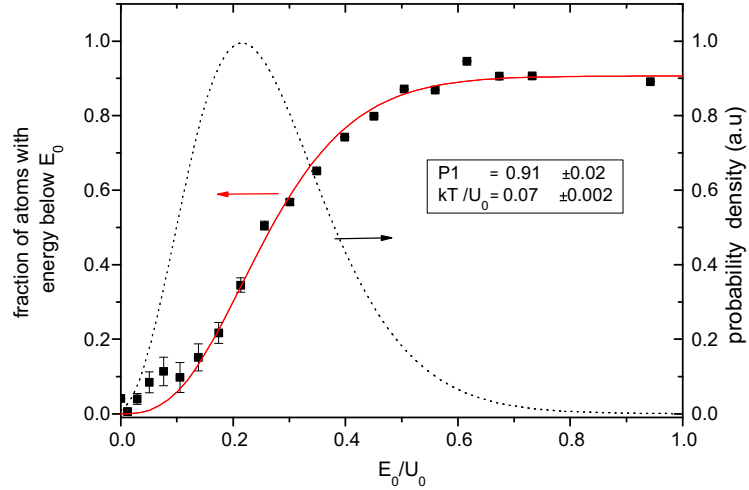
FIGURE 3.16: Cumulative energy distribution of the trapped atoms. The data points are obtained from the measured survival probability as a function the lowered potential U_{low}. The former dependency on U_{low} is transformed into E_0 dependency using the results from the Monte-Carlo simulation in Fig. 3.15. The fit of the cumulative Maxwell-Boltzmann distribution (red line) in our trap yields a temperature of 28 μK (see text). The dotted line indicates the corresponding energy distribution.

For further utilization of the results obtained from the simulations, an analytic function was fitted to the data points. This function was applied to the experimental data in order to extract the true (cumulative) energy distribution from our measurement (see Fig. 3.16).

Results

The corrected cumulative energy distribution (see Fig. 3.16), i.e., the fraction of atoms with an energy below E_0, is well described by the integrated Boltzmann-distribution

$$P(E_0, T) = P_{\max} \int_0^{E_0} \frac{g(E)}{Z(T)} e^{-E/k_B T} \, dE, \tag{3.11}$$

where

$$g(E) = \frac{2\pi(2M)^{3/2}}{h^3} \int_{V(E)} \sqrt{E - U(\mathbf{r})} d^3 r \tag{3.12}$$

denotes the density of states [107], and $Z(T)$ is an appropriately chosen normalization function, where k_B is the Boltzmann constant and T is the temperature. For $E \ll U_0$ the latter integral yields approximately

$$g(E/U_0) \propto \frac{E^2}{2U_0^2} + \frac{E^4}{4U_0^4} + \mathcal{O}(\frac{E^6}{U_0^6}). \tag{3.13}$$

Using this approximation, the resulting fit of $P(E_0, T)$ (Eq. (3.11)) on our data yields a temperature of $k_B T = 0.070(2) \, U_0$ and a maximum survival probability of $P_{\max} = 91\%$. For the calculated trap depth of $U_0 = 0.4$ mK we obtain a temperature of $T = 28 \pm 1 \, \mu$K. This value is lower than the Doppler temperature (125 μK), and even lower than what would be expected when taking evaporative cooling solely into account ($T \approx 1/9 \, U_0$) [87, 108] (see Sect. 3.1). Hence, we can conclude that sub-Doppler cooling mechanisms [5, 86] may operate even in the presence of the nanofiber and the trapping fields, which might indicate a viable way of further cooling the atoms.

By knowing the temperature, we can estimate the occupation of the vibrational states and the localization of the atoms inside the trap. The mean occupation number is defined by [110]

$$\langle n_i \rangle = \frac{1}{e^{\hbar \Omega_i / k_B T} - 1}. \tag{3.14}$$

With the measured trapping frequencies $\nu_i (= \Omega_i / 2\pi)$ from Sect. 3.3.4, we obtain $\langle n_z \rangle = 1.4$, $\langle n_r \rangle = 2.5$, and $\langle n_\varphi \rangle = 3.8$. These low mean occupation numbers indicate that the atoms can be found very close to the vibrational ground state of the respective oscillatory mode. The corresponding extension of the atomic motion in each spatial direction, estimated from the $1/\sqrt{e}$-widths of the harmonic-oscillator wave function modulus squared,

$$|\Psi(x_i)|^2 \propto \sum_n \left| H_n(\sqrt{m\Omega_i/\hbar} x_i) e^{-m\Omega_i x_i^2 / 2\hbar} \right|^2 e^{-n\hbar\Omega_i / k_B T}, \tag{3.15}$$

where H_n are the Hermite polynomials, yields only about twice the spatial extension of the oscillatory ground state wave function in each direction, i.e., $\Delta z \approx 42$ nm, $\Delta r \approx 67$ nm, and $r\Delta\varphi \approx 92$ nm for the axial, radial and azimuthal direction, respectively.

3.5 Heating-rates

The method of temperature measurement described in the previous section is used now in order to estimate the total heating rate of the atoms during the storage in our trap. We measured the temperature for different delay times after loading the trap and switching off the MOT-beams. Figure 3.17 shows the progression of the temperature in the first 100 ms, starting at $T \approx 0.07 U_0 = 28 \, \mu$K and converging towards a maximum value. During this time the number of atoms reduces exponentially to 13.5% according to $N = N_0 \exp(-t/50 \text{ ms})$. The increase of temperature in the first 100 ms resembles a similar time dependency; the fit of a simple exponential model $T(t) = T_{\max} - T_0 \exp(-t/\tau)$ on the measured data points indicates that both follow the same e-folding time of $\tau \approx 50$ ms. The correlation of the time evolution of the temperature and the time evolution of the
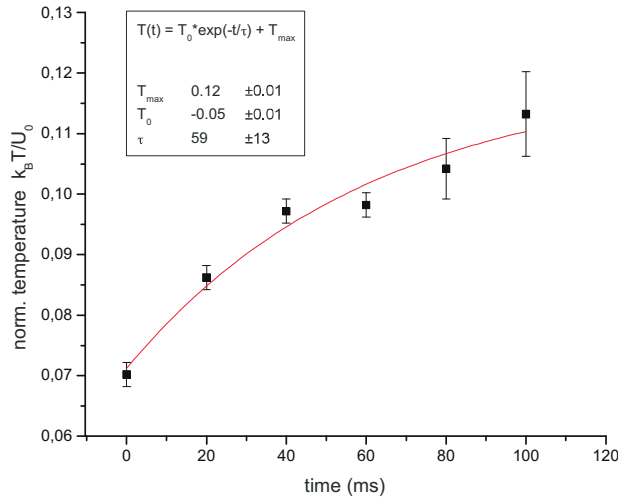
FIGURE 3.17: (black points) Measured temperature as a function of storage time. The red line is a fit (see text). Note that the increase of the temperature is accompanied with an exponential decrease of the atom number $N = N_0 \exp(-t/50 \text{ ms})$.

atom number may suggest that atom losses arise due to heating inside the trap, which is found to be more pronounced than what one would expect from simply considering scattering of photons from the trapping fields. In the following section several sources of heating are discussed and their contributions are evaluated. The analysis of the fundamental and technical heating effects in our trap is intended to quantify heating- and loss-mechanisms arising for the storage of the atoms.

3.5.1 Recoil heating

One fundamental heating mechanism in an optical dipole trap arises from spontaneous scattering of photons of the dipole fields. The absorption and emission of a photon transfers each on average the recoil energy

$$E_r = \frac{(\hbar k)^2}{2m} \tag{3.16}$$

to the atom [6], where k denotes the wave number of the photons. For a random momentum transfer at the rate R_s the average atomic energy increases by [6]

$$\langle \dot{E} \rangle = 2 R_s E_r. \tag{3.17}$$

For a potential depth U and detuning of the dipole laser frequency ($\Delta \gg \Gamma$) the scattering rate is given by $R_s = U \frac{\Gamma}{\hbar \Delta}$ (cf. Sect. 2.1). Due to the large detunings of both of our dipole trap lasers and a trap depth of $U/k_B = 0.4$ mK, only a low scattering rate of $R_s = 10 \text{ s}^{-1}$ is expected, producing a negligible heating rate of $4 \ \mu\text{K/s}$.
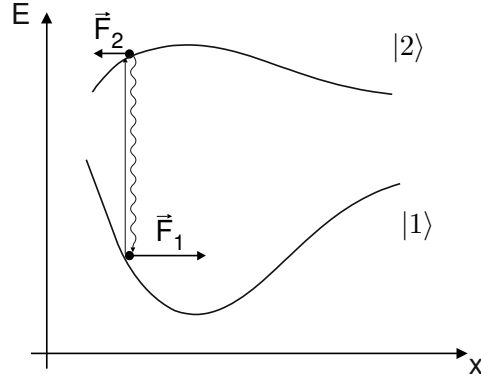
FIGURE 3.18:   Illustration of heating induced by dipole force fluctuation.   The
dipole force changes from F_1 to F_2 upon excitation from state $|1\rangle$ to $|2\rangle$

3.5.2   Heating due to dipole-force fluctuations

Another form of heating arises if an atom undergoes a transition from the ground
state $|1\rangle$ to the excited state $|2\rangle$. In this case, the atom experiences a repulsive po-
tential during its lifetime in state $|2\rangle$ (see Sect. 2.2). Several such random excitations
result in *fluctuating dipole forces* which lead to heating of the atomic motion. For
oppositely curved potentials the dipole force is changed by $\Delta F = \nabla U_1(\mathbf{r}) - \nabla U_2(\mathbf{r})$
for the lifetime $\tau = 1/\Gamma$ of the excited state. This force transfers momentum of
$\Delta p = \Delta F \tau$ in the stationary case, i.e., if the oscillation period $T_{\mathrm{osc}} = 2\pi/\Omega$ is
large compared to τ (30 ns), as in our case. In analogy to recoil heating, these
momentum kicks drive random walks in momentum space. The energies of these
kicks averages to

$$\langle E_{\mathrm{kick}} \rangle = \frac{(\Delta p)^2}{2m},\tag{3.18}$$

and result in the heating rate

$$\langle \dot{E} \rangle = R_{\mathrm{exc}} \langle E_{\mathrm{kick}} \rangle .\tag{3.19}$$

For a real atom this effect is, however, state selective in the hyperfine- and Zeeman
sub-levels (cf. Fig. 2.5 in Sect. 2.3). In our case, the maximum energy of $\langle E_{\mathrm{kick}} \rangle =$
3 μK is obtained for the excitation to the $|6P_{3/2}, F = 5, M = 0\rangle$ state, assuming
an thermal energy of $E = 0.5\, U_0$ of the atom. Note that for atoms excited to the
$6P_{1/2}$ states $\langle E_{\mathrm{kick}} \rangle$ is negligible small (see Sect. 2.2).

In the case of off-resonant scattering of the trap light the excitation rate is given
by [63]

$$R_{\mathrm{exc}} = \frac{R_s^2}{\Gamma}.\tag{3.20}$$

The scattering rate in our trap yields $R_{\mathrm{exc}} \approx 10^{-6}\mathrm{s}^{-1}$, which results in a completely
negligible heating rate below 10^{-9} mK/s.

If, however, near-resonant light interacts with the trapped atoms, e.g., for optical pumping or for probing of the atoms, then the excitation rate becomes equal to the scattering rate, which can be significant. As an example, the typical power of our resonant probe beam of 1 pW yields an excitation rate of $R_{\mathrm{exc}} = 30$ kHz to the $6P_{3/2}$ state. For an exposure time of 0.5 ms, as used for the temperature measurement, the temperature increases by about 6 μK. Here, the energy dependent heating rate changes the temperature by 2 μK, 3 μK, 1 μK in the radial, axial and azimuthal direction, respectively. Thus, in order to avoid the excitation of higher vibrational modes in the trap, the pulse length Δt or the number of scattered photons ($N_{\mathrm{phot}} = \Delta t R_{\mathrm{sc}}$) should be kept small.

In general, resonant excitation can be fully suppressed during the storage time by careful shielding of the experimental setup against resonant scattered light. However, for our case, the blue-detuned laser light propagating inside the nanofiber induces fluorescence of the glass material, producing about 10^{-4} pW of (near) resonant light in a frequency band of $\Delta \omega = 2\Gamma$. The corresponding scattering rate is estimated to be at a level of $R_{\mathrm{exc}} \approx 1$ s^{-1}, which gives a lower limit of our heating rate of about 3 μK/s.

3.5.3 Potential fluctuations

Technical noise induced by the lasers themselves or the control units of the AOMs can have a strong impact on the intensity or phase stability of the trapping light fields. Any variations of these parameters are changing the geometry of trapping potentials. Fluctuations in the potential depth, in the Fourier domain at twice the trapping frequency, affect the amplitude of the oscillatory motion, an effect that is referred as parametric heating. Position fluctuation of the potential minimum in resonance with the trapping frequencies, strongly influences the atomic oscillation as well. Single fluctuations of both kinds can either increase or decrease the oscillatory energy of a given atom. However, the stochastic nature of these fluctuations always leads to heating.

Parametric heating

Because of the power dependency of the trap depth $U_0 \propto P$, fluctuations of the laser power result in fluctuations of the trap depth and therefore cause fluctuations in the spring constant of the trap. This parametric heating effect is thus determined by the amplitude and the spectral distribution of the laser power fluctuations $\Delta P = P(t) - \langle P \rangle$ around $\langle P \rangle$. The only relevant contribution of these fluctuations to heating is found in the spectral region close to twice the trapping frequency ($2\nu_i$). Any excitations at other frequencies will dephase with respect to the oscillatory motion of the atom and will thus on average not lead to heating.

An important quantity concerning these processes is thus the spectral density of the relative power noise $S_P(\nu)$, which is related to the normalized variance of the power or the potential in a spectral band $d\nu$ around the frequency ν by

$$S_P(\nu)\,\mathrm{d}\nu = \frac{\left\langle \Delta P^2 \right\rangle_{d\nu}}{\left\langle P \right\rangle^2} = \frac{\left\langle \Delta U^2 \right\rangle_{d\nu}}{\left\langle U \right\rangle^2} \tag{3.21}$$

and thus

$$\int_0^\infty S_P(\nu)\,\mathrm{d}\nu = \frac{\left\langle \Delta P^2 \right\rangle}{\left\langle P \right\rangle^2} = \frac{\left\langle \Delta U^2 \right\rangle}{\left\langle U \right\rangle^2}. \tag{3.22}$$

Here and in the following, the notation $\nu(=\omega/2\pi)$ for the frequencies in units of Hertz is used.

For a harmonically approximated potential $U(x_i) \propto x_i^2$ and small variations of the power $(\Delta P \ll \langle P \rangle)$ at the frequency $2\nu_i$, the classical as well as the quantum mechanical calculation of the equation of motion yield an exponential growth of the mean energy in time [108, 109]

$$\langle \dot{E} \rangle = \pi^2 \nu_i^2 S_P(2\nu_i) \langle E \rangle. \tag{3.23}$$

Note that the quadratic term ν_i^2 makes parametric heating most efficient at high oscillation frequencies, i.e., strongly confining trap geometries are very sensitive to heating due to power fluctuation.

For our two-color dipole trap the sum of the two individual potentials results in a potential well with a depth and radial position that strongly depends on the relative values of P_{red} and P_{blue}. Small variations of these powers have a stronger effect on the total potential than on each individual. More quantitatively, the power fluctuations of the respective lasers results in a factor $c_{\mathrm{red}} \approx 3$ and $c_{\mathrm{blue}} \approx 2$ times higher potential variation as compared to the respective individual potentials.

We recorded the intensity noise spectra or the spectral variance of both lasers at the output of the TOF using a fast photodiode and an electronic spectrum analyzer (Agilent, E4407) (see Fig. 3.19). The relative intensity noise is obtained by dividing the spectrum by the DC output voltage. At low frequencies the $1/f$-noise is apparently as well as several peaks from the switching power supplies of the lasers or relaxation oscillations. In the relevant region from 100 kHz to 1 MHz the spectrum is essentially flat and reaches the shot noise limit of the DC photo current. The obtained noise level is thus only an upper limit. Integration of the power spectrum $S_{\mathrm{red}}(\nu)$ of the red-detuned laser yields a slightly higher rms noise level of 0.3% than specified by the manufacturer ($< 0.2\%$). For the blue-detuned laser the measured rms noise level yields 1%. Using Eq. (3.23), we estimate the maximum heating rate for the measured noise of the individual laser and the combined total value ($\langle \dot{E}_{\mathrm{tot}} \rangle = c_{\mathrm{red}} \langle \dot{E}_{\mathrm{red}} \rangle + c_{\mathrm{blue}} \langle \dot{E}_{\mathrm{blue}} \rangle$), respectively (see Fig. 3.19(b)), assuming an energy of $E = U_0/2$. The maximum heating rate is expected for the axial mode ($2\nu_z = 600$ kHz), yielding only a negligible value of $\langle \dot{E} \rangle = 10$ μK/s.
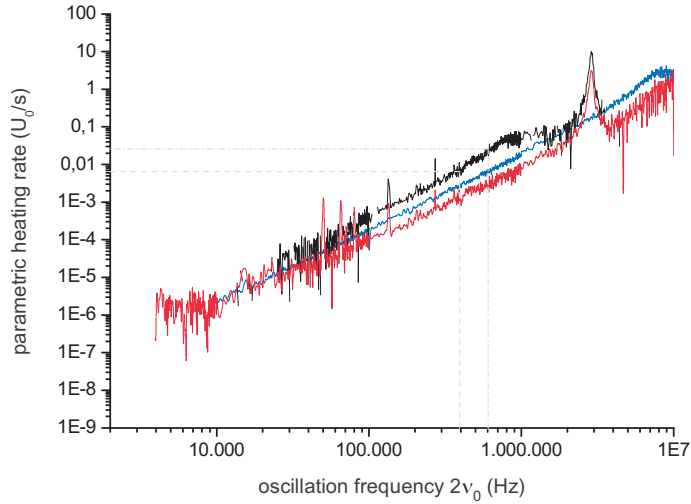
(a)
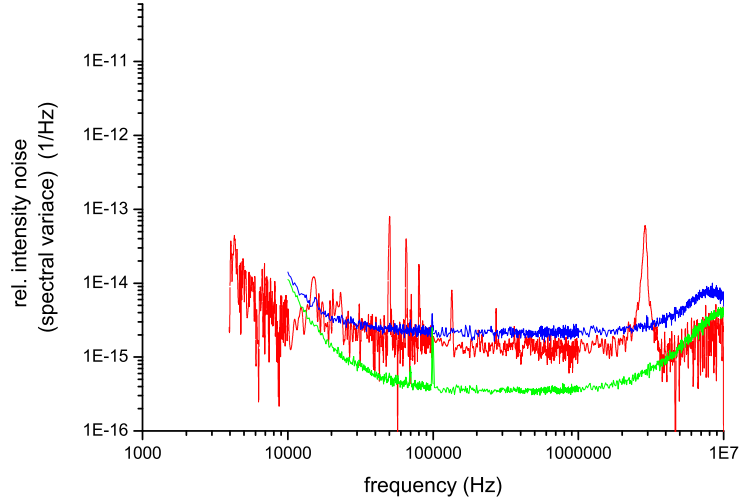
(b)

FIGURE 3.19: (a) Spectral density of the relative intensity noise of our dipole lasers transmitted through the TOF, the spectra for the blue-detuned and red-detuned lasers are labeled by the color of the line. The green line indicates the noise of the amplified photodiode (lasers off). (b) Resulting parametric heating rate as a function of the double oscillation frequency of the individual lasers (red, and blue line) according to Eq. (3.23), and the total heating rate (black line). The grey dashed lines mark twice the radial and axial trapping frequencies.

Resonant heating

The contribution of resonant heating due to position fluctuation of the trap center is obtained analogously to Eq. (3.23) by [109]

$$\langle \dot{E} \rangle = 4\pi^4 m \nu_i^4 S_{\Delta r} (\nu_i) , \tag{3.24}$$

where $S_{\Delta r}$ is the power spectrum of the position fluctuation, i.e., integration of $S_{\Delta r}$ over the frequency space yields the variance of the trap center position

$$\int_0^\infty S_{\Delta r} (\nu) \, \mathrm{d}\nu = \langle \Delta r^2 \rangle . \tag{3.25}$$

Here, a shaking of the trap heats up the atoms independently of their initial energy, but with a strong dependency on the trap frequency due to the factor ν_i^4.

Since variations of the relative powers P_{red} and P_{blue} result in radial displacement of the trap center, fluctuations in the power of each dipole laser give rise to trap position fluctuations in the radial direction. For small power fluctuations ΔP, the variance of the trap position can be approximated

$$\langle \Delta r^2 \rangle \approx \left| \frac{\partial r}{\partial P} \right|^2 \langle \Delta P^2 \rangle , \tag{3.26}$$

such that

$$\int_0^\infty \left| \frac{\partial r}{\partial P} \right|^2 S_P(\nu) \mathrm{d}\nu = \langle \Delta r^2 \rangle . \tag{3.27}$$

For our trap parameters, the calculated power dependency of the trap position yields for both lasers $\partial r / \partial (P/P_0) \approx 2 \times 10^{-7} \mathrm{m}/(P/P_0)$, where P_0 is the power of the respective laser beam. Hence, the measured power noise spectrum $S_P(\nu)$ can be used in order to estimate both the parametric and the resonant heating rate in our two-color dipole trap.

For the measured spectral power densities $S_P(\nu_r)$ at the radial trap frequency $\nu_r = 200$ kHz (see Fig. 3.19), Eq. (3.24) predicts a total resonant heating rate of $\langle \dot{E} \rangle = 0.2$ mK/s in our trap. In this analysis, we find that the (radial) resonant heating rate is expected to be significantly larger than the (radial) parametric heating rate for the initial temperature of 28 μK. This is also reflected in the excitation spectrum obtained from measurement of the trapping frequencies (see Fig. 3.12). However, since the power fluctuations of our dipole lasers are small at the relevant frequencies (see Fig. 3.19), atom losses due to this kind of resonant and parametric heating can be neglected.

Note that vibrations of the fiber itself might also provide resonant heating, since the frequencies of normal modes of vibrations of the nanofiber waist ($\nu_n \approx n \cdot 130$ kHz)
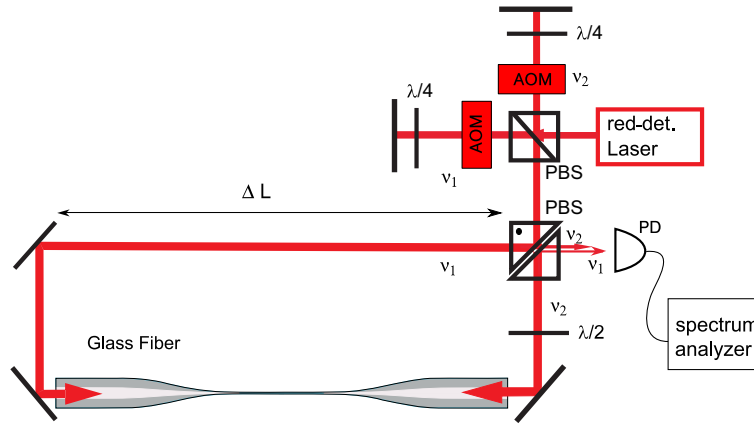
FIGURE 3.20: For the measurement of the phase noise we used the Sagnac inter-
ferometer structure of our setup. The interference of the two beams is detected
using a fast photodiode (PD). The resulting beat signal is recorded by an elec-
tronic spectrum analyzer. Two AOMs with mutual detunings are used for the
heterodyne measurement.

are close to the trapping frequencies. Preliminary measurements of the phase fluctu-
ations on several other TOFs indeed indicate resonances of mechanical oscillations.
However, it is unclear whether excitations of these high frequency oscillations do
occur in our setup. Currently, the measured phase noise spectra in our setup are
dominated by a broad noise floor (above shot noise limit) which does not permit
to resolve resonance features of any mechanical vibrations.

3.5.4   Influence of phase noise

The periodic lattice potential of the nanofiber trap relies on the interference of two
counter-propagating red-detuned laser beams. This interference forms a standing
wave intensity pattern which is strongly dependent on the coherence properties of
the laser light as well as on the phase stability of each of the two counter-propagating
beams.

Typical coherence lengths provided by single-frequency solid state lasers are in the
order of many kilometers. In free space, it is only determined by the laser line
width γ as $L_{\mathrm{coh}} \simeq c/\gamma$. In general, the coherence length is limited by phase noise,
e.g., resulting from spontaneous emission in the gain medium, or noise induced by
electronics when using modulators, e.g., AOMs. If, however, intense laser light is
carried by optical fibers, non-linear effects give rise to phase fluctuations induced by
stimulated Brillouin scattering (SBS). This effect reduces the coherence length and
results in intensity and phase noise due to stochastic fluctuations of the spontaneous
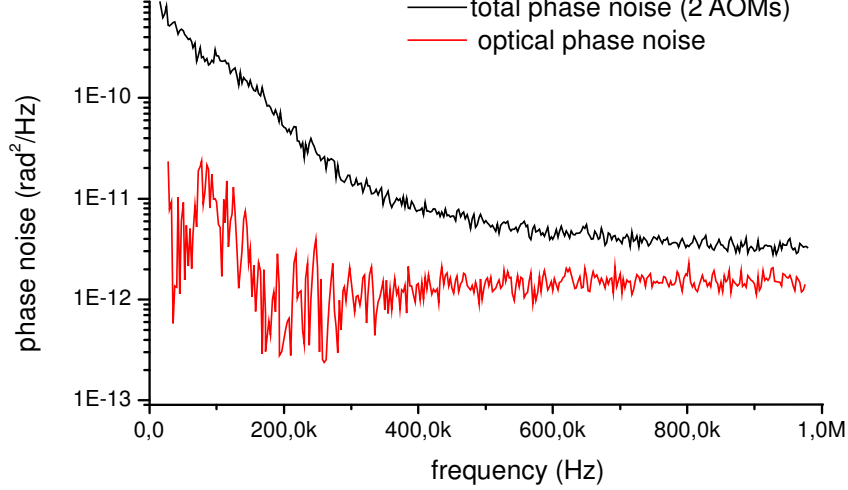scattering processes that initiate SBS [111].

FIGURE 3.21:   Spectral density of the optical phase noise measured with the
setup shown in Fig. 3.20 (red line, no AOM), (black line, 2 AOMs on).

Brillouin scattering

SBS can be substantial in long haul single mode fibers resulting from the interaction
of the transmitted light and thermally generated acoustic waves in the fiber. Above
a certain threshold power, which can be as low as a few milliwatts for narrow
linewidth lasers, the scattered light interferes with the incident light and amplifies
the acoustic waves via electrostriction [112]. This further enforces the scattering
process and results in a large back reflection with a Stokes-shifted frequency (about
20 GHz). However, the necessary threshold power for SBS is $P_{\text{thr}} \approx 21\frac{A_{\text{eff}}}{gL}$ [113],
where $g = 2 \times 10^{-11}$ m/W is the gain coefficient for silica, A_{eff} is the effective fiber
cross section, and L the length of non-linear interaction. For the nanofiber waist the
SBS threshold is thus expected to be about $P_{\text{thr}} \approx 10$ W, hence only spontaneous
Brillouin scattering should occur in this case. Experimentally, we have not observed
any non-linear dependency of the backscattered power due to SBS up to a level of
250 mW of transmitted light through the TOF in vacuum. Only the analysis of
phase fluctuations in our optical setup (see Fig. 3.21) may give rise to spontaneous
Brillouin scattering and to heating due to axial position fluctuation of the trap.

Note that the optical path lengths of the two counter-propagating laser beams are
almost equal in our setup. Thus, common phase noise of the standing wave beams
at the nanofiber is expected to be strongly suppressed. For unequal path lengths,
the intrinsical phase noise of the laser itself should have an effect on the heating
rate and thus on the trap lifetime. However, even for a difference of $\Delta L = 2$ m
in the optical pathways we do not observe any change neither of the phase noise
nor on the trap lifetime. Hence, we can conclude that the contribution of phase
fluctuations produced in the laser cavity and in the optical pathways to heating is
negligible.

Phase noise measurement

For the measurement of the phase noise of the standing wave we employed the Sagnac interferometer structure of our fiber trap setup (see Fig. 3.20). The imperfections of the polarizing beam splitter (PBS) are used to create interference of the two counter propagating laser beams at the output port of the PBS (see Fig. 3.20). In a homodyne detection of the interference (or via heterodyning using two AOMs), using a fast photodiode (PD), we measure a phase dependent intensity signal

$$I(\phi + \Delta\phi) \propto I_0(1 - \cos(\phi + \Delta\phi)). \tag{3.28}$$

Any deviation of the relative phase ϕ of the counter propagating beams by $\Delta\phi$ results in an intensity change at the PD. The resulting PD signal is recorded and processed using an electronic spectrum analyzer (ESA). The highest sensitivity for phase fluctuations in this setup is obtained at the side of the fringe ($\phi = \pi/2$), provided that slow phase drifts are negligible during the measurement. From the determined intensity noise we estimate the phase noise via the relation

$$\Delta\phi = |\partial_\phi I|\Delta I. \tag{3.29}$$

When using two individual AOMs for each of the dipole beams in the setup, we measure a phase noise density of $S(\nu)_{\Delta\phi} \approx 1 \times 10^{-11}$ rad^2/Hz with a mainly flat spectrum from 400 kHz to 1 MHz, at lower frequencies the $1/f$-noise is governed by the electronic noise of the AOM-drivers (see Fig. 3.21). Without any AOMs the phase noise level is reduced to an almost constant level of $S(\nu)_{\Delta\phi} \approx 2.2 \times 10^{-12}$ rad^2/Hz in the region from 200 kHz to 1 MHz, the corresponding phase variation $\Delta\phi_{\mathrm{rms}}$ decreases from 23 mrad to 1.5 mrad (DC to 1 MHz).

These phase fluctuations of are related to axial position fluctuations of the trap center via

$$\Delta z_{\mathrm{rms}} = \Delta\phi_{\mathrm{rms}}/\beta, \tag{3.30}$$

where β is the propagation constant of the red-detuned dipole laser. Hence, phase fluctuations of the standing wave lead mainly to resonant heating in axial direction. For an axial oscillation frequency of $\nu_z = 300$ kHz, Eq. (3.24) predicts a heating rate of $\langle\dot{E}\rangle \approx 68\ U_0$/s $= 27$ mK/s (or 5 mK/s without any AOMs). This value is compatible with the reduced lifetime of $\tau \approx 12$ ms resulting from the additional electronic noise induced by the AOM controllers. Without any AOMs being used, the residual phase noise would yield a heating rate of 5(1) mK/s, which is in a good agreement with the measured loss rate of atoms ($U_0/\tau \approx 8(1)$ mK/s) for $\tau \approx 50$ ms.

Note that we are able to slightly reduce the atomic losses by decreasing the axial trapping frequency, i.e., by lowering of the axial confinement only (cf. Sect. 3.3.5). This behavior would suggest that position fluctuations of the standing wave beams contribute significantly to heating in our trap. The origin of the position fluctuations is assumed to be phase noise due to spontaneous Brillouin scattering inside the

TOF. However, further investigations of this effect need to be carried out in order to clarify the underlying mechanisms and eventually suppress the arising heating.

Results and discussion

The survey of several sources of heating reveals that most of the heating mechanism are negligibly small (see Table 3.2). The only significant contribution, which also seems to be the origin of the reduced trap lifetime, is indicated by phase fluctuations. The underlying mechanism is not yet fully understood and requires further investigations. Nonetheless, we hope that the phase of the trapping fields can be actively stabilized by using an electro-optical phase modulator and employing a fast servo loop. This would reduce heating and increase the storage time of the atoms, and would even allow us to efficiently convey the atoms along the fiber.

We further note that any kind of heating reduces the coherence time of a quantum system, either due to dephasing by thermal motion or, e.g., due to loss of atoms, etc.. However, the timescale on which inevitable photon-scattering of the dipole laser fields leads to decoherence, in our case about 50 ms, is comparable to the trap lifetime. Thus, the coherence time of the atomic ensemble $\tau_{\mathrm{coh}} \approx (\tau_{\mathrm{scatt}}^{-1} + \tau_{\mathrm{loss}}^{-1})^{-1}$, is expected to be reduced to only half of the ultimate value.

Although, heating limits the lifetime of our trap, the effect on the coherence time of the trapped ensemble is assumed to be only marginal (compare with [29]). Hence, our optical interface with trapped atoms holds great potential for coherent manipulation of atomic states with light. It should thus be possible to, e.g., realize electro-magnetically induced transparency (EIT) and slow-light in our system, a first important step towards fiber coupled quantum memories for quantum communication.

Heating effect	Heating rate	Comment
Recoil heating	10 μK/s	fundamental
Dipole force fluctuation	$< 10^{-6}$ μK/s	state dependent
(due to fluorescence)	3 μK/s	and energy dependent
(due to probe light)	(12 μK/ms)	
Laser intensity fluctuation (total)	10 μK/s	parametric, energy dependent
Laser intensity fluctuation (radial)	0.2 mK/s	resonant
Optical phase noise (axial)	5 mK/s	resonant
Phase noise (AOM)	(27 mK/s)	resonant, avoidable
temperature change estimated from atom losses	≈ 8 mK/s, (≈ 33 mK/s)	observed (two AOMs)

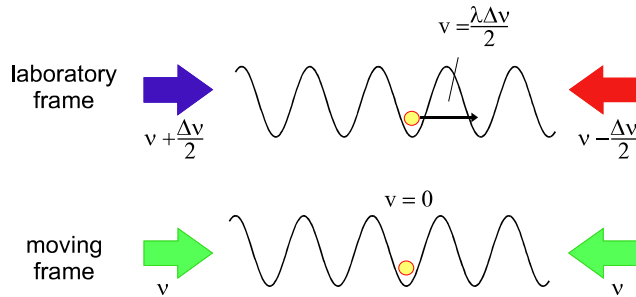TABLE 3.2: List of heating effects and the corresponding heating rates.

FIGURE 3.22: The mutual detuning $\Delta\nu$ of the counter-propagating beams results in a standing wave pattern which moves at a velocity of $v = \lambda/2 \cdot \Delta\nu$. In a co-moving frame this detuning is compensated by the Doppler shift and the interference forms a standing wave at rest.

3.6 Conveying atoms

As a first straightforward application of our nanofiber-based trap, we considered the realization of an optical conveyer belt for atoms. In this section I will report on the first attempts to load and to transport the trapped atoms along the nanofiber.

3.6.1 Moving standing wave

If the axial confinement in an optical dipole trap is provided by a standing wave, the stationary optical lattice can be translated by varying the relative phase of the counter-propagating beams. A constant motion of the lattice can be realized through a mutual detuning of the frequency of the beams such that the interference pattern propagates with a velocity of

$$v = \frac{\lambda\Delta\nu}{2}, \tag{3.31}$$

where $\Delta\nu$ is the frequency difference of the counter-propagating beams (see Fig. 3.22). In a co-moving frame this detuning is canceled by the Doppler shift thereby resulting in a standing wave pattern. For small accelerations the trapped atoms will remain trapped, allowing the atoms to be conveyed along the fiber [114, 115].

The detuning of both lasers can be realized by using acousto-optical modulators (AOMs). However, as discussed in the previous section, the lifetime of the trap critically depends on the relative phase stability of the counter-propagating beams. By employing further active optical elements, such as AOMs, additional phase noise might be introduced, which results in higher heating rates and leads to a rapid loss of atoms. Due to the sensitivity to phase noise, efficient transportation requires an active stabilization of the phase, which at the same time has to allow for tuning of the laser frequencies in order to accelerate the atoms.
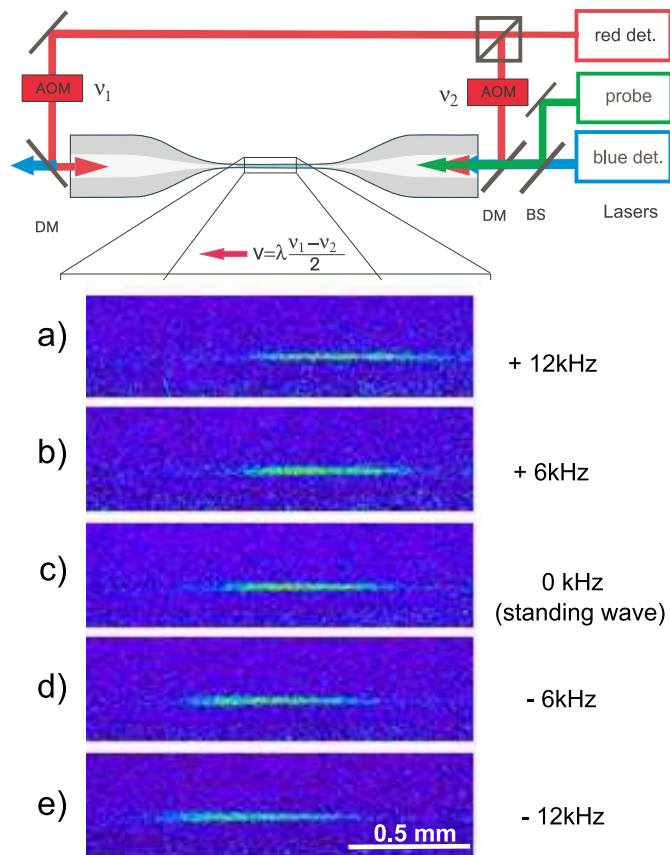
FIGURE 3.23:   Conveying of atoms. The images a)−e) have all been recorded after loading of traveling potentials moving with different velocities $v = \lambda/2 \cdot \Delta\nu$. The respective detunings $\Delta\nu$ of the counter propagating beams are denoted on the right.

3.6.2   Transport of atoms

For a simple proof of principle, we set the difference frequency to a fixed value, and load the atoms into a constantly moving lattice. The frequencies of the two dipole beams are shifted by using two AOMs (see Fig. 3.23). These AOMs are driven by two phase-locked waveform generators (Agilent N9310, and N5182). Since the implemented phase stabilization only has a low bandwidth, the relative phase noise of the two independent waveform generators is unsuppressed at high frequencies and therefore lowers the lifetime of our trap to 12 ms. Nonetheless, we are able to demonstrate transportation of atoms over more than 1 mm in each direction along the nanofiber by loading the atoms into the lattice sites moving at various velocities (see Fig. 3.23). Up to a velocity of 6 mm/s the number of trapped atoms does not significantly change but the distribution is elongated in the direction of the transportation. Higher velocities result in a decrease of the number of transported atoms, presumably because the efficiency of loading the atoms into the moving trapping sites is reduced.

However, in principle the loading might be performed with a stationary lattice and subsequently transported. In this case the transportation efficiency would be primarily limited by the short lifetime of the trap. A more elaborate phase stabilization should, however, allow us to reduce the atom loss during the conveyance, and would permit us to trap the atoms along the whole length of the nanofiber. This would increase the number of trapped atoms by about a factor of up to five, or perhaps more if the nanofiber length is increased.

Another possible application of such a fiber-optical conveyer belt for atoms might be the deterministic coupling of atoms with solid state devices as, e.g., micro resonators [118–120] for cavity-QED experiments, or for experiments involving superconducting circuits (Josephson junctions) [7–9]. In this case, the atoms could be loaded at a distant MOT region and carried to the desired place in the experimental setup. Due to the tight transversal confinement of the trapping fields around the nanofiber, the atoms can be placed in close vicinity of such a device while permitting a minimum of interaction with the trapping fields.

3.7   Imaging of the trapped atoms

3.7.1   Fluorescence imaging

For imaging the trapped atoms, we have positioned a home-built microscope objective with a numerical aperture of 0.29 inside the vacuum chamber [101]. This allows us to collect the fluorescence light, induced by the resonant excitation of the trapped atoms, and thus create an image on the chip of an electron multiplying charge coupled device (EMCCD) camera (Andor, DU897).
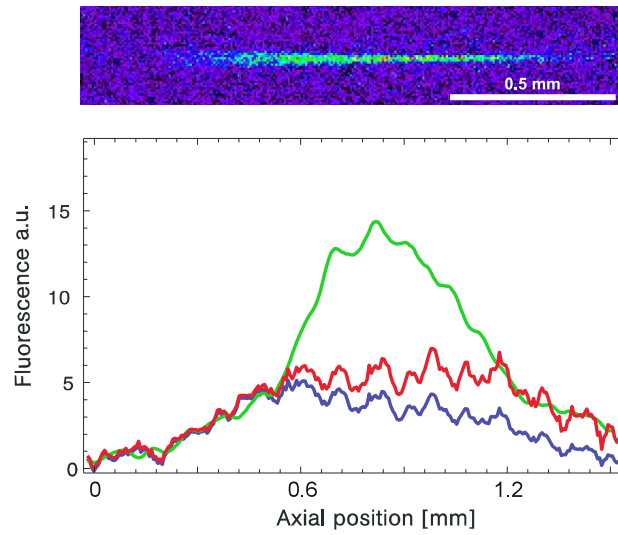
FIGURE 3.24:   (blue curve) Horizontal profile of the fluorescence image of the nanofiber trap (upper image), the excitation light propagates through the fiber from the left to the right. The red curve represents the density distribution of the atoms (see text). Here, the flat central part, indicates maximum filling of the nanofiber trap. As a reference the fluorescence of the MOT-cloud has been imaged before loading the trap (green curve) and the scaling has been adjusted arbitrarily in order to compare the shapes of the curves.

For all recorded images the probe laser was detuned by $\Delta = -20$ MHz with respect to the AC-Stark shifted D2 ($F = 4 \to F' = 5$) transition of cesium and its power was set to 500 pW, corresponding to twice the saturation intensity at resonance at the position of the atoms. Such a large detuning was chosen in order to ensure low attenuation of the probe light along the nanofiber, thereby making all atoms of the ensemble contributing to fluoresce with similar intensities. The probe light was pulsed with a pulse length of 2 ms, corresponding to the exposure time of the EMCCD camera. The power chosen for the probe light ensures low heating and negligible losses of atoms during the exposure time. The axis of polarization was aligned perpendicular to the camera view direction in order to maximize the perceived intensity on the camera chip. All fluorescence images shown in this thesis were recorded 20 ms after loading the nanofiber trap. This delay time is sufficient for the atoms to escape from the MOT, thus shielding of the fluorescence light by the surrounding atom cloud can be neglected. Each shown image is the sum of 320 single background corrected exposures from consecutive experimental runs.

The image in Fig. 3.24 shows the fluorescence of a trapped ensemble of about 2000 cesium atoms over a length of $L \approx 1.2$ mm corresponding roughly to the $1/e^2$-diameter of the cold atom cloud in the MOT. Here, the fluorescence intensity is proportional to the number density of atoms $\rho(z)$ times the probe light intensity $I_{\mathrm{probe}}(z)$, i.e.,

$$I_{\mathrm{fluor.}}(z) \propto \rho(z) I_{\mathrm{probe}}(z)$$

$$\propto \rho(z) I_0 \exp(-\sigma \int_0^z \rho(z') dz'), \tag{3.32}$$

where the exponential function accounts for the intensity loss due to absorption along the nanofiber. The intensity profile of the image (Fig. 3.24, blue curve) can thus be used to estimate the density distribution $\rho(z)$ of the trapped atoms along the nanofiber (z-direction). Given that the attenuation of the probe light varies slowly along z, we can simply approximate $I_{\mathrm{probe}}(z) \simeq I_0 \exp(-OD/L \cdot z)$, where OD is the measured optical density of the atomic sample ($OD \approx 1$ for $\Delta = -20$ MHz).

In Fig. 3.24 the resulting density profile of the trapped atomic ensemble (red curve) is compared to the profile of the atom cloud in the MOT (green curve). As expected, the density distributions are consistent in the low density region of the MOT. In the central part of the MOT, however, the density distribution becomes flat. This behavior can be explained by assuming that the maximum filling of the nanofiber trap is limited by the collisional blockade effect [97]. If we assume loading of at most one atom per lattice site and a filling factor of 0.5 (cf. [97]) for each of the two lattices above and below the nanofiber, then from the measured density distribution $\rho(z)$ in Fig. 3.24 we obtain the number of trapped atoms $N = 2 \times \sum_{i=0}^{L/\Delta z} \rho(z_i) \Delta z \approx 2100$, where $\Delta z = z_i - z_{i-1} \approx 500$ nm is the lattice spacing. The resulting atom number of 2100 is in good agreement with our absorption measurement performed under strong saturation ($N \approx 2000$) as described in Sect. 3.3.2.

3.7.2 Coherent scattering

For the imaging of the trapped atoms relatively high intense excitation pulses (500 pW) have been used in order to obtain reasonable counting rates on the EM-CCD chip. About 60% of the input light power was absorbed by the trapped atoms (300 pW) and presumably re-emitted into free space. Interestingly, our camera collected only a tiny fraction of about 1/250 of the power expected under the assumption of isotropic scattering (1 pW), taking the NA of the objective, the transmission of the filters, the chip sensitivity and quantum efficiency, the EM gain, and the timing of the camera into account.

This result would suggest that the fluorescence of the trapped atomic ensemble displays coherences of the re-emitted light, such that the radiation interferes in a directed pattern and thus lowers the intensity in the observed solid angle. This assumption is further confirmed when regarding the optical Bloch equations of a driven two-level atom subjected to coherent incident light: The coherent fraction of the scattered intensity is unity in the limit of weak coupling ($\Omega \to 0$) (or large detuning ($\Delta \gg \Gamma$)) [122]

$$\frac{\bar{I}^{\text{coherent}}_{\text{scat.}}}{\bar{I}_{\text{scat.}}} = \frac{1 + 4\Delta^2/\Gamma^2}{1 + 4\Delta^2/\Gamma^2 + 2(\Omega^2/\Gamma^2)}, \tag{3.33}$$

where Γ is the atomic decay rate and $\Omega = d_{eg} \cdot \mathcal{E}/\hbar$ is the Rabi frequency which quantifies the interaction strength. In our case, this fraction is expected to be about 97%, for an off-resonant saturation parameter of $s \equiv 2(\Omega^2/\Gamma^2) \approx 2$, estimated from the previously mentioned intensity and detuning of the probe field. Thus, in this regime the atoms are expected to radiate almost fully coherently[1], like classical dipoles, with a well defined phase with respect to the excitation field.

The radiation characteristic of such a coherently radiating array of emitters is related to *phased arrays* in wave theory, which is also the basic principle of directed antennas. Here, the relative phases of the periodically spaced emitters are aligned in such a way that the radiation pattern resulting from interference, reinforces radiation in the desired direction and suppresses it in all other directions [121].

In our case, the atoms are trapped in two one-dimensional arrays with a constant lattice spacing of $\Delta z \approx 500$ nm (and a filling factor of 0.5). The excitation via the fiber guided light imprints a position-dependent phase relation ($\phi(z) = \beta z$, see Sect. 1.1) between the atoms, such that the subsequent coherent re-emission into free space results in a well-defined angular distribution analogous to Bragg scattering

$$\cos(\theta_{\text{max}}) = \frac{2\pi - \beta_{\text{probe}}\Delta z}{k_{\text{probe}}\Delta z}, \tag{3.34}$$

---

[1]Note that for Zeeman-degenerate transitions spontaneous Raman scattering may increase the incoherent fraction (up to 30% for Cs [123]). Furthermore, for the case of a large coupled atomic ensemble the total scattering rate might also be changed [116, 117].
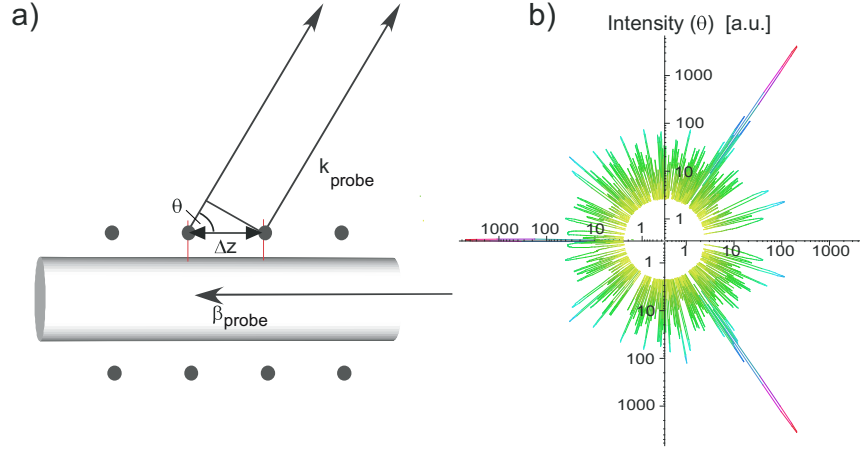
FIGURE 3.25: (a) Bragg-scattering of the fiber guided probe light due to a periodic arrangement of trapped atoms. (b) Polar plot of the angular intensity distribution, simulated for a random filling of 100 atoms in the array (filling factor of 0.5). Note that the intensity has been scaled logarithmically.

where β_{probe} is the propagation constant of the fiber-guided mode of the probe light and k_{probe} is the corresponding wave vector in vacuum. For an infinitely long and perfectly periodic lattice this would result in a sharply defined scattering cone with an opening angle of $2\theta_{\mathrm{max}} = 2 \times 56°$ for the probe light at a wavelength of 852 nm (see Fig. 3.25(a)).

Due to a random filling of the optical lattice, however, this pattern is expected to be blurred such that a small part of the coherent radiation is scattered into other directions. The random distribution of defects in such a lattice would result in a spatial fluctuation of the electric field amplitude $\Delta\mathcal{E} \propto \sqrt{N_{\mathrm{voids}}}$, such that the intensity of isotropically scattered light would be proportional to the number of voids in the lattice ($I_{\mathrm{iso}} \propto N_{\mathrm{voids}}$). In contrast to this, the intensity at the maxima of the angular distribution is expected to scale quadratically with the number of atoms located in the lattice ($I(\theta_{\mathrm{max}}) \propto N_{\mathrm{atoms}}^2$).

Figure 3.25(b) shows a simulated intensity distribution arising from scattering of such arbitrarily filled lattice sites with 100 atoms and a filling factor of 0.5. The resulting pattern indicates preferred scattering at $\theta = \pm 56°$ with additional isotropic emission, whose intensity is proportional to the number of voids in the lattice. In our experiment we should be able to observe the scattered power of about half of the 2000 trapped atoms, but the currently measured power corresponds to only 8 atoms. This result may indicate that the radiation characteristic of the fiber-coupled ensemble is altered either due to an unexpected even distribution of atoms inside the lattice, or probably due to collective radiative effects [117].

The investigation of the scattering under the preferred angle might may help to clarify this circumstance. However, our setup does not provide full optical access to all angles and we were not able to resolve this pattern of coherent radiation. We are planning to employ a tunable laser to change the spacing in our optical lattice via its wavelength, thereby shift the angle of preferred emission into the range of optical access.

It is worth noting that one special feature might occur in the case of coherent scattering by atoms arranged in a lattice with spacings $\Delta z < 2\pi/(\beta_{\mathrm{probe}} + k_{\mathrm{probe}})$: In the classical picture, any emitted radiation interferes destructively in all directions in vacuum if the atoms are closely spaced and coherently excited with a slightly smaller wavelength than the wavelength in vacuum. As a consequence, deexcitation of the atoms due to emission into free space will be inhibited. The only remaining decay channel is the nanofiber. By choosing reasonably large trap distances from the surface the channeling of radiation into the fiber might be strongly suppressed [130]. Hence, the lifetime of the excited atomic states could be substantially increased. More elaborate calculations by H. Ritsch et al. [117] have shown that in this case the system may give rise to metastable *excitons* which propagate in the lattice without showing a radiative decay.

Chapter 4

Interfacing light and atoms

The key challenge in implementation of practical quantum information technologies as, e.g., quantum-networks is a faithful mapping of photonic and atomic quantum states [124]. For this purpose, efficient transfer of quantum states between photons and atoms might be established by interfacing light and atoms under a strong light-atom interaction.

As an alternative to the single-atom approach using a high-finesse cavity in the strong-coupling regime, an ensemble of atoms can provide a similar strong atom-light coupling without a cavity. This approach involves less complexity and provides a better accessibility to the atoms compared to cavity-QED experiments. Here, the interaction with a collective mode of the ensemble can be collectively enhanced due to many-atom constructive interference [23]. As shown in [23, 124] the "effective" figure-of-merit for the light-atom ensemble interface is given by the resonant optical density (OD). In this chapter we analyze the coupling of fiber-guided light and the trapped atomic ensemble in our experiment, and motivate further developments towards direct integration of laser-cooled atomic ensembles within fiber-networks.

Moreover, this chapter presents three powerful approaches to interface trapped atoms and fiber-guided light. In the first part the resonant interaction of the trapped atomic ensemble and the fiber-guided light is outlined. Furthermore, the spectroscopic properties of the trapped atoms are investigated and the influences of the ac-Stark shifts and inhomogeneous broadening are discussed.

The second part reports on the observation of fluorescence via the coupling of light and the guided modes of the nanofiber.

The last part is focused on a non-destructive phase measurement scheme based on off-resonant light-atom interaction.

4.1   Resonant interaction

All the schemes of detection of the trapped atomic ensemble described so far in this thesis rely on the (near) resonant scattering of light.

The fiber-guided probe light, tuned (close) to the D2 transition of cesium, couples to the atoms via the evanescent field and gets scattered by the atoms. The response of the atoms to the near resonant light results in absorption and dispersion of the probe light, which in turn is perceivable at the output of the fiber. Here, the presence of a large trapped atomic ensemble results in a strong extinction of the fiber-guided probe light.

The presented detection scheme takes advantage of the resonant enhancement of the optical response in conjunction with an efficient coupling of the atoms to the fiber-guided light. The capacity to establish strong coupling between a photon and a collective mode of the ensemble makes the presented technique ideally suited for interfacing photonic and atomic quantum systems.

Method

An important quantity characterizing the probability for absorption and scattering of photons by atoms is the cross section which can be understood as the effective area of the atom occluding the incident light beam. In this regard, the efficiency for coupling fiber-guided light and the atom (or the OD per atom) is given by

$$\eta = \sigma/A_{\text{eff}} \left(= \frac{\text{OD}}{N} \right),\tag{4.1}$$

where σ is the absorption cross section of the atom which incorporates the dependency on the atomic state as well as on the driven transition, and $A_{\text{eff}} = P/I(\mathbf{r}_{\text{at}})$ represents the effective mode area of the fiber-guided mode [36, 126] (i.e., ratio of the total power P and the intensity of the evanescent field $I(\mathbf{r}_{\text{at}})$), where $\mathbf{r}_{\text{at}}$ denotes the position of the atom. When the distance between the atom and the fiber surface is small, the light-atom coupling is enhanced by the strong lateral confinement of the field around the nanofiber, making A_{eff} comparable to σ [15].

The absorption cross section owing to a dipole transition $|nFM_F\rangle \rightarrow |n'F'M'_{F'}\rangle$ is related to the atomic transition dipole moment

$$d_{nFM,n'F'M'} = \langle nFM_F|\mathbf{e} \cdot \mathbf{d}|n'F'M'_{F'}\rangle\tag{4.2}$$

and may be expressed by [126]

$$\sigma = \frac{\omega_0}{2c\epsilon_0\Gamma_0\hbar}|d_{nFM,n'F'M'}|^2 \frac{1}{1 + 4\Delta^2/\Gamma_0^2 + s},\tag{4.3}$$

where $\mathbf{e}$ represents the polarization vector of the probe light, $\mathbf{d}$ denotes the dipole operator, $\Delta = \omega - \omega_0$ is the detuning of the probe light from the (light-shifted)

angular transition frequency ω_0, Γ_0 is the decay rate of the excited state, s denotes the saturation parameter ($s = I/I_{\text{sat}}$), and ϵ_0 is the vacuum permittivity. Here and in the following we use the same nomenclature for the matrix elements and the quantum numbers as in Sect. 2.2.

In the spherical basis, the absorption cross section for each polarization component of the probe light (denoted by q) reads

$$\sigma = \frac{\omega_0 |\langle nF\|\mathbf{d}\|n'F'\rangle|^2}{2c\epsilon_0\Gamma_0\hbar} \begin{pmatrix} F' & 1 & F \\ M'_{F'} & q & -M_F \end{pmatrix}^2 \frac{1}{1 + 4\Delta^2/\Gamma_0^2 + s}, \qquad (4.4)$$

where

$$|\langle nF\|\mathbf{d}\|n'F'\rangle|^2 = (2F+1)(2F'+1) \begin{Bmatrix} J & J' & 1 \\ F' & F & I \end{Bmatrix}^2 |\langle nJ\|\mathbf{d}\|n'J'\rangle|^2. \qquad (4.5)$$

In the upper notation $q = \pm 1$ denotes $\sigma^{\pm}$-polarization, and $q = 0$ corresponds to π-polarization. We note that the 3-j symbol in Eq. (4.4) specifies the selection rules $F' - F = 0, \pm 1$ and $M'_{F'} - M_F = q$. For the atomic states $|nFM_F\rangle$, defined with respect to the quantization axis parallel to the dominating electric field in the trap, i.e., $\mathcal{E}_{\text{red}}$, we assume negligible mixing of the excited state M'_F sub-levels due to ac-Stark shifts (see Sect. 2.2).

The relevant parameters for the D2 transition of cesium ($6S_{1/2} \rightarrow 6P_{3/2}$) are: $\langle 6S_{1/2}\|\mathbf{d}\|6P_{3/2}\rangle = 3.8 \times 10^{-29}\text{C} \cdot \text{m}$, $\omega_0 = 2\pi \cdot 351.7$ THz, and $\Gamma_0 = 5.2$ MHz [49]. Note that for the closed sub-transitions $|F = 4, M = \pm 4\rangle \leftrightarrow |F = 5, M = \pm 5\rangle$, the resonant absorption cross section in Eq. 4.4 becomes maximal with $\sigma = 6\pi c^2/\omega_0^2$, which is equal to the cross section predicted by the Lorentz model [49].

For probing the atoms, we employ the quasi-linearly polarized HE_{11} mode as a probe field. If the polarization axis is aligned orthogonal to the axis containing the atoms (y-polarization, cf. Fig 4.2(d)), the local polarization of the probe field is purely linear and tangential to the fiber surface (yielding $A_{\text{eff}}(r_{\text{at}}) = 1 \times 10^{-11}\text{m}^2$, see Sect. 1.3.2). In the orthogonal orientation of the polarization axis (x-polarization), however, $\mathbf{e}_{\text{probe}}$ is aligned normal to the fiber surface, i.e., the intensity of the evanescent field becomes maximal at the position of the atoms ($A_{\text{eff}}(r_{\text{at}}) = 3.5 \times 10^{-12}\text{m}^2$), but in turn the polarization becomes elliptical (see Sect. 1.3.2). The polarization orientation in the first case leads to the excitation of σ-transitions (i.e., $M'_{F'} - M_F = \pm 1$-transitions are driven simultaneously, with the quantization axis aligned along $\mathcal{E}_{\text{red}}$ (x-direction)), while in the latter case mixed π- and $\sigma^{\pm}$-transitions (i.e., $M'_{F'} - M_F = 0$ and $M'_{F'} - M_F = \pm 1$) can be excited.

In our experiment the initial state of the atomic ensemble is assumed to be an incoherent mixture of all Zeeman sub-states $|F = 4, M_F\rangle$ resulting from the spatially varying polarization and optical pumping in the MOT. The resonant cross section
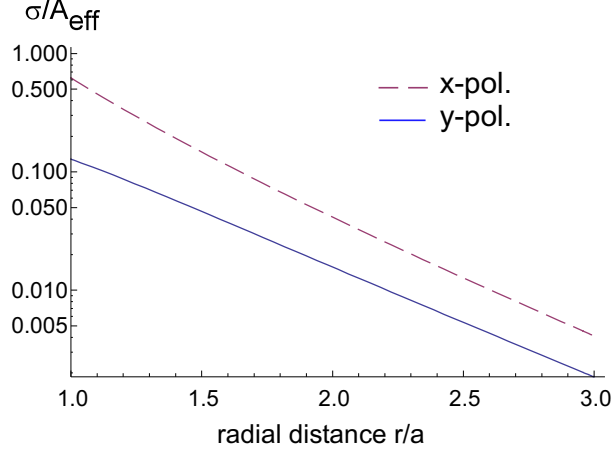
FIGURE 4.1: Resonant coupling efficiency of unperturbed cesium atoms σ/A_{eff} to the evanescent light field as a function of the normalized radial distance r/a, calculated for a fiber radius of $a = 250$ nm and a wavelength of 852 nm (D2 transition, $|F = 4\rangle \rightarrow |F' = 5\rangle$). The atomic population is assumed to be equally distributed among the M_F-states. The dashed and the solid line correspond to the x-polarization and the y-polarization of the probe field, respectively, where the x-axis aligned parallel to the axis containing the atoms while the y-axis is aligned perpendicular to it. Note that the ordinate has been scaled logarithmically.

($\Delta = 0$) according to Eq. (4.4) for unperturbed cesium atoms and an even population of all M_F sublevels yields $\sigma = 1.4 \times 10^{-13} \text{m}^2$, which is found to be independent of the polarization of the probe light.

For both polarization orientations the radial dependence of σ/A_{eff} for evenly populated M_F-states, are plotted in Fig. 4.1. These plots represent the position dependency of the atom-light coupling in absence of the trapping fields.

Note that due to the $M'_{F'}$ dependent light-shift of the $|6P_{3/2}F'M'_{F'}\rangle$ excited state of the trapped cesium atoms (see Sect. 2.2), the absorption line of each sub-transition is shifted differently. The multitude of unequally shifted sub-transitions results in inhomogeneous broadening of the absorption spectrum and simultaneously leads to a decrease of the maximal absorbance per atom and the OD for the D2 transition in cesium. From the maximal values of the absorption cross section σ in the presence of the trapping fields, calculated for the parameters of our trap, we obtain the reduced absorption cross sections $\sigma'_y = 0.35\sigma$ and $\sigma'_x = 0.5\sigma$, respectively. Meaning that at the position of the atoms ($r_{\text{at}} = 230$ nm) each atom would absorb a fraction of $\eta_y = 0.35 \times 1.4$ % and $\eta_x = 0.5 \times 4$ %, respectively, when taking the inhomogeneous broadening into account.
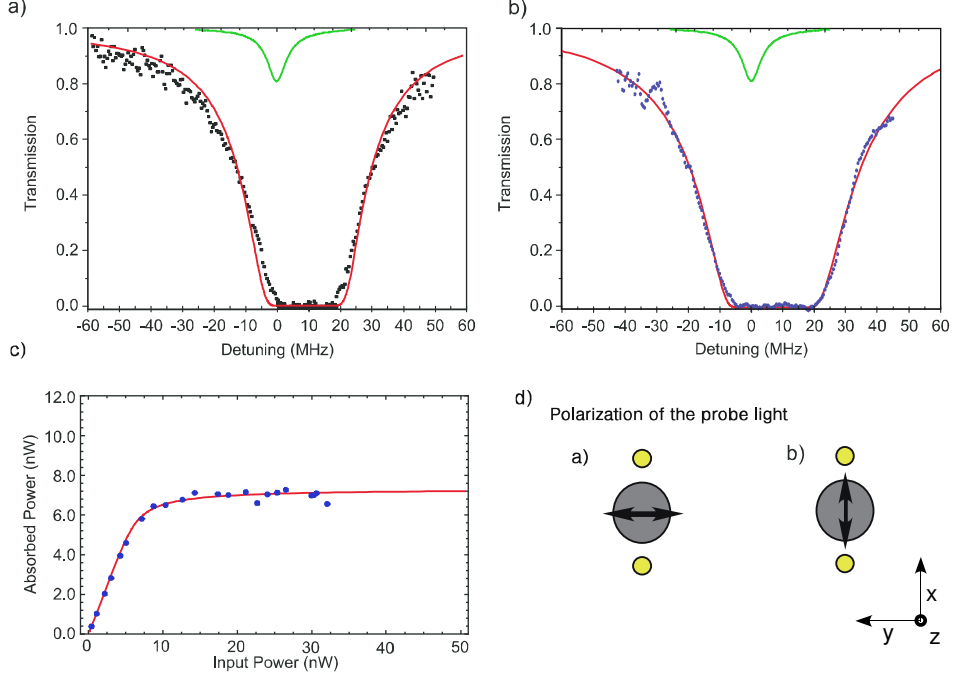
FIGURE 4.2: (a) Transmission spectrum of the probe beam through the nanofiber after loading the trap (black squares) for orthogonal, and (b) parallel polarization (blue points). As a reference, we plotted the spectrum of the MOT-cloud in each case (green line). The red lines are theoretical fits, see text. (c) Saturation measurement (blue circles) yielding the number of trapped atoms (see Sect. 3.3.2). (d) Polarizations of the probe light with respect to the atoms used for the measurements in (a) and (b).

4.1.1 Spectroscopy

In order to investigate the spectral properties of the trapped atomic ensemble and to estimate the effect of inhomogeneous broadening we performed measurements of the transmission/absorption of the probe light as a function of its detuning.

The measured transmission is calculated according to

$$T = \frac{(P_{\mathrm{at}} - P_{\mathrm{bg}})}{(P_0 - P_{\mathrm{bg}})}, \tag{4.6}$$

where P_{at}, P_0, and P_{bg} are the APD signals with atoms, without atoms, and without probe light, respectively.

For the spectroscopic measurements presented in Fig. 4.2 (a & b) the probe light power was chosen as about 1 pW. Such a low power ensures that the scattering rate of the atoms (30 kHz) is smaller than their oscillation frequency in the trap ($\approx$ 140 kHz), resulting in strongly suppressed recoil heating due to off-resonant

raman scattering [127]. This maximizes the number of scattered photons before atom loss, thereby optimizing the signal. The APD signal is recorded with a digital storage oscilloscope and averaged over 64 traces. As a reference, the green line in Fig. 4.2 (a & b) shows the transmission of the probe light versus the detuning with respect to the D2 ($F = 4 \rightarrow F' = 5$) transition of cesium without the fiber trap after abruptly switching off the MOT lasers and magnetic field. In this case, the measured absorption due to the cold atom cloud around the nanofiber reaches 20% and the linewidth is only slightly larger than the natural linewidth of cesium due to the atom-surface interactions [15].

The black squares in Fig. 4.2 (a) show the transmission of the probe light polarized along the y-axis (σ-polarization) directly after loading the fiber trap. We observe a strong absorption resulting from a strong increase of the number of atoms in the evanescent field due to trapping of atoms inside the two-color dipole trap. The fitted line profile (solid red line) yields a maximum optical depth of OD = 13(2) at a detuning of 13 MHz and a FWHM of $\Gamma = 20$ MHz. The spectrum for π-polarization, i.e., parallel to $\mathcal{E}_{\mathrm{red}}$ (x-direction), shows an even higher fitted optical depth of OD = 32(2) at a detuning of 12 MHz and a FWHM of $\Gamma = 13$ MHz (see Fig. 4.2 (b)). The shift and broadening can be attributed to the state dependent light-shift of the transition frequency induced by the trapping laser fields (see Sect. 2.2). Compared to this inhomogeneous broadening due to the various shifts of the excited sub-states, the broadening due to the thermal motion of the atoms inside the trapping potential is expected to be negligible (about 0.8 MHz for $T = 28$ μK).

The transmission spectra in Figs. 4.2 (a & b) are well described by

$$T(\Delta) = \exp\left\{-\text{OD} \sum_{i,j} \frac{|d_{i,j}|_q^2 g_{i,j} f_i}{1 + 4(\Delta_j/\Gamma_0)^2}\right\}, \qquad (4.7)$$

(solid red line), where the exponent accounts for the Lorentzian line profiles corresponding to the transitions between the differently light-shifted new eigenstates, $\Delta = \omega - \omega_0$ is the detuning of the probe laser frequency with respect to the atomic resonance frequency in free space ω_0, and $\Delta_j = \Delta - \Delta_j^{\mathrm{LS}}$, where Δ_j^{LS} is the state dependent light shift induced by the linearly polarized trapping lasers. For convenience we denote the ground state $|FM_F\rangle$ by i and the excited state $|F'M_F'\rangle$ by j. $\Gamma_0 = 5.2$ MHz is the natural linewidth of the cesium D2 transition. The coefficients $g_{i,j}$ account for the degeneracy, f_i for the population, and $|d_{i,j}|_q^2$ for the relative strength of the transitions (see Eq. (4.3)). They are chosen such that the sum in the exponent is normalized to one. We assume equally distributed population of the ground state, i.e., $f_i = $ constant. The optical pumping induced by the probe light as well as collective radiative effects are not included in this model and might account for the slight discrepancy between the theoretical prediction and the experimental data.
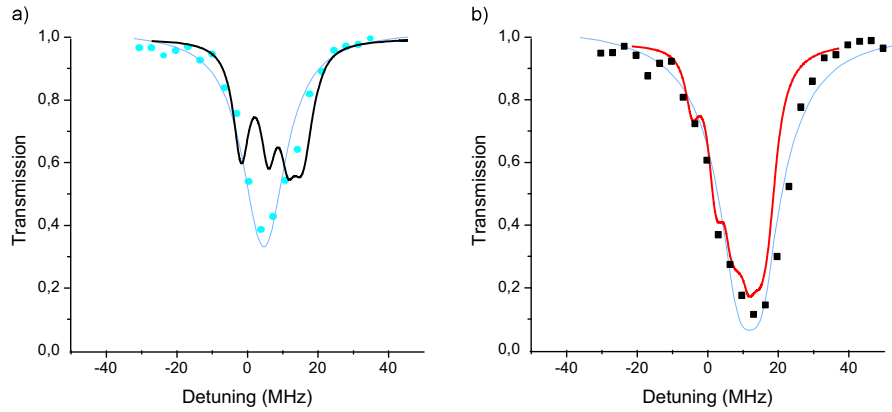
FIGURE 4.3: Transmission spectra for an atom number of about 100. The polarization of the probe light in (a) is chosen orthogonal to the axis containing the atoms (y-polarization), and in (b) parallel to it (x-polarization). The blue dots and black squares indicate the respective measured spectra. As a reference the respective theoretical spectrum for an even $|M_F\rangle$ population is indicated by a thick solid line. The light blue lines are fitted Lorentzian profiles to the optical depth OD(Δ).

The theoretical transmission spectra according to Eq. (4.7) corresponding to the two orientations of the probe light (x- and y-polarization) are depicted in Fig. 4.2 (and Fig. 4.3 for low atom numbers). From the fitted optical depth and the number of atoms, shown in Fig. 4.2, we infer an absorbance per atom of $\eta_y \approx 0.6(1)$ % and $\eta_x \approx 1.6(1)$ %. These values are consistent with our expectation that each of the trapped atoms at a radial distance of about $r_{\mathrm{at}} = 230$ nm from the fiber surface would absorb a fraction of $\sigma'_y/A_{\mathrm{eff}}(r_{\mathrm{at}})_y = 0.5$ % and $\sigma'_x/A_{\mathrm{eff}}(r_{\mathrm{at}})_x = 2$ %, respectively (see above).

4.1.2   Optical pumping

For small numbers of atoms in the trap we are able to resolve the absorbance profiles, which, in contrast to the expected spectra, are reasonable well described by Lorentzian line shapes with a FWHM of approximately 13 MHz and 11 MHz for σ- and π-polarized probe light, respectively (see Fig. 4.3). The low atom number is obtained by reducing the partial pressure of cesium in our MOT-chamber. For this measurement we apply probe pulses with a duration of 0.5 ms and a power of about 1 pW, such that each atom scatters only up to 15 photons. In order to minimize the contribution of heating to the spectrum, each data point corresponding to one specific detuning is recorded in an individual experimental run.

Despite the fact that the measured spectrum for x-polarization almost resembles the theoretical prediction for an evenly distributed M_F-state population (see

Fig. 4.3 (b)), the spectrum for y-polarization (blue circles) shows significant deviations from the expected spectral shape calculated for the same population (black line in Fig. 4.3 (a)). The narrow and less complex structure might be an indication of a redistribution of the $|M_F\rangle$ state population caused by optical pumping.

In particular, the small detuning of the light-shifted resonance, i.e., the position of the transmission minimum (blue circles in Fig. 4.3 (a)), indicate an increased admixture of the $|F = 4, M_F\rangle \rightarrow |F = 5, M'_{F'}\rangle$ transitions to the excited state sub-levels with a large $|M'_F|$ number (see Sect. 2.2). Such a spectrum would suggest that resonant scattering of the probe light may give rise to optical pumping of the ground state sub-level population towards the stretched state $|M_F = \pm 4\rangle$, as is expected for cesium vapor under illumination with σ-polarized resonant light [49]. As discussed previously, in the case of polarization axis being aligned parallel to the axis containing the atoms the probe field excites π- and $\sigma^{\pm}$-transitions simultaneously, such that optical pumping (out of an even M_F population) might be inhibited. Note that pumping by the MOT cooling light during loading of the trap is unlikely because the measured spectra of the x- and the y-polarization do not exhibit the same M_F population.

For the y-polarized probe light (σ-polarization) the effect of optical pumping by the probe light would ultimately lead to a narrowing of the absorption spectrum, which should eventually converge to a Lorentzian profile with a close to natural linewidth, after a sufficient number of scattering events [49,128]. However, in the experiment, this spectral evolution could not be enforced by applying a pump pulse prior to probing. We suspect that heating due to resonant scattering may counteract the narrowing effect and may even lead to broadening of the absorption spectra. A further possibility is that, collective electronic excitations change the damping rate of the atomic transitions [116], thereby leading to homogeneous broadening of the probed transition.

Discussion and Outlook

When taking optical pumping into account and assuming the same spectral shapes for both high and low atom numbers, we would expect an approximately 2 times larger OD for y-polarization and 1.25 times larger OD for x-polarization than that estimated for an evenly distributed M_F-population. With regard to our attempts of increasing the OD, optical pumping and state preparation are still under further investigation. For future experiments, preparation of well defined Zeeman state population may be an important consideration for reducing the influence of inhomogeneous broadening of the probing transition and thus for increasing the coupling efficiency. As an example, pumping into the stretched state $|M_F = \pm 4\rangle$ or the clock state $|M_F = 0\rangle$ may even raise the absorbance per atom to $\eta_y = 4.5$ % and $\eta_x = 8$ %, resulting in an OD of 90 and 160, respectively, for 2000 atoms.
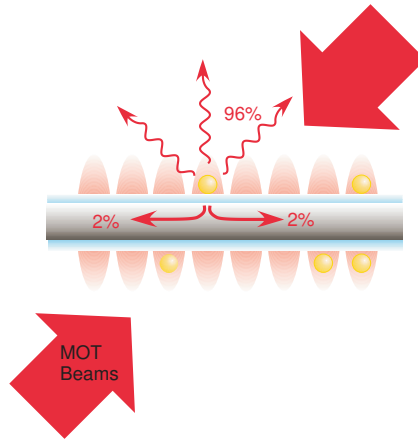
FIGURE 4.4: Scheme for excitation of the trapped atoms. The atoms are illuminated by an optical molasses provided by the MOT beams. At the position of the atoms about two percent of the irradiated power is channeled in each direction of the fiber.

4.2   Fluorescence of the atomic ensemble

In close proximity to the nanofiber surface, the fluorescence light emitted by the trapped atoms can be efficiently coupled into the fiber-guided optical mode [39,130]. Due to the strong transverse confinement of the fiber-guided optical mode and the highly pronounced evanescent field, the probability to emit photons into a nanofiber becomes substantial for distances approaching the fiber surface.

This particular property provides an alternative for effective detection of the trapped atoms, and interrogation of the atomic states. Moreover, it has been shown theoretically that the emission of photons from a linear array of atoms into the guided modes of a nanofiber can be even collectively enhanced, thereby reaching a coupling efficiency close to unity [129].

For the estimation of the efficiency for the atom to emit into the nanofiber, a fluorescence measurement has been accomplished by illumination of the trapped ensemble by the six counter propagating MOT-cooling beams (see Fig. 4.4) and detection of the fiber-coupled fluorescent light on one or both ends of the TOF. This approach of excitation has the advantage that expulsion of the atoms from the trap due to rapid resonant scattering can be diminished, since the photons are incident from all directions [51]. Moreover, we found that for carefully chosen detunings and intensities of the cooling light the atoms get additionally laser-cooled while they are interrogated via the optical molasses, thereby leading to an increased trap lifetime.

Emission rate into the guided modes

The theoretical description of the coupling of fluorescent light to the fiber modes has been extensively reviewed in [130]. We have employed these results to estimate the expected coupling efficiency using the expression of the relative emission rate of atoms in the vicinity of a nanofiber

$$\eta_{\text{fluo.}}(r) \simeq \frac{\gamma_{\text{guided}}(r)}{\gamma_0}, \tag{4.8}$$

where $\gamma_{\text{guided}}(r)$ denotes position dependent spontaneous emission rate into the guided mode

$$\gamma_{\text{guided}}(r) \simeq \gamma_0 \gamma_a \frac{I(r)}{I(a)}, \tag{4.9}$$

γ_0 is the spontaneous emission rate of an atom in free space, and γ_a is the normalized decay rate $\gamma_{\text{guided}}(a)/\gamma_0$ at the fiber surface ($r = a$), and $I(r)$ is the intensity distribution of the guided mode. According to this model, the coupling efficiency into the guided modes follows the radial field distribution outside the nanofiber, i.e, $\eta_{\text{fluo.}}(r) \propto I(r)$, as is the case for the atom-light coupling in absorption with $\eta_{\text{abs}}(r) = \sigma I(r)/P_{\text{probe}}$ (see Sect. 4.1).

For a fiber radius of $a = 250$ nm and a transition wavelength of $\lambda = 852$ nm (D2 line) in conjunction with evenly populated atomic M_F sub-levels Ref. [130] predicts $\gamma_a \approx 0.28$, thus Eq. (4.8) yields $\eta_{\text{fluo.}}(r_{\text{at}}) = 2.7\%$ at a radial distance of $r_{\text{at}} = 230$ nm from the fiber surface. Meaning that in our experiment 2.7% of the fluorescence light is expected to be emitted into the TOF to both sides. In comparison to that, the resonant absorbance per atom η_{abs} of the fiber-guided probe light (isotropic polarization) would yield $\eta_{\text{abs}}(r_{\text{at}}) = 2.7\%$ as well in absence of inhomogeneous broadening due to the ac-Stark shift. However, in contrast to the absorption measurements, the coupling efficiency of fluorescence light is expected not to be influenced by ac-Stark shifts and inhomogeneous broadening.

Experimental realization

The trapped atoms are excited via the MOT-beams and the fluorescence light coupled to the nanofiber is detected at the output of the TOF using an APD. The fluorescence signal, recorded during the last seconds of the experimental sequence, is shown in Fig. 4.5 (black curve).

Before the atoms are transferred from the MOT to the dipole trap ($t < 0$), we observe fluorescence mainly from the MOT-cloud surrounding the nanofiber [16,17,39] and from a few trapped atoms. As soon as the loading sequence starts ($t = 0$), the detuning is increased in one single step to $\Delta = -80$ MHz with respect to the light shifted cooling transition. This reduces scattering in the first place but afterwards
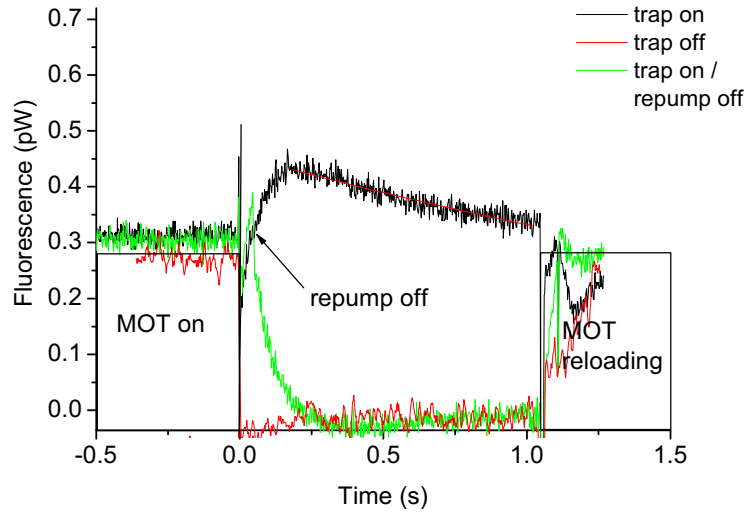
FIGURE 4.5: Fluorescence excited by the MOT-laser beams and detected as the light is channeled into the nanofiber waist of the TOF. The loading of the dipole trap starts at $t = 0$, and is performed with a fixed detuning of $\Delta = -80$ MHz. As a reference the red curve indicates the background level caused by the MOT-beams without the dipole trap. The green curve shows the remaining fluorescence when the trapped atoms are pumped into a dark state. The boxes on the left and on the right mark the operation of the MOT.

the accumulation of trapped atoms leads to an increase of the fluorescence signal. Within the first 200 ms, when about 2000 atoms are loaded into the trap, the measured fluorescence increases up to 0.5 pW, showing a loading characteristic similar to that measured with our conventional loading sequence (see Sect. 3.3.1). Without the presence of the trapping fields around the nanofiber the signal drops to the zero level (red curve). Note that the background level of 0.4 pW corresponding to the coupling of the MOT-beams into the fiber guided mode has been subtracted for all plots shown in Fig. 4.5.

As a second reference, the fluorescence is measured after switching off the repump laser, thereby pumping the atoms into a dark state (green curve). The subsequent decay into the $|F = 3\rangle$ state decouples the atoms from the cooling light of the MOT (i.e., the detuning of the probe light increases significantly to 9.2 GHz), and thus unveils the background level.

Note that the opacity of the MOT-cloud is small at detunings of -80 MHz, hence the expansion of the atomic cloud during the loading procedure does not affect the intensity of the MOT-beams arriving at the nanofiber. Thus, the measured fluorescence is expected to depend only on the number of trapped atoms. The large detunings also ensure that the losses through reabsorption of the fiber-coupled light can be neglected. Furthermore, the detuning of the MOT-lasers close to

$\Delta = -80$ MHz (with an intensity of about 8 mW/cm^2), provides molasses cooling in our trap and allows for counteracting heating and losses of atoms. The resulting storage time, indicated by the slow exponential decay of the fluorescence signal, is raised up to $\tau \approx 3.5$ s, limited by the background pressure of the vacuum chamber.

Results and Discussion

From the measurements of the maximum fluorescence light power arriving at one end of the fiber $P_{\text{meas.}} = 0.5$ pW, the number of trapped cesium atoms $N \approx 2000$ (cf. Sect. 3.3.2) emitting into the nanofiber, and the total MOT-beams peak intensity of 8 mW/cm^2, we deduce the coupling efficiency (neglecting losses in the TOF)

$$\eta = \frac{P_{\text{meas.}}}{P_{\text{scat.}}} \tag{4.10}$$

to be $\eta \approx 2.3(2)\%$, where the scattering power $P_{\text{scat.}} = N R_s \hbar \omega_0$ is found to be approximately 22 pW with a scattering rate of $R_s \approx 50$ kHz. Here, we have assumed a saturation intensity of $I_{\text{sat}} = 2.7$ mW/cm^2 for isotropically polarized light [49]. The measured coupling efficiency and the theoretically expected value $\eta_{\text{flou.}} = 2.7\%$ are in good agreement within the experimental uncertainties. As a comparison to free-beam optics, the collection efficiency of $\eta \approx 2.3\%$ would require an objective lens with an NA of about 0.3 [101]. Note that the depth of focus (or Rayleigh length) for such an NA would not exceed the length of the ensemble (> 1 mm) or the nanofiber.

In conclusion, we have experimentally demonstrated efficient probing of fluorescence emitted by atoms trapped in the vicinity of the nanofiber surface. Such an efficient coupling of the atomic fluorescence into the TOF, makes the outlined method ideally suitable for investigation of, e.g., spontaneous emission in close vicinity of a dielectric surface of a wave-guide. Particulary, the strong confinement of the atoms in the nanofiber trap opens the way for investigation of atom-surface interactions with high precision and an unprecedented spatial resolution: The possibility to position the atoms very close to the surface may lead to interesting applications in terms of cavity quantum electrodynamics (cavity-QED), and studies of van der Waals and Casimir-Polder interactions with the fiber surface [54–57].

Moreover, for an atomic ensemble prepared in a certain one-excitation state, i.e, when a single electronic excitation is indistinguishably shared between the atoms, the coupling efficiency of the subsequently emitted photon into the nanofiber can be close to unity [129]. This collective enhancement of emission into the nanofiber might be a key factor in the realization of fiber-coupled single-photon sources, as required for the implementation of quantum information technologies.

4.3   Nondestructive Phase Detection

The absorption measurements performed on our system reveal that resonant scattering can be very efficiently employed for interfacing light and matter, making our system a prime candidate for detection and manipulation of atoms at the quantum level. A major drawback of this method, however, is the accompanying absorption and spontaneous re-emission of photons which results in damping of the light-mode and heating of the probed atomic ensemble.

The successful implementation of quantum information schemes requires means to make measurements of the atomic ensemble without destroying the internal quantum states being used [131]. Such quantum non-demolition (QND) measurements are usually made by employing the dispersive effect of the atomic ensemble caused by the coherent forwards scattering of photons, which has been shown to be more powerful than absorption or florescence-based detection techniques. Typically, the dispersion is detected either through interferometry [132], frequency modulation spectroscopy or phase-contrast imaging, used most often for imaging Bose-Einstein condensates [138].

In the following we demonstrate that, in the context of the atoms trapped with an optical nanofiber, a similar QND measurement can be very simply realized by taking advantage of the intrinsic birefringence of the system. A signal is derived that is proportional to the optical phase shift induced by the atoms, which is in turn proportional to the number of atoms trapped around the fiber. In addition to its non-destructive nature, this technique is fast, simple, features good signal to noise ratios and avoids the spectral complexity often entailed in the resonant absorption approach.

Note that parts of this section are prepared for publication [149].

Method

In the nanofiber-based trapping scheme demonstrated above, resonant detection of the atoms may be achieved by coupling a probe beam at a wavelength of 852 nm into the fiber. This beam couples efficiently to the atoms via its evanescent field resulting in an absorbance per atom of the order of one percent (measured at the light shifted resonance for the strong $F = 4 \rightarrow F' = 5$ transition in cesium).

For finite detunings such strong coupling also leads to a significant phase shift of the probe light. This can be understood by considering the Lorentz model which predicts advanced or retarded phase relation between the driving field and the induced dipole moment depending on the sign of the detuning (see Sect. 2.1). Both the absorption as well as the phase retardation can be derived from the complex polarizability or the complex refractive index $\tilde{n} = \sqrt{1 - 4\pi n\alpha(\omega)}$ [137]. For $|\tilde{n} - 1| \ll 1$

and detunings $\Delta = \omega_0 - \omega$ larger than the splitting of the Zeeman sub-levels associated with the ac-Stark shift induced by the trapping fields, we obtain

$$
\begin{aligned}
\tilde{n} - 1 &= \frac{\lambda}{4\pi l} \sum_{F,F'} \sigma_{I,J,J',F,F'} \frac{\Delta_{FF'} + i}{\Delta_{FF'}^2 + 1} \frac{N_F}{A_{\text{eff}}} \\
&= \frac{\lambda^3}{8\pi^2} (2J' + 1) \sum_{F,F'} (2F' + 1) \\
&\quad \times \left\{ \begin{array}{ccc} J & F & I \\ F' & J' & 1 \end{array} \right\}^2 \frac{\Delta_{FF'} + i}{\Delta_{FF'}^2 + 1} \frac{N_F}{A_{\text{eff}} l},
\end{aligned}
\tag{4.11}
$$

where $\sigma_{I,J,J',F,F'}$ is the resonant absorption cross-section for each transition labeled by I, F and J, which are the nuclear, total atomic and total electronic angular momenta quantum numbers respectively, and where the primed quantum numbers refer to the excited states. Here, $\Delta_{FF'} = 2(\omega_{FF'} - \omega)/\Gamma$ is the normalized detuning of the probe light with an average wavelength λ, Γ is the natural linewidth, N_F is the population of the ground state, l is the length of the sample, and A_{eff} is the effective cross-sectional area of the probe light. The complex response function for transmitted radiation is given by $\exp(i(\tilde{n} - 1)2\pi/\lambda)$. The absorptive component of the light-atom coupling can be expressed in terms of the optical density [138]

$$
\begin{aligned}
OD(\Delta_{FF'}) &= \frac{4\pi l}{\lambda} \text{Im}\{\tilde{n} - 1\} \\
&= OD_0 \frac{1}{\Delta_{FF'}^2 + 1},
\end{aligned}
\tag{4.12}
$$

where $OD_0 = \sigma_{J,J',F,F',I} N_F / A_{\text{eff}}$ is the resonant optical density. Similarly, the phase shift imparted on the probe light is given by

$$
\begin{aligned}
\phi(\Delta_{FF'}) &= \frac{2\pi l}{\lambda} \text{Re}\{\tilde{n} - 1\} \\
&= \frac{OD_0}{2} \frac{\Delta_{FF'}}{\Delta_{FF'}^2 + 1}.
\end{aligned}
\tag{4.13}
$$

The maximum phase shift, which occurs at $\Delta_{FF'} = 1$, is $\phi_0 = OD_0/4$. Eqs. (4.12) and (4.13) show that for significant detunings, the phase shift can be substantial even when the absorption is negligible, since $OD/\phi \propto 1/\Delta_{FF'}$. We also note that for $\Delta_{FF'} \gg 1$, we have $\phi(\Delta_{FF'}) = OD_0/2\Delta_{FF'}$. A common approach to detect the phase shift induced by an optically dense atomic medium is to compare the phase of a probe beam passing through the medium with the phase of an external reference beam, i.e., by using an interferometer [132,138]. In the case of atoms being trapped in two linear arrays around the fiber (see Fig. 4.6), one is able to take a similar approach due to the inherent asymmetry of the coupling between the quasi-linear HE_{11} optical modes with linear polarization that propagate in the nanofiber and the atomic ensemble [32].

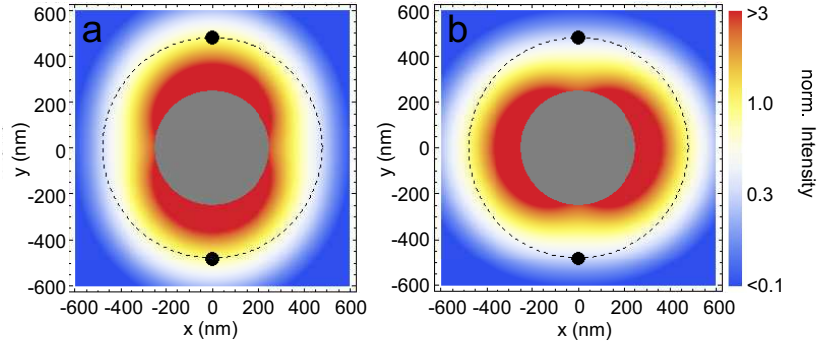FIGURE 4.6: Normalized intensity distribution $(I(x,y)/I(\mathrm{r_{at}})_{\max})$ scaled by the maximum intensity of the evanescent field at the position of the atoms $I(\mathrm{r_{at}})_{\max}$ for (a) the polarization axis aligned parallel to the axis containing the atoms and (b) the polarization aligned perpendicular to it. The filled black circles indicate the position of the trapped atoms at a distance of 230 nm (black dashed circle) from the surface of the 500-nm diameter nanofiber (represented by gray cross-section). The color scheme has been scaled logarithmically.

Here, the rotational symmetry of the propagation medium is broken by the presence of the arrays of trapped atoms above and below the nanofiber, and the remaining mirror symmetry dictates that the eigenmodes of the system consist of the HE_{11} optical mode oriented either parallel or perpendicular to the axis containing the atoms. We denote these axes the strong-coupling axis and the weak-coupling axis respectively, because the coupling of the eigenmodes differs significantly due to the substantial azimuthal variation of the evanescent field intensity of the HE_{11} mode. Note that the same feature of the HE_{11} mode produces the azimuthal confinement of the trapping potentials [31].

For the probe light at a wavelength of 852 nm the eigenmode with the polarization axis parallel to the axis containing the atoms, denoted by $|\Psi_{\parallel}\rangle$, couples 2.8 times more strongly to the atoms than the eigenmode perpendicular to the axis containing the atoms, $|\Psi_{\perp}\rangle$, corresponding to the ratio of intensity at the center of the trap, i.e., at a distance of $r_{\mathrm{at}} \sim 230$ nm from the fiber surface, in each case (see Fig. 4.6). The resulting difference in coupling leads not only to a higher optical density for $|\Psi_{\parallel}\rangle$ but also results in a larger optical phase shift accumulated along the fiber, thereby producing a birefringent effect. By probing the atoms with a linear combination of $|\Psi_{\parallel}\rangle$ and $|\Psi_{\perp}\rangle$ one can measure this differential phase shift by observing the change it causes to the polarization state. The comparison with the interferometric method shows here, that the weak coupling polarization mode plays a similar role as the phase reference and that the probing may therefore be performed with only one beam, thus avoiding the need for stabilization of a reference beam path.

This method resembles conventional polarization spectroscopy, except that the birefringence does not need to be induced via optical pumping of the atomic sample [92].
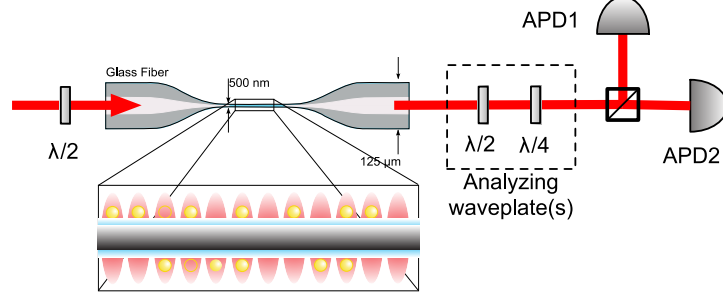
FIGURE 4.7: Setup for the birefringent phase measurement. A detuned light field is coupled into the nanofiber to probe the cesium atoms, which are trapped in the evanescent field of the nanofiber (zoomed inset). A Stokes measurement is performed on the outgoing beam using the analyzing waveplates, a polarizing beam splitter and two avalanche photodiodes.

Figure 4.7 shows a schematic of the measurement approach. A probe beam is coupled into the fiber with the polarization adjusted to $45°$ with respect to the strong axis in order to excite a superposition of both eigenmodes $|\Psi_\parallel\rangle$ and $|\Psi_\perp\rangle$ with equal powers, i.e., $|\Psi_{\text{in}}\rangle = \frac{1}{\sqrt{2}}\begin{pmatrix} 1 \\ 1 \end{pmatrix}$ in terms of the normalized Jones vector [134].

The two initially degenerate modes then propagate through the fiber, interacting with the birefringent atom-fiber system, thus exiting the other end of the fiber in a modified polarization state. When the light passes through the trapped atomic ensemble, the state undergoes a simple transformation of the magnitude and phase to produce the polarization state at the output of the fiber. This polarization state is then determined by measuring the Stokes vector by simply splitting the beam with a polarizing beam splitter (PBS) for different settings of the analyzing waveplates and measuring the power of either port with an avalanche photodiode (APD). The resulting polarization of the light incident on the PBS may be expressed in terms of the Jones calculus formalism:

$$
\begin{aligned}
|\Psi_{\text{out}}\rangle &= \mathrm{R} \begin{pmatrix} t_\parallel e^{i\phi_\parallel} & 0 \\ 0 & t_\perp e^{i\phi_\perp} \end{pmatrix} |\Psi_{\text{in}}\rangle \\
&= \frac{1}{\sqrt{2}}\mathrm{R} \begin{pmatrix} t_\parallel e^{i\phi_\parallel} \\ t_\perp e^{i\phi_\perp} \end{pmatrix},
\end{aligned}
\tag{4.14}
$$

where the light-atom interaction is modeled by transmissions $t_\parallel^2 = e^{-OD_\parallel}$ and $t_\perp^2 = e^{-OD_\perp}$ and phase shifts $\phi_\parallel$ and $\phi_\perp$, experienced by the basis states $|\Psi_\parallel\rangle$ and $|\Psi_\perp\rangle$ respectively, and R is the Jones matrix describing the phase retardation produced by the analyzing waveplate(s) in Fig. 4.7. Here we assume that the birefringence of the fiber itself and other optical components is negligible. In any case these contributions can be compensated by using variable retardation plates as, e.g., Berek compensators.

Stokes Measurement

By measuring with three different configurations c of the analyzing waveplate(s), we can fully characterize the beam's polarization state and obtain the Stokes vector [135] (normalized here to the total beam power):

$$S = \begin{pmatrix} S_0 \\ S_1 \\ S_2 \\ S_3 \end{pmatrix} = \begin{pmatrix} 1 \\ (P_{\|,1} - P_{\perp,1})/(P_{\|,1} + P_{\perp,1}) \\ (P_{\|,2} - P_{\perp,2})/(P_{\|,2} + P_{\perp,2}) \\ (P_{\|,3} - P_{\perp,3})/(P_{\|,3} + P_{\perp,3}) \end{pmatrix}$$

$$= \begin{pmatrix} 1 \\ \frac{t_\|^2 - t_\perp^2}{t_\|^2 + t_\perp^2} \\ \frac{2 t_\| t_\perp}{t_\|^2 + t_\perp^2} \cos\left(\phi_\| - \phi_\perp\right) \\ \frac{2 t_\| t_\perp}{t_\|^2 + t_\perp^2} \sin\left(\phi_\| - \phi_\perp\right) \end{pmatrix}, \qquad (4.15)$$

The quantities S_0-S_3 are the observables of the polarized light field (cf. Fig. 4.8) via the powers $P_{\|,c}$ and $P_{\perp,c}$ detected at the two output ports of the PBS in three configurations:

($c = 1$) when the analyzer axis is aligned to the strong-coupling axis

$$\mathrm{R} = \begin{pmatrix} 1 & 0 \\ 0 & 1 \end{pmatrix}, \qquad (4.16)$$

($c = 2$) when the analyzer axis is at $45°$ to the strong-coupling axis

$$\mathrm{R} = \frac{1}{\sqrt{2}} \begin{pmatrix} 1 & 1 \\ 1 & -1 \end{pmatrix}, \qquad (4.17)$$

($c = 3$) when a quarter-wave plate has been inserted at $45°$ to the analyzer

$$\mathrm{R} = \frac{1}{2} \begin{pmatrix} 1+i & 1-i \\ 1-i & 1+i \end{pmatrix}, \qquad (4.18)$$

respectively, and the total power can of course be measured by the sum of the PBS powers in any of those configurations. In practice these configurations are set by a half-waveplate and/or a quarter-waveplate included before the PBS, as indicated in Fig. 4.7. The second line in Eq. (4.15) is determined by calculating $P_\| = |\langle \Psi_\| | \Psi_{\mathrm{out}} \rangle|^2$ and $P_\perp = |\langle \Psi_\perp | \Psi_{\mathrm{out}} \rangle|^2$ from Eq. (4.14) with the appropriate waveplate matrix R. It is immediately evident from Eq. (4.15) that both S_2 and S_3 provide the means to measure the phase difference $\Delta\phi = \phi_\| - \phi_\perp$, but S_3 is more convenient because it also gives access to the sign. The prefactor in S_3 is unity when the absorption is negligible ($t_\| = t_\perp = 1$), as is the case far off-resonance.

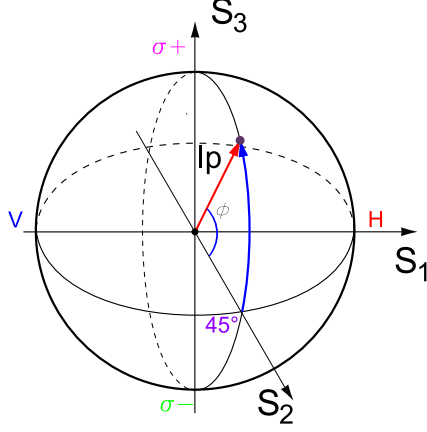FIGURE 4.8: Poincaré sphere representation of birefringence. The stokes vector (red arrow) is rotated from the equator at 45° pol. position by an angle ϕ, corresponding to the phase difference induced by the birefringent medium. Without absorption the length of the Stokes vector I_p, corresponding to the intensity, stays unchanged. Here, the colored symbols around the sphere indicate the corresponding state of polarization.

It is also worth noting that S_1 is independent of the phase difference $\Delta\phi$, which provides a convenient experimental parameter to determine the orientation of the strong-coupling/weak-coupling axis.

In order to deduce the absolute phase shift in a particular axis, we use the proportionality established in Eq. (4.13) that $\phi \propto \mathrm{OD}_0 \propto 1/A_{\mathrm{eff}}$ and therefore proportional to the local intensity of the light. This assumption is valid as long as the ground state population is evenly distributed, i.e., the ensemble has not been optically pumped, as is typically the case for atoms produced by a magneto-optical trap (MOT) [5]. From the model of the fiber mode, the ratio is then $\phi_\perp/\phi_\parallel \simeq 1/2.8$ (see Sect. 1.3.2), leading to

$$\phi_\parallel = (1 - \phi_\perp/\phi_\parallel)^{-1} \Delta\phi \simeq 1.6\,\Delta\phi. \tag{4.19}$$

Results and Discussion

The method outlined above was applied to the apparatus described in Sect. 3.2. In order to maintain the linearity of the probe beam polarization under rotation, a Berek compensator was used to compensate for the birefringence of the beam splitter used to combine the probe beam with the trapping beams. Berek compensators were also used on the input and output of the fiber to compensate for the birefringence present in the section of standard optical fiber, e.g., caused by strain

due to bending. The result is that the probe beam polarization is linear both at the input of the TOF and the output after passing the Berek compensator, and also results in a quasi-linear HE_{11} mode.

By observing the Rayleigh scattering from the nanofiber, we estimated the impurity of the polarization to be less than a few percent (this value has been measured at wavelengths of 780 nm and 1064 nm but we assume it to also hold for the weak probe beam at a wavelength of 852 nm). Finally, the components of the Stokes vectors are determined by calculating the ratio of the difference and the sum of the powers at each port of the PBS as measured with two APDs. To measure S_3, a quarter-waveplate is included with its optical axis aligned at $45°$ to the PBS.

Without any trapped atoms, the output polarization remains linear. Introducing trapped atoms will in general change the value of the Stokes measurement, but the sensitivity will depend on the orientation of the input polarization. By adjusting the angle of the input polarization (and simultaneously adjusting the output quarter-waveplate to preserve the S_3 measurement), one can find the strong-coupling axis or the weak-coupling axis where the Stokes measurement with atoms goes to 0. The highest sensitivity to the presence of atoms is obtained in between these axes, i.e., at $\sim 45°$, corresponding to S_3 in Eq. (4.15). The signal near resonance, however, will be compromised for a number of reasons. Firstly, absorption becomes significant near resonance, which not only alters the polarization state as described by the prefactor in S_3 in Eq. (4.15), but also results in a loss of signal simply because less light is available for detection, particularly with the high optical density scenario examined here. Secondly, the absorptive interaction results in more scattering events, which begins to perturb the initial preparation of the ensemble via either optical pumping or heating and thus loss of atoms from the trap. Thirdly, the spectral shape of the signal is complicated near resonance due to the presence of the strong trapping fields, which results in a frequency shift and inhomogeneous broadening of the resonance via ac-Stark shifting of the Zeeman sub-states (see Sect. 2.2). Furthermore, this inhomogeneous broadening is also different for the two polarization states, thus complicating the spectrum measured via the phase difference. Finally, should it be possible to overcome the signal to noise issues at high optical densities (i.e., where the phase difference $\Delta\phi$ may exceed $\pi/2$), the spectrum will also exhibit discontinuities due to the wrapping resulting from the sinusoidal term in the expression for S_3. One may avoid all of these issues, however, by using the measured signal only at significant detunings, where the overall absorption is less than a few percent.

Figure 4.9 shows a measurement of the phase shift $\phi_{\parallel,\text{meas}} = 1.6 \sin^{-1}(S_{3,\text{meas}})$, where the frequency of the probe has been scanned across the $F = 4 \rightarrow F' = 5$ transition in cesium. For completeness, we performed a full scan through the resonance, see Fig. 4.9 (light red points). Here, the solitary data points ($|\Delta| > 100$ MHz) have been recorded at a fixed detuning in each individual experimental run. The
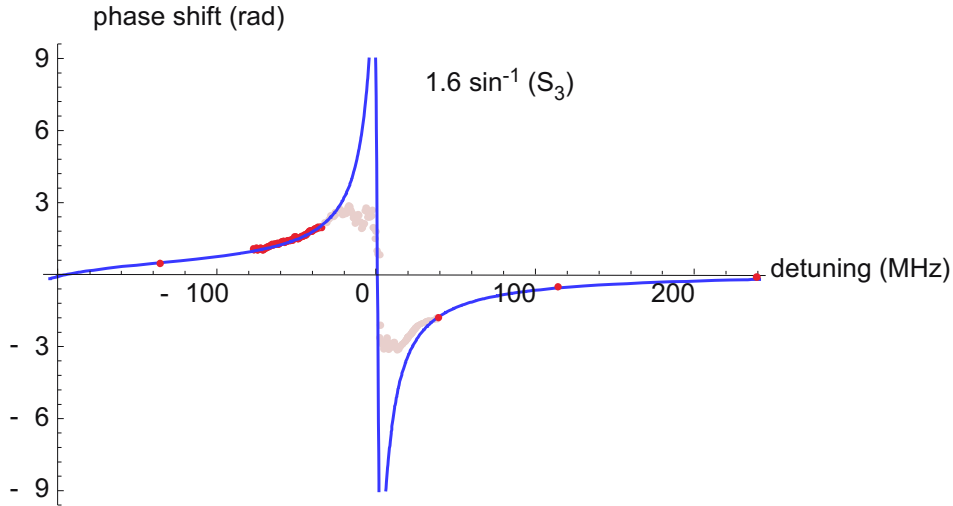
FIGURE 4.9: Phase shift in the strong-coupling axis as a function of the detuning from the $F = 4 \rightarrow F' = 5$ transition, estimated from the measurement of the fourth element of the Stokes vector (S_3). The blue line is a fit using Eq. (4.13). Note that for the measurement close to the resonance (light red points) optical pumping as well as inhomogeneous broadening is expected to decrease the phase shift.

other data points have been taken while scanning the probe light detuning within 5 ms from -80 to $+40$ MHz. For further estimation of the phase shift we fitted the measured spectrum using Eq. (4.13). (Note that we have omitted the data points which have been taken after scanning through the near-resonant region, i.e., $\Delta > -30$ MHz.)

The fit in Fig. 4.9 takes the functional form of the unbroadened dispersion in Eq. (4.13) with the natural linewidth of the transition of $\Gamma = 5.2$ MHz. The fitted maximum phase and maximum optical density in the strong-coupling axis are $\phi_\parallel(\Delta_{4,5} = 1) = 12(1)$ and $OD_{0,\parallel} = 48(5)$ respectively.

The measured number of atoms for that measurement was approximately 2000, yielding an approximate absorbance per atom of $\eta = OD/N = 2.6\,\%$ providing an estimate of the effective far-detuned resonant absorption cross-section of $\sigma = \eta A_{\mathrm{eff}} = 0.8 \times 10^{-9}\,\mathrm{cm}^2$. This is about $40\,\%$ less than the expected value of $1.4 \times 10^{-9}\,\mathrm{cm}^2$ (cf. Sect. 4.1). This may be a result of optical pumping during the loading process or residual resonant excitation induced by the probe light. However, as expected, we find a larger on-resonance OD than we actually measure in absorption ($OD_{0,\parallel}^{\mathrm{Abs}} = 32$), simply because far off-resonance dispersion is not affected by inhomogeneous broadening, thus the reduction of the coupling strengths can be neglected.
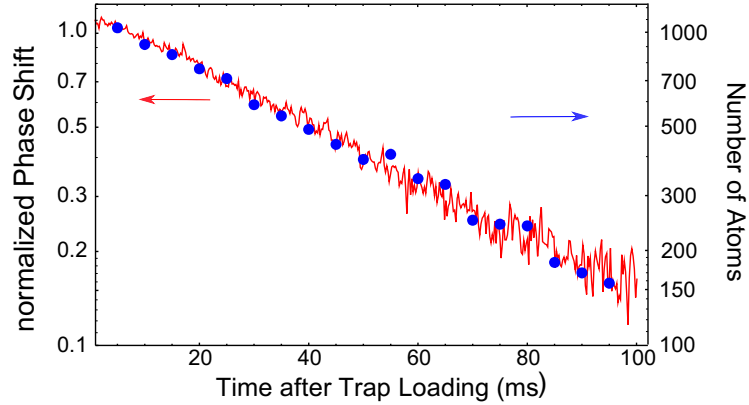
FIGURE 4.10: (red curve) Evolution of the phase shift for about 1000 atoms, $P = 4$ pW, and $\Delta = 165$ MHz during 100 ms of continuous probing. As a reference, the blue dots indicate the loss of atoms in absence of any resonant light, measured by absorption for different delay times in each individual experimental run (cf. Sect. 3.3.5).

Non-destructive measurement and influence of the probe light

The capacity of the outlined phase detection scheme to operate far off-resonance, where absorption is negligible and scattering rates are low, raises the possibility of performing QND measurements that do not perturb the quantum states of the trapped atoms. In order to demonstrate the non-destructivity of this measurement technique, we performed an atom number measurement of the atomic ensemble using the phase measurement technique over 100 ms and compared it with a series of conventional absorption measurements with successively longer delay times (see Fig. 4.10), as we have performed for the lifetime measurements in Sect. 3.3.5.

Due to an yet not fully understood heating mechanism and limitation of the trap lifetime, the conventional absorption measurement reveals an exponential decay of the population of the trapped ensemble with a lifetime of about 50 ms. The lifetime of the phase signal was also measured to be about 50 ms, which indicates that no significant perturbation in form of heating or optical pumping is produced by the presence of the probe light, and that the measurement is non-destructive to the phase shift and the atom number.

In this measurement, the probe light power was about 4 pW, blue-detuned by 165 MHz from the light-shifted $F = 4 \rightarrow F' = 5$ transition which corresponds to a scattering rate of about 30 s^{-1} (or about 3 photons scattered by each atom over 100 ms measurement. For detunings $\Delta \lesssim 30$ MHz, the lifetime of the phase measurement drops below that of the absorption measurement, despite there still being very low absorption. We believe this to be a result of optical pumping by the probe light that perturbs the initially evenly populated Zeeman sub-states into

atomically aligned states [49]. Such a process would alter the relative coupling of the strong and weak axis, thereby changing the birefringence that provides the basis for this technique. Indeed, we have observed that under certain conditions conducive to optical pumping, i.e., at low detuning and high probe light intensity, the birefringent signal is reduced to almost zero in a few milliseconds.

Conclusions

We have demonstrated the non-destructive phase detection of an atomic ensemble trapped around an optical nanofiber. The resulting estimate of the effective resonant absorbance per atom of $\eta = 2.6\%$ clearly reveals the high coupling implicit in this system that makes it an attractive platform for interfacing the quantum properties of an ensemble of cold atoms with optical fiber-based systems. This approach could be applied to derive information about the quantum state of the atoms, in order to prepare them in a known state, e.g., via optical pumping. This may also help to realize a photonic phase gate, in which the phase of a photon is changed depending on the internal state of the atoms [139].

Chapter 5

Conclusions and Outlook

In this thesis I have presented the realization of a fiber-based optical interface using optically-trapped cesium atoms. I have shown that our method provides an efficient tool for coupling light and atoms, and that it is ideally suited to interconnecting different quantum systems. Furthermore, it might enable the realization of fiber-coupled quantum memories in the context of quantum information processing and transmission. The basic principle of the presented coupling scheme relies on trapping of neutral cesium atoms in a two-color evanescent field surrounding a nanofiber. The strong confinement of the fiber guided-light, which also projects outside the nanofiber in the form of an evanescent field, enables strong confinement of the atoms as well as efficient coupling to resonant light propagating inside the fiber.

In the theoretical part of my work, I have analyzed the fundamental properties of light propagation inside an optical nanofiber. The discussed solutions of Maxwell's equations provide the exact modeling of the distribution and orientation of the field outside the fiber, thereby allowing one to compute the trapping potentials and the atom-light coupling in the vicinity of a nanofiber. The theoretical considerations of light-atom interaction have been completed by a quantum mechanical description of the atomic level shifts of the new atomic eigenstates in the presence of two arbitrarily polarized light fields.

The experimental part of this work reported on the fabrication of tapered optical fibers (TOF) with a sub-wavelength diameter from standard glass fibers, and their optimization in terms of transmissivity and persistence against high laser intensities. Our resulting TOFs feature efficient transfer of the guided mode into and out of the nanofiber waist with negligible losses, and carry up to a few hundred milliwatts of laser light in vacuum without fusing. This achievement was a crucial step towards the realization of the nanofiber-based trap.

The trapping scheme has been realized by launching a combination of a linearly polarized blue-detuned running wave and a red-detuned standing wave into the TOF, thereby forming two 1d-lattice potentials above and below the nanofiber. Since this scheme critically depends on the polarization of the fiber-guided light, a simple procedure of monitoring and controlling of the polarization on the nanofiber waist has been introduced. Via observation of the angular distribution of Rayleigh scattered light, emitted by the nanofiber, we are able to precisely align the polarization of each trapping field.

The implementation of trapping of cesium atoms around an optical nanofiber has been accomplished using well-established laser-cooling techniques. A conventional magneto-optical trap (MOT), serving as a source of cold cesium atoms, is overlapped with the waist of the TOF, while the ends of the TOF establish a direct link to the exterior laser setup. By this means, the cold atoms can be efficiently transferred from the MOT into the nanofiber trap. Due to the small trapping volumes the loading operates in the collisional blockade regime resulting in an occupancy of at most one atom per trapping site. Furthermore, our optimized loading scheme provides sub-Doppler cooling of the atoms to temperatures of about 28 μK, resulting in a high occupancy of the vibrational ground state in the nanofiber trap.

In addition to the optimization of the loading/cooling process, I have analyzed our trap in terms of confinement of atoms and their storage time. The measurements of the trapping frequencies indicate strong confinement of the cesium atoms which is compatible to the modeled trapping potentials. In contrast to this, the storage time is significantly shorter than expected. In this context, I have investigated the impact of several sources of noise which lead to heating and result in the loss of atoms. Particularly, the phase fluctuations of the standing wave, presumably induced by spontaneous Brillouin scattering in the TOF, should lead to strong heating, and is probably the limiting factor of the trap lifetime.

By introducing a moving standing wave in our trap and by imaging of the atoms, we were able to demonstrate the transportation of the atoms along the nanofiber in spite of the relatively short trap lifetime in this configuration. This result promises a viable way of deterministic delivery of individual atoms, and loading of the atoms along the whole length of the nanofiber.

The successful interfacing of the trapped ensemble and the fiber-guided light is another central part of this thesis. In the vicinity of the nanofiber surface, each atom can scatter (absorb) a significant fraction of photons propagating in the nanofiber. The analysis of the spectroscopic properties of the trapped atoms in absorption measurements exhibits good agreements with the predictions of the light-induced ac-Stark shift presented in the theoretical part. With 2000 fiber-coupled atoms we obtain an optical density (OD) up to 32. We also found signatures of optical pumping via the probe light, which in this context might be a convenient way to prepare the atoms in a single Zeeman substate. This should diminish the effects

of inhomogeneous broadening and thus increase the OD. The demonstrated strong coupling of the atoms and the fiber-guided modes allows us to probe the ensemble also via a phase measurement even at large detunings where the absorption of the probe light is negligible. The inherent birefringence, caused by the anisotropy of the evanescent field and the azimuthal arrangement of the trapped atoms around the fiber, provides a sensitive means of interrogation of atomic states. In this scheme, the state of polarization of the probe light changes while propagating through the nanofiber and interacting with the atomic ensemble. The birefringence induced by the atoms is then easily detectable via a Stokes vector measurement. At large detunings from resonance we could even demonstrate the non-destructive nature of this measurement.

In conclusion, the presented technique for the coupling of light and atoms opens the route for numerous unique applications, such as the direct integration of atomic quantum devices into fiber networks, an important prerequisite for large scale quantum communication schemes. More generally, this work is an important step towards the realization of hybrid quantum systems in which atomic ensembles can be optically interfaced with, e.g., solid state quantum emitters. Trapping and interfacing atoms in close vicinity of solid state devices, coupled via electric or magnetic interaction, would one allow to combine the advantageous properties of both systems for quantum information processes.

5.1 Coherent light-matter interaction

5.1.1 EIT and quantum memories

In order to proceed towards the implementation of fiber-coupled quantum devices, it is essential to explore the coherence properties of our system. For this purpose we are considering the demonstration of electromagnetically induced transparency (EIT) [140], which provides the possibility of storing quantum information recorded as a spinwave in an atomic ensemble [141].

The prerequisite for EIT is, besides a very high optical density of the atomic ensemble, the presence of two energy states in which (superposition) the atoms can remain for a long time without significant loss of coherence. Such is the case for sub-levels of different angular momentum (spin) within the electronic ground state of, e.g., cesium atoms exhibiting two metastable lower hyperfine states, e.g, $|g\rangle = |6S_{1/2}, F = 4\rangle$ and $|s\rangle = |6S_{1/2}, F = 3\rangle$, which can be coupled to an excited state (e.g., $|e\rangle = |6P_{3/2}, F = 4\rangle$) either via the control field or the probe pulse, respectively (see Fig. 5.1). Such a Λ-type atomic level structure (see Fig. 5.1) offers the required long coherence time for the collective spin excitation or a spinwave (SW), which is required to make the storage and retrieval of photons feasible [141].
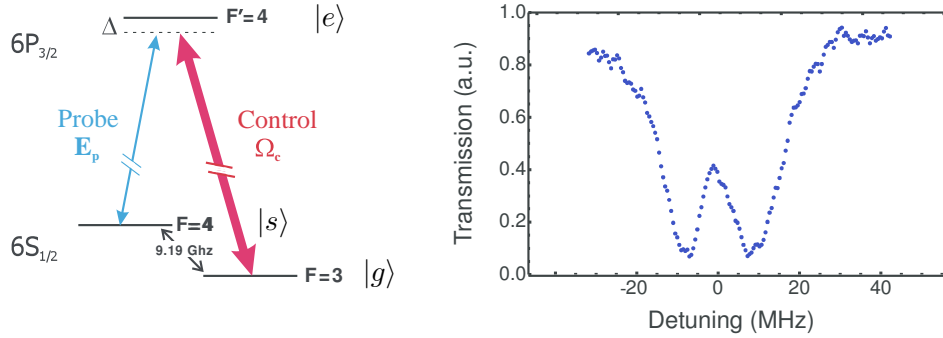
FIGURE 5.1:   First attempts to realize EIT with fiber-coupled cesium atoms.
(left) A lambda system for cesium making use of the two stable hyperfine states
$F = 3$ and $F = 4$, the classical control field denoted by Ω_c, and a weak probe
field denoted by E_p. On two-photon resonance, the excitation pathways $|s\rangle$–$|e\rangle$
and $|s\rangle$–$|e\rangle$–$|g\rangle$–$|e\rangle$ are indistinguishable, leading to destructive interference of the
transition amplitude thus causing transparency of the medium. (right) Transmis-
sion spectrum of the probe trough the fiber-coupled atoms in the presence of the
coupling field (1 nW). (Note that the transparency window is broadened because
the relative phase of the probe and coupling laser has not been stabilized.)

The proposed deterministic scheme for storing and retrieving photons refers to "slow
light" or "stopped light" which is based on the coherent control of propagation of
the coupled light-matter excitation known as a "dark state polariton" (DSP) [142].
This control is performed under the condition of EIT, where a coherent coupling
field leads to mixing of the photonic ($\hat{E}$) and excitonic ($\hat{\sigma}_{\text{spin}}$) part of the polariton
field [140]

$$\Psi = \cos\theta \hat{E} - \sin\theta \sqrt{n} \hat{\sigma}_{\text{spin}}, \tag{5.1}$$

with $\tan^2\theta \propto n/\Omega_c^2$, where Ω_c denotes the Rabi frequency associated with the cou-
pling field, and n is the atom number density. By adiabatically changing the control
field strength one can thus transfer the coupled excitation into a stationary atomic
spin excitation (spinwave), thereby storing the light pulse in the EIT medium [140].
Depending on the decoherence rate of this medium the light pulse can be retrieved
after a certain storage time.

The coherence times demonstrated in the recent experiments involving atomic en-
sembles in a MOT are mainly limited by dephasing due to the thermal motion of the
atoms and were found to be less than one millisecond [27]. A Longer coherence time
is feasible by a reduction of the temperature but is still limited due to the free-fall
under gravity. Other approaches employing dipole traps and optical lattices have
shown dephasing effects due to collisions. In comparison to those approaches, our
nanofiber trap stores at most one atom per trapping site and thus prevents atomic
collisions. Furthermore, the thermal motion of the trapped atoms is strongly re-
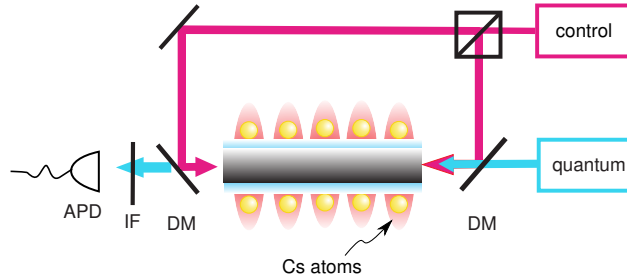stricted (almost to the oscillatory ground state), with respect to the propagation

FIGURE 5.2: Schematic of a setup for EIT with fiber-coupled atoms. By using counter propagating control beams stationary DSPs can be created.

direction of the spinwave. Hence, we expect the coherence time provided by our trap to be limited mainly by electronic excitations and loss of atoms, which might be in the order of 50 ms. We believe that the fiber-coupled atomic ensemble in our experiment has the capacity to fulfil the requirements for EIT with fiber-coupled atoms, which is supported by our first attempts (see Fig. 5.1). Currently, we are working on the increasing the lifetime and lowering the heating rate in our trap, which may increase the coherence time to a few hundred milliseconds.

Note that, a further improvement might be obtained by employing a pure blue detuned nanofiber-based trap as we proposed in [40], potentially providing coherence times of more than a second.

5.1.2   Dark state polariton physics

The targeted improvement of coupling light and the atomic ensemble, e.g., using optical pumping and loading along the whole nanofiber, may open the route towards efficient photon-photon interaction enabled by EIT [141]. Such non-linear interaction may not only be a step towards the realization of all-optical quantum logic gates [147], but would permit to tailor the interaction of dark state polariton (DSPs).

The enhancement in nonlinear optical efficiency may be produced by either simultaneously slowing down a pair of light pulses in order to enable a long interaction time [141] or using stationary-light techniques [143]. For the latter, the enhancement can be dramatically increased via a Kerr-like interaction [143,144]. In this case the probability of interaction between two single photons scales as $\sim OD\lambda^2/A_{\mathrm{eff}}$, resulting in a significant phase shift for the photons. The required optical depth $OD > 100$ can be realized within modest improvements (see Sect. 4.1), thus nonlinear interaction of even two guided photons appears within reach.

Finally, the demonstrated coupling scheme opens up the possibility of creating strongly interacting many-body photon states, such as DSPs which can be associated with massive quasi-particles of variable masses. Moreover, due to the strong photon-photon interaction it is feasible to reach the Tonks-Giradeau regime where a strong confinement of bosonic DSPs leads to "fermionization" and "crystallization" of light [145]. These kinds of applications may give new insights into the physics of strongly correlated systems and may be an exciting prospect for quantum simulation of matter Hamiltonians in 1D using quantum optical systems [148].

List of Figures

List of Tables

Bibliography

[1] H. Walther, *Single-atom experiments and the test of fundamental quantum physics* Proc. SPIE, Vol. 1726, 2 (1992).

[2] M. A. Nielsen, I. L. Chuang, *Quantum Computation and Quantum Information.* (Cambridge University Press, 2000).

[3] D. P. DiVincenzo, *The physical implementation of quantum computation*, Fortschr. Phys. **48**, 771 (2000).

[4] D. Schrader, I. Dotsenko, M. Khudaverdyan, Y. Miroshnychenko, A. Rauschenbeutel, and D. Meschede, *Neutral Atom Quantum Register*, Phys. Rev. Lett. **93**, 150501 (2004).

[5] H. J. Metcalf and P. van der Straten, *Laser cooling and trapping*, (Springer-Verlag, New York, 1999).

[6] R. Grimm, M. Weidemüller, and Y. Ovchinnikov, *Optical dipole traps for neutral atoms*, Adv. At. Mol. Phys. **42**, 95-170 (2000)

[7] R. J. Schoelkopf and S. M. Girvin, *Wiring up quantum systems*, Nature **451**, 664 (2008).

[8] A. André, *et al.*, *A coherent all-electrical interface between polar molecules and mesoscopic superconducting resonators*, Nature Physics **2**, 636 (2006).

[9] C. Monroe and M. D. Lukin, *Remapping the quantum frontier*, Phys. World **21**, 32 (2008).

[10] D. E. Chang *et al.*, *Trapping and Manipulation of Isolated Atoms Using Nanoscale Plasmonic Structures*, Phys. Rev. Lett. **103**, 123004 (2009).

[11] T. A. Birks and Y. W. Li, *The shape of fiber tapers*, J. Lightw. Tech. **10**, 432-438 (1992).

[12] J. D. Love and W. M. Henry, *Quantifying loss minimisation in single-mode fibre tapers*, Electron. Lett. **22**, 921 (1986).

[13] M. Sumetsky, *Optics of tunneling from adiabatic nanotapers*, Opt. Lett. 31, 3420-3422 (2006).

[14] M. Sumetsky, *Theory of Adiabatic Optical Fiber and Microfiber Tapers*, in Optical Fiber Communication Conference and Exposition and The National Fiber Optic Engineers Conference, (2006).

[15] G. Sagué, E. Vetsch, W. Alt, D. Meschede and A. Rauschenbeutel, *Cold Atom Physics Using Ultra-Thin Optical Fibers: Light-Induced Dipole Forces and Surface Interactions*, Phys. Rev. Lett. **99**, 163602 (2007).

[16] K. P. Nayak *et al.*, *Optical nanofiber as an efficient tool for manipulating and probing atomic fluorescence*, Optics Express **15**, 9 5431 (2007).

[17] M. J. Morrissey , K. Deasy, Y. Wu, S. Chakrabarti, and S. Nic Chormaic, *Tapered optical fibers as tools for probing magneto-optical trap characteristics*, Rev. Sci. Instrum. **80**, 053102 (2009).

[18] C. H. Bennett and G. Brassard, *Quantum Cryptography: Public key distribution and coin tossing*, Proceedings of the IEEE International Conference on Computers, Systems, and Signal Processing, Bangalore, p. 175 (1984).

[19] A. K. Ekert, *Quantum cryptography based on Bell's theorem*, Phys. Rev. Lett. **67**, 661-663 (1991).

[20] H.-J. Briegel, W. Dür, J. I. Cirac, and P. Zoller, *Quantum Repeaters: The Role of Imperfect Local Operations in Quantum Communication*, Phys. Rev. Lett. **81**, 5932 (1998).

[21] A. Muller, H. Zbinden and N. Gisin, *Quantum cryptography over 23 km in installed under-lake telecom fibre*, Europhys. Lett. **33**, 335-340 (1996).

[22] C. Gobby, Z. L. Yuan, and A. J. Shields, *Quantum key distribution over 122 km of standard telecom fiber* Appl. Phys. Lett. **84**, 3762 (2004).

[23] L. M. Duan, M. D. Lukin, J. I. Cirac, and P. Zoller, *Long-distance quantum communication with atomic ensembles and linear optics*, Nature **414**, 413 (2001).

[24] D. N. Matsukevich, T. Chanelière, M. Bhattacharya, S.-Y. Lan, S. D. Jenkins, T. A. B. Kennedy, and A. Kuzmich, *Entanglement of a Photon and a Collective Atomic Excitation*, Phys. Rev. Lett. **95**, 040405 (2005).

[25] S. Choi, H. Deng, J. Laurat, and H. J. Kimble, *Mapping photonic entanglement into and out of a quantum memory*, Nature **452**, 67–71 (2008).

[26] Z.-S. Yuan, Y.-A. Chen, B. Zhao, S. Chen, J. Schmiedmayer, and J.-W. Pan, *Entanglement demonstration of a BDCZ quantum repeater node*, Nature **454**, 1098 (2008).

[27] B. Zhao, Y.-A. Chen, X.-H. Bao, T. Strassel, C.-S. Chuu, J. Schmiedmayer, Z.-S. Yuan, S. Chen, and J.-W. Pan. *A Millisecond Quantum Memory for Scalable Quantum Networks*, Nature Physics **5**, 95 (2008).

[28] C. A. Christensen, S. Will, M. Saba, G.-B. Jo, Y.Shin, W. Ketterle, and D. E. Pritchard, *Trapping of Ultracold Atoms in a Hollow-core Photonic Crystal Fiber.*, Phys. Rev. A **78**, 033429 (2008).

[29] M. Bajcsy, S. Hofferberth, V. Balic, T. Peyronel, M. Hafezi, A. S. Zibrov, V. Vuletic, and M. D. Lukin,*Efficient All-Optical Switching Using Slow Light within a Hollow Fiber*, Phys. Rev. Lett. **102**, 203902 (2009).

[30] J. P. Dowling and J. Gea-Banacloche, *Evanescent Light-Wave Atom Mirrors, Resonators, Waveguides, and Traps*, Adv. At. Mol. Opt. Phys. **37**, 1 (1996).

[31] Fam Le Kien, V. I. Balykin, and K. Hakuta, *Atom trap and waveguide using a two-color evanescent light field around a subwavelength-diameter optical fiber* Phys. Rev. A **70**, 063403 (2004).

[32] F. Le Kien, J. Q. Liang, K. Hakuta, and V. I. Balykin, *Field intensity distributions and polarization orientations in a vacuum-clad subwavelength-diameter optical fiber*, Opt. Commun. **242**, 445 (2004).

[33] A. W. Snyder, J. D. Love, *Optical Waveguide Theory*, (Kluwer Academic Publishers, London, 2000).

[34] A. Yariv, *Optical Electronics*, (Sanders College Publishing, Philadelphia, 1991).

[35] M. Mehrvar, C. Bis, J. Scharer, M. Moo-Young, and J. Luong, *Fiber-Optic Biosensors - Trends and Advances*, Analytical Sciences, 16 (7), 677-692, (2000).

[36] F. Warken, E. Vetsch, D. Meschede, M. Sokolowski, and A. Rauschenbeutel, *Ultra-sensitive surface absorption spectroscopy using sub-wavelength diameter optical fibers*, Optics Express **15**, 19 11952-11958 (2007).

[37] F. Warken, *Ultradünne Glasfasern als Werkzeug zur Kopplung von Licht und Materie*, Ph.D. thesis, Rheinische Friedrich-Wilhelms Universität, Bonn (2007).

[38] F. Warken, A. Rauschenbeutel, and T. Bartholomäus, *Fiber pulling profits from precise positioning*, Phot. Spectra **42**, No.3, 73 (2008).

[39] G. Sagué, *Cold atom physics using ultra-thin optical fibres*, Ph.D. thesis, Rheinische Friedrich-Wilhelms Universität, Bonn (2008).

[40] G. Sagué, A. Baade and A. Rauschenbeutel, *Blue-detuned evanescent field surface traps for neutral atoms based on mode interference in ultra-thin optical fibres*, New J. Phys. **10** 113008 (2008).

[41] A. Baade, *Light induced trapping potential for neutral atoms by mode interference of a blue detuned light field in ultra thin fibres*, Diplomarbeit, Johannes-Gutenberg Universität, Mainz (2009).

[42] A. Jöckel, *Glasfaser-basierte Fabry-Pérot-Resonatoren mit integrierten ultradünnen Passagen*, Diplomarbeit, Johannes-Gutenberg Universität, Mainz (2009).

[43] M.K. Tey, Z. Shen, S.A. Aljunid, B. Chng, F. Huber, G. Maslennikov and C. Kurtsiefer, *Strong interaction between light and a single trapped atom without the need for a cavity*, Nature Physics **4**, 924-927 (2008).

[44] J. Bures and R. Ghosh, *Power density of the evanescent field in the vicinity of a tapered fiber*, J. Opt. Soc. Am. A **16**, 8 (1999).

[45] Fam Le Kien, V. I. Balykin, and K. Hakuta, *Angular momentum of light in an optical nanofiber*, Phys. Rev. A **73**, 053823 (2006).

[46] F. Orucevic, V. Lefevre-Seguin, J. Hare, *Transmittance and Near-Field Characterization of Sub-Wavelength Tapered Optical Fibers*, Optics Express **15**, 21 13625 (2007).

[47] J. D. Jackson, *Classical electrodynamics*, (Wiley, New York, 1962).

[48] A. Ashkin, *Trapping of Atoms by Resonance Radiation Pressure*, Phys. Rev. Lett. **40**, 729 (1978).

[49] D. A. Steck, *Cesium D Line Data* (23 January 1998, Revision 1.5, 21 November 2002), http://steck.us/alkalidata/.

[50] M. Fabry, *Theoretical and experimental determinations of cesium oscillator strengths*, J. Quant. Spectrosc. Radiat. Transf., **16**, 2, (1976).

[51] D. Schrader, *A neutral atom quantum register*, Ph.D. thesis, Rheinische Friedrich-Wilhelms Universität, Bonn (2004).

[52] A. Messiah, *Quantum Mechanics*, (Volume II), 12th edition, (North Holland Publishing, New York, 1981).

[53] M. Boustimi, J. Baudon, P. Candori, and J. Robert, *van der Waals interaction between an atom and a metallic nanowire*, Phys. Rev. B **65**, 155402 (2002).

[54] A. Laliotis *et al.*, *Testing the distance-dependence of the van der Waals interaction between an atom and a surface through spectroscopy in a vapor nanocell*, Proc. of SPIE **6604**, 660406-1 (2007).

[55] A. Derevianko, W. R. Johnson, M. S. Safronova and J. F. Babb, *High-Precision Calculations of Dispersion Coefficients, Static Dipole Polarizabilities, and Atom-Wall Interaction Constants for Alkali-Metal Atoms*, Phys. Rev. Lett. **82** 18 3589 - 3592 (1999).

[56] M. Fichet *et al.*, *Exploring the van der Waals atom-surface attraction in the nanometric range*, Europhys. Lett. **77**, 54001 (2007).

[57] D. Bloch, M. Ducloy, *Atom-Wall interaction*, Adv. At. Mol. Opt. Phys. **50**, (B. Bederson and H. Walther eds., Elsevier-Academic Press, 2005).

[58] T. Kuga, Y. Torii, N. Shiokawa, T. Hirano, Y. Shimizu, and H. Sasada *Novel Optical Trap of Atoms with a Doughnut Beam* Phys. Rev. Lett. **78**, 4713 (1997).

[59] R. G. Beausoleil, and T. W. Hänsch, *Ultra-high resolution two-photon optical Ramsey spectroscopy of an atomic fountain*, Phys. Rev. A **33**, 1661-1670 (1986).

[60] J. McKeever, J. R. Buck, A. D. Boozer, A. Kuzmich, H. C. Nagerl, D. M. Stamper-Kurn, and H. J. Kimble, *State-insensitive cooling an trapping of single atoms in an optical cavity*, Phys. Rev. Lett. **90** 133602 (2003).

[61] M. Takamoto, F.-L. Hong, R. Higashi and H. Katori, *An optical lattice clock*, Nature **435**, 321-324, (2005).

[62] N.L. Manakov, V.D. Ovsiannikov, L.P. Rapoport, *Atoms in a laser field*, Phys. Rep. **141**, 6, 320-433, (1986).

[63] J. Dalibard and C. Cohen-Tannoudji, *Dressed-atom approach to atomic motion in laser light: the dipole force revisited*, J. Opt. Soc. Am. B **2**, 1707-1720 (1985).

[64] N. B. Delone, and V. P. Krajnov, *AC Stark shift of atomic energy levels*, Physics-Uspekhi **42**, (7) 669-687 (1999).

[65] Fam Le Kien, V. I. Balykin, K. Hakuta, *State-Insensitive Trapping and Guiding of Cesium Atoms Using a Two-Color Evanescent Field around a Subwavelength-Diameter Fiber*, J. Phys. Soc. Jpn. **74**, 3 910-917(2005).

[66] R. W. Schmieder, *Matrix Elements of the Quadratic Stark Effect on Atoms with Hyperfine Structure*, Amer. J. Phys. **40**, 297 (1972).

[67] P. Rosenbusch, S. Ghezali, V. A. Dzuba, V. V. Flambaum, K. Beloy, and A. Derevianko, *ac Stark shift of the Cs microwave atomic clock transitions* Phys. Rev. A **79**, 013404 (2009).

[68] D. Budker, D. F. Kimball, and D. P. DeMille, *Atomic Physics: Exploration Through Problems and Solutions*, Chapter 4.5, Oxford University Press, (2008).

[69] *High-Precision Measurements in Atomic Cesium Supporting a Low-Energy Test of the Standard Model*, S. C. Bennett, Ph.D. thesis, University of Colorado (1998).

[70] G. A. Askar'yan,*Effects of the Gradient of a Strong Electromagnetic Beam on Electrons and Atoms* Zh. Eksp. Teor. Fiz. 42, p. 1567, engl. translation Sov. Phys. JETP **15**, 1088 (1962).

[71] V. S. Letokhov, *Doppler line narrowing in a standing light wave*, Pis. Zh. Eksp. Teor. Fiz. **7**, 348 (1968), engl. translation JTEP Lett. **7**, 272 (1968).

[72] T. W. Hänsch and A. L. Schawlow, *Cooling of gases by laser radiation*, Opt. Commun. **13**, 68 (1975)

[73] D. Wineland and H. Dehmelt, *Proposed $\Delta\nu/\nu < 10^{-14}$ Laser Fluorescence Spectroscopy on Tl+ Mono-Ion Oscillator III (side band cooling)*, Bull. Am. Phys. Soc. **20**, 637 (1975).

[74] A. L. Migdall, J. V. Prodan, and W. D. Phillips, T. H. Bergeman and H. J. Metcalf, *First Observation of Magnetically Trapped Neutral Atoms*, Phys. Rev. Lett. **54**, 2596-2599 (1985).

[75] S. Chu, L. Hollberg, J. E. Bjorkholm, A. Cable, and A. Ashkin, *Three-dimensional Viscous Confinement and Cooling of Atoms by Resonance Radiation Pressure*, Phys. Rev. Lett. **55**, 48 (1985).

[76] S. Chu, J. E. Bjorkholm, A. Ashkin, and A. Cable *Experimental Observation of Optically Trapped Atoms* Phys. Rev. Lett. **57**, 314 (1986).

[77] E. L. Raab, M. Prentiss, A. Cable, S. Chu, and D. E. Pritchard, *Trapping of Neutral Sodium Atoms with Radiation Pressure*, Phys. Rev. Lett. **59**, 2631 (1987).

[78] V. I. Balykin, V. S. Letokhov, Yu. B. Ovchinnikov, and A. I. Sidorov, *Quantum-State-Selective Mirror Reflection of Atoms by Laser Light*, Phys. Rev. Lett. **60**, 2137-2140 (1988).

[79] Yu. B. Ovchinnikov, I. Manek, and R. Grimm, *Surface Trap for Cs atoms based on Evanescent-Wave Cooling*, Phys. Rev. Lett. **79**, 2225-2228 (1997).

[80] M. Hammes, D. Rychtarik, V. Druzhinina, U. Moslener, I. Manek-Hnninger, R. Grimm, *Optical and evaporative cooling of caesium atoms in the gravito-optical surface trap*, J. of Mod. Optics **47**, 14 2755-2767 (2000).

[81] N. Westbrook, C. I. Westbrook, A. Landragin, G. Labeyrie, L. Cognet, V. Savalli, G. Horvath, A. Aspect, C. Hendel, K. Moelmer, J.-Y. Courtois, W. D. Phillips, R. Kaiser, and V. Bagnato, *New Physics with Evanescent Wave Atomic Mirrors: The van der Waals Force and Atomic Diffraction*, Physica Scripta. **78**, 712 (1998).

[82] A. H. Barnett, S. P. Smith, M. Olshanii, K. S. Johnson, A. W. Adams, and M. Prentiss, *Substrate-based atom waveguide using guided two-color evanescent light fields*, Phys. Rev. A **61**, 023608 (2000).

[83] J. P. Burke Jr., Sai-Tak Chu, G. W. Bryant, C. J. Williams, and P. S. Julienne, *Designing neutral-atom nanotraps with integrated optical waveguides*, Phys. Rev. A **65**, 043411 (2002).

[84] H. Gauck, M. Hartl, D. Schneble, H. Schnitzler, T. Pfau, and J. Mlynek *Quasi-2D Gas of Laser Cooled Atoms in a Planar Matter Waveguide* Phys. Rev. Lett. **81**, 5298 (1998).

[85] V. I. Balykin, K. Hakuta, Fam Le Kien, J. Q. Liang, and M. Morinaga, *Atom trapping and guiding with a subwavelength-diameter optical fiber*, Phys. Rev. A **70**, 011401(R) (2004).

[86] J. Dalibard and C. Cohen-Tannoudji, *Laser cooling below the Doppler limit by polarization gradients: simple theoretical models*, JOSA B **6**, 11 2023-2045 (1998).

[87] K. B. Davis, M.-O. Mewes, W. Ketterle *An analytical model for evaporative cooling of atoms* Appl. Phys. B 60, 155-159 (1995).

[88] C. G. Townsend, N. H. Edwards, C. J. Cooper, K. P. Zetie, and C. J. Foot, A. M. Steane, P. Szriftgiser, H. Perrin, and J. Dalibard, *Phase-space density in the magneto-optical trap*, Phys. Rev. A **52**, 1423 (1995).

[89] M.-O. Mewes, M. R. Andrews, N. J. van Druten, D. S. Durfee, D. M. Kurn, and W. Ketterle, *Bose-Einstein Condensation in a Gas of Sodium Atoms*, Phys. Rev. Lett. **75**, 22 (1995).

[90] K. G. Libbrecht, R. A. Boyd, P. A. Willems, T. L. Gustavson, and D. K. Kim, *Construction of Stabilized Lasers and Lithium Cells*, Am. J. Phys. **63**, 729 (1995).

[91] K. C. Harvey and C. J. Myatt, *External-cavity diode laser using a grazing-incidence diffraction grating*, Opt. Lett. **16**, 910 (1991).

[92] W. Demtröder, *Laserspektroskopie*, (Springer-Verlag, Berlin, 1993).

[93] E. R. I. Abraham and E. A. Cornell, *Teflon feedthrough for coupling optical fibers into ultrahigh vacuum systems*, Applied Optics **37** 10 (1998).

[94] Gamma Vacuum, *Ion Pumping of Cesium and Rubidium*, Technical Bulletin (2006).

[95] S. J. M. Kuppens, K. L. Corwin, K. W. Miller, T. E. Chupp, and C. E. Wieman, *Loading an optical dipole trap* Phys. Rev. A **62**, 013406 (2000).

[96] C. Salomon, J. Dalibard, W. D. Phillips, A. Clairon and S. Guellat, *Laser Cooling of Cesium Atoms below 3 μK*, Europhys. Lett., **12** 8, 683-688 (1990).

[97] N. Schlosser, G. Reymond, and P. Grangier, *Collisional Blockade in Microscopic Optical Dipole Traps*, Phys. Rev. Lett. **89**, 023005 (2002).

[98] J. E. Bjorkholm, *Collision-limited lifetimes of atom traps* Phys. Rev. A **38**, 1599 (1988).

[99] U. Schlöder, H. Engler, U. Schünemann, R. Grimm, and M. Weidemüller, *Cold inelastic collisions between lithium and cesium in a two-species magneto-optical trap.* Eur. Phys. J. D., **7**, 331-340, (1999).

[100] W. Alt, *Optical control of single neutral atoms*, Ph.D. thesis, Rheinische Friedrich-Wilhelms Universität, Bonn (2004).

[101] W. Alt, *An objective lens for efficient fluoresence detection of single atoms* Optik **113**, (3) 142 (2002).

[102] T. M. Brzozowski, M. Maczazyńska, M. Zawada, J. Zachorowski and W. Gawlik, *Time-of-flight measurement of the temperature of cold atoms for short trap-probe distances*, J. Opt. B: Quantum Semiclass. Opt. **4**, 62-66 (2002).

[103] L. D. Landau and E. M. Lifschitz, *Mechanics*, Pergamon, New York (1976)

[104] W. H. Press, S. A. Teukolsky, W. T. Vetterling and B. P. Flannery *Numerical Recipes in C: The Art of Scientific Computing*, Cambridge University Press, New York 2nd edition (1992).

[105] C. Henkel, S. Pötting, and M. Wilkens, *Loss and heating of particles in small and noisy traps* Appl. Phys. B **69**, 379-387 (1999)

[106] C. Henkel, and M. Wilkens, *Heating of trapped atoms near thermal surfaces* Europhys. Lett. **47**, 414-420, (1999)

[107] V. Bagnato, D. E. Pritchard, and D. Kleppner, *Bose-Einstein condensation in an external potential*, Phys. Rev. A **35**, 4354 (1987)

[108] M. E. Gehm, K. M. O'Hara, T. A. Savard, and J. E. Thomas *Dynamics of noise-induced heating in atom traps* Phys. Rev. A **58**, 3914 (1998).

[109] T. A. Savard, K. M. O'Hara, and J. E. Thomas *Laser-noise-induced heating in far-off resonance optical traps* Phys. Rev. A **56**, R1095 (1997).

[110] D.J. Wineland and W.M. Wayne Itano, *Laser Cooling of Atoms*, Phys. Rev. A **20**, 1521-1540 (1979).

[111] A. L. Gaeta and R. W. Boyd, *Stochastic dynamics of stimulated Brillouin scattering in an optical fiber* Phys. Rev. A **44**, 3205 (1991).

[112] P. C. Wait and T. P. Newson, *Measurement of Brillouin scattering coherence length as a function of pump power to determine Brillouin linewidth*, Opt. Comm. ,**117**, 1-2, pp 142-146, (1995).

[113] R.W. Boyd, *Nonlinear Optics*, Academic Press, New York (1992) Chapter 8.

[114] D. Schrader, S. Kuhr, W. Alt, M. Müller, V. Gomer, and D. Meschede, *An optical conveyor belt for single neutral atoms*, Appl. Phys. B **73**, 819 (2001).

[115] S. Kuhr, W. Alt, D. Schrader, M. Müller, V. Gomer, and D. Meschede, *Deterministic Delivery of a Single Atom*, Science **293**, 278 (2001).

[116] H. Zoubi and H. Ritsch, *Superradiant and dark exciton states in an optical lattice within a cavity* Europhys. Lett. **87**, 23001 (2009), and H. Ritsch (private communication).

[117] H. Zoubi, H. Ritsch, *Hybrid Quantum System of a Nanofiber Mode Coupled to Two Chains of Optically Trapped Atoms*, arXiv:1006.1971 (June 2010)

[118] M. Khudaverdyan, W. Alt, I. Dotsenko, T. Kampschulte, K. Lenhard, A. Rauschenbeutel, S. Reick, K. Schörner, A. Widera, and D. Meschede, *Controlled insertion and retrieval of atoms coupled to a high-finesse optical resonator*, New J. Phys. **10**, 7 073023 (2008).

[119] T. Aoki, B. Dayan, E. Wilcut, W. P. Bowen, A. S. Parkins, T. J. Kippenberg, K. J. Vahala and H. J. Kimble, *Observation of strong coupling between one atom and a monolithic microresonator*, Nature **443**, 671–674 (2006).

[120] M. Pöllinger, D. O'Shea, F. Warken, and A. Rauschenbeutel Ultra-high-Q tunable whispering-gallery-mode microresonator Phys. Rev. Lett. **103**, 053901 (2009)

[121] R. J. Mailloux, *Phased array antenna handbook*, Boston, MA: Artech House, (1994).

[122] R. Loudon, *The Quantum Theory of Light*, Oxford University Press, 3rd ed. (2000).

[123] Bo Gao, *Effects of Zeeman degeneracy on the steady-state properties of an atom interacting with a near-resonant laser field: Resonance flourescence*, Phys. Rev. A 50, 4139-4156 (1994).

[124] E. S. Polzik and J. Fiuráŝek, *Quantum Interface Between Light and Atomic Ensembles, in Lectures on Quantum Information*, (eds D. Bruß and G. Leuchs), Wiley-VCH, Weinheim (2008).

[125] N. Lindlein, R. Maiwald, H. Konermann, M. Sondermann, U. Peschel, and G. Leuchs, *A new 4π-geometry optimized for focusing onto an atom with a dipole-like radiation pattern*, Laser Physics **17**, 927-934 (2007).

[126] F. L. Kien, V. I. Balykin, and K. Hakuta, *Scattering of an evanescent light field by a single cesium atom near a nanofiber*, Phys. Rev. A **73**, 013819 (2006).

[127] S. Wolf, S. J. Oliver, and D. S. Weiss, *Suppression of Recoil Heating by an Optical Lattice*, Phys. Rev. Lett. **85**, 4249 (2000).

[128] V. Gomer, and D. Meschede, A single trapped atom: Light-matter interaction at the microscopic level, Ann. Phys. (Leipzig) **10** (1-2), 9-18 (2001)

[129] Fam Le Kien and K. Hakuta, *Cooperative enhancement of channeling of emission from atoms into a nanofiber*, Phys. Rev. A 77, 013801 (2008).

[130] Fam Le Kien, S. Dutta Gupta, V. I. Balykin, and K. Hakuta, *Spontaneous emission of a cesium atom near a nanofiber: Efficient coupling of light to guided modes*, Phys. Rev. A **72**, 032509 (2005).

[131] V. B. Braginsky and F. Ya. Khalili, *Quantum Measurement*, Rev. Mod. Phys. **68**, 1-11, (1996).

[132] D. Oblak *et al.*, *Quantum-noise-limited interferometric measurement of atomic noise: Towards spin squeezing on the Cs clock transition*, Phys. Rev. A, **71**, 043807 (2005).

[133] Greg A. Smith, S. Chaudhury, A. Silberfarb, I. H. Deutsch, and P. S. Jessen, *Continuous Weak Measurement and Nonlinear Dynamics in a Cold Spin Ensemble*, Phys. Rev. Lett. **93**, 163602 (2004).

[134] E. Hecht, *Optics*, 2nd ed., Addison-Wesley (1987).

[135] B. E. A. Saleh, and M. C. Teich, *Fundamentals of Photonics*, Wiley Series in Pure and Applied Optics, 2nd. edition, (2007).

[136] L. Allen and J. H. Eberly, *Optical Resonance and Two-Level Atoms* (Wiley, New York, 1975).

[137] I. I. Sobelman, *Atomic Spectra and Radiative Transitions*, (Springer, Berlin, 1992), 2nd edition.

[138] W. Ketterle, D. S. Durfee, and D. M. Stamper-Kurn: *Making, probing and understanding Bose-Einstein condensates.*, Bose-Einstein condensation in atomic gases, Proceedings of the International School of Physics "Enrico Fermi", Course CXL, edited by M. Inguscio, S. Stringari and C.E. Wieman (IOS Press, Amsterdam, 1999) pp. 67-176.

[139] C. M. Savage, S. L. Braunstein, and D. F. Walls, *Macroscopic quantum superpositions by means of single-atom dispersion* Opt. Lett. **15**, 628 (1990).

[140] M. Fleischhauer, A. Imamoglu, and J. P. Marangos, *Electromagnetically induced transparency: Optics in Coherent Media*, Rev. Mod. Phys. **77**, 633 (2005)

[141] M. D. Lukin, and A. Imamoglu, *Controlling photons using electromagnetically induced transparency*, Nature **413**, 273-276 (2001).

[142] T. Chanelière, D. N. Matsukevich, S. D. Jenkins, S.-Y. Lan, T. A. B. Kennedy and A. Kuzmich, *Storage and retrieval of single photons transmitted between remote quantum memories* Nature **438**, 833-836 (2005).

[143] A. André, M. Bajcsy, A. S. Zibrov, and M. D. Lukin, *Nonlinear Optics with Stationary Pulses of Light*, Phys. Rev. Lett. **94**, 063902 (2005).

[144] M. Fleischhauer, J. Otterbach, and R. G. Unanyan, *Bose-Einstein Condensation of Stationary-Light Polaritons*, Phys. Rev. Lett. **101**, 163601 (2008).

[145] D. E. Chang, V. Gritsev, G. Morigi, V. Vuletic', M. D. Lukin, and E. A. Demler *Crystallization of strongly interacting photons in a nonlinear optical fibre*, Nature Physics **4**, 884 - 889 (2008)

[146] A. K. Patnaik, J. Q. Liang, and K. Hakuta, *Slow light propagation in a thin optical fiber via electromagnetically induced transparency*, Phys. Rev. A **66**, 063808 (2002).

[147] C. Ottaviani, S. Rebić, D. Vitali, P. Tombesi, *Quantum phase-gate operation based on nonlinear optics: Full quantum analysis*, Phys. Rev. A **73**, 010301(R) (2006).

[148] R. G. Unanyan, J. Otterbach, and M. Fleischhauer,/ J. Ruseckas, V. Kudriasov, and G. Juzeliunas, *Spinor Slow-Light and Dirac Particles with Variable Mass*, Phys. Rev. Lett. 105, 173603 (2010).

[149] S. T. Dawkins, E. Vetsch, D. Reitz, R. Mitsch, and A. Rauschenbeutel, *Non-destructive Phase Detection with fiber coupled atoms*, In preparation (2010).

Danksagung

An dieser Stelle möchte ich Allen danken die am gelingen dieser Arbeit beteiligt waren.

Mein erster Dank gilt meinem Betreuer, der es mir ermöglicht hat, an diesem interessanten Projekt mitwirken zu dürfen, und für die Unterstützung, die vielen Ratschläge und wertvollen Diskussionen die meinen Einblick in die Quantenoptik vertieft haben.

Allen Mitglieder der Arbeitsgruppe möchte für die super nette Atmosphäre und die große Hilfsbereitschaft danken. Ganz besonderer Dank gebührt den Kollegen die an meiner Seite so manch lange Messnacht verbracht haben: Darunter Guillem, mit dessen Hilfe das Experiment verwirklicht werden konnte, der mir auch abseits der Physik ein geschätzter Freund geworden ist. Regine und Daniel die darauf unser Team verstärkt haben und durch ihren wertvollen Einsatz wesentlich zum Erfolg des Projekts beigetragen haben. Unseren PostDoc Sam, der mit seinem breiten Wissen uns viele neue Anregungen bereitet, und den experimentellen Ablauf immens vereinfacht hat. Dem neuen Doktoranden Rudolf danke ich für das Auffinden und Überprüfen von meinen fehlerhaften Berechnungen mit Mathematica. Auch danke ich allen die die an der Korrektur meiner Arbeit mitgewirkt haben. Danken möchte ich auch meinen ehemaligen Kollegen, insbesondere Dietmar, Wolfgang und Florian für die Unterweisung in die experimentelle Arbeit sowie für die Realisierung der Faserziehanlage ohne die diese Arbeit nicht verwirklicht hätte werden können.

Insbesondere gilt mein Dank der Administrative des Instituts; dem Sekretariat mit Christine und Elvira, der Etatverwaltung, Warenannahme, usw., dafür dass sie mit der reibungslose Abwicklung aller Verwaltungaufgaben uns permanent den Rücken frei halten. Für die technische Unterstützung danke ich Herrn Lenk sowie Michael für die viele Hilfe in Elektronik Angelegenheiten, sowie den mechanischen Werkstätten des Instituts, die durch ihre kompetente und hochqualifizierte Arbeit zum Erfolg der Arbeit entscheidend beigetragen haben.

Ganz besonders danken möchte ich all denen Menschen die mich auch in anderen Belangen meines Lebens unterstützen. Meiner Familie die immer für mich da war und immer an mich geglaubt haben. Meiner Freundin Regine danke ich für die Unterstützung und Rückhalt die sie mir auch in schwierigen Zeiten gegeben hat. Danke für die Geduld mit mir!

Allen Kollegen und Freunden die hier aus Platzgründen unerwähnt bleiben wünsche ich alles Gute.